



**CENTRO DE INVESTIGACIÓN Y DE ESTUDIOS
AVANZADOS DEL INSTITUTO POLITÉCNICO
NACIONAL**

UNIDAD ZACATENCO

PROGRAMA DE DOCTORADO
NANOCIENCIAS Y NANOTECNOLOGÍA

**CATALYST SUPPORTED ON CARBON NANOSTRUCTURES FOR
AMMONIA ELECTROLYSIS**

T E S I S

Que presenta

MARLEN ALEXIS GONZÁLEZ REYNA

Para obtener el grado de
Doctora en Ciencias

Director de la Tesis:
Juan Francisco Pérez Robles

Ciudad de México

Diciembre 2019

ACKNOWLEDGEMENTS

Undertaking this PhD has been a truly life-changing experience that it would not have been possible to do without the support and guidance that I received from many people.

Thanks for all your encouragement!

And finally, last but by no means least, I want to show my gratitude to **CONACYT** for my scholarship support under the grant **424698**.

TABLE OF CONTENTS

| | |
|--|----|
| INTRODUCTION..... | 1 |
| OBJECTIVES..... | 6 |
| MATERIALS AND METHODS..... | 8 |
| 1.1. MATERIALS..... | 8 |
| 1.2. SYNTHESIS..... | 9 |
| 1.2.1. CVD catalyst..... | 9 |
| 1.2.2. Carbon nanostructures..... | 10 |
| 1.2.3. Ammonia oxidation catalyst | 12 |
| 1.3. CHARACTERIZATION METHODS..... | 13 |
| 1.3.1. Thermogravimetric analysis (TGA) | 13 |
| 1.3.2. Surface area and porosity | 14 |
| 1.3.3. Scanning Electron Microscopy (SEM)..... | 16 |
| 1.3.4. X-ray powder diffraction (XRD)..... | 17 |

| | |
|--|-----------|
| 1.3.5. Spectroscopic methods..... | 17 |
| 1.3.6. Electrochemistry | 19 |
| 1.3.7. Chemical analysis | 22 |
| RESULTS AND DISCUSSION..... | 23 |
| 2.1. CVD CATALYST | 23 |
| 2.2. CARBON NANOSTRUCTURES..... | 29 |
| 2.3. CNT AND CNS AS CATALYST SUPPORT | 31 |
| 2.4. NICKEL AS AOR ELECTROCATALIST..... | 35 |
| 2.5. AMMONIA OXIDATION PROCESS..... | 37 |
| CONCLUSIONS..... | 54 |
| REFERENCES | 57 |
| APPENDIX..... | i |
| ANNEX..... | v |

Abstract

The electrolysis of ammonia has the selection of the electrodes as a factor to minimize losses and optimize energy consumption. With this thesis, it is proposed the use of nickel supported on carbon nanotubes and carbon nanospheres as a cheaper catalyst alternative to the commonly platinum electrodes for the oxidation process of ammonia. Using scanning electron microscopy and Raman spectroscopy is confirmed the presence of the Ni on the surface of the carbon nanostructures and based on the electrochemical results is established that the redox process between Ni^{+2} and Ni^{+3} plays the role of intermediate in the ammonia oxidation reaction. This process causes an increment in the anodic current density that is dependent on the pH and ammonia concentration. Even more, using the rotating disk electrode technique, the ammonia oxidation, is defined as a diffusion-controlled process that follows first-order kinetics respect to the concentration of ammonia and suggests the formation of nitrogen as the principal reaction product, where the carbon nanospheres present the best results.

Evenmore, is offered an advantageous synthesis of carbon nanotubes and carbon nanospheres with nickel encapsulated inside by using a one-step CVD process which saves time and money. The presence of nickel nanoparticles was confirmed by STEM micrographs and TGA analysis, and the catalytic activity evaluated by means of electrochemical characterization.

Resumen

La electrólisis del amoníaco tiene la selección de los electrodos como un factor para minimizar las pérdidas y optimizar el consumo de energía. Con esta tesis, se propone el uso de níquel soportado en nanotubos de carbono y nanoesferas de carbono como una alternativa de catalizador más barata a los electrodos de platino, comúnmente utilizados para el proceso de oxidación del amoníaco. Mediante microscopía electrónica de barrido y espectroscopía Raman se confirma la presencia de Ni en la superficie de las nanoestructuras de carbono y, según los resultados electroquímicos, se establece que el proceso redox entre Ni^{+2} y Ni^{+3} desempeña el papel de intermediario en la reacción de oxidación de amoníaco. Este proceso provoca un incremento en la densidad de corriente anódica que depende del pH y la concentración de amoníaco. Aún más, usando la técnica de electrodo de disco giratorio, la oxidación de amoníaco, se define como un proceso controlado por difusión que sigue una cinética de primer orden con respecto a la concentración de amoníaco y sugiere la formación de nitrógeno como el principal producto de reacción, donde las nanoesferas de carbono presentan los mejores resultados.

Además, se ofrece una síntesis ventajosa de nanotubos de carbono y nanoesferas de carbono con níquel encapsulado en su interior mediante el uso de un proceso CVD de un solo paso que ahorra tiempo y dinero. La presencia de nanopartículas de níquel fue confirmada por micrografías STEM y análisis TGA, y la actividad catalítica evaluada mediante caracterización electroquímica.

INTRODUCTION

The increasing energy demand leads to develop alternatives that offer high-efficiency technology, eco-sustainable energy conversion, and good energy storage by means of solar cells, wind turbines, batteries, super-capacitors, electrolyzers, fuel cells, etc.

Electrolysis is a promising option to obtain hydrogen, and fuel cells provide an opportunity to develop thermodynamic systems that generate electricity based on that hydrogen. This technology presents high efficiency, low environmental footprint

and the direct conversion of fuel to electricity. In this context, advanced water electrolysis has been considered as one of the most efficient and reliable approaches to obtain hydrogen. Nevertheless, ammonia has been considered as a possible fuel for use in fuel cell applications recently; it has the advantage of being a relatively cheap liquid fuel, and it appears to oxidize completely to nitrogen and water. Compared with water electrolysis that requires at least 33 Wh g⁻¹ H₂ at standard conditions ammonia electrolysis requires 1.55 Wh g⁻¹ H₂ which represents 95% less energy [1,2]. It indicates that the potential of the ammonia electrolysis technology to produce hydrogen is an energy-efficient process theoretically.

Even more, ammonia is a pollutant frequently found in wastewater resulting from domestic, industrial and agricultural activities causing water eutrophication¹; consequently, its removal is an important task. This process is commonly carried out by bacterial degradation, but present high cost[3]. On the other hand, due to ammonia has a high hydrogen capacity, as was said early, the electrochemical process is one promising method that has attracted great attention, because offers environmental remediation while produces hydrogen [1,2,4,5]. Moreover, ammonia offers significant advantages due to its higher density, easier storage and distribution does not release carbon oxides during its decomposition.

¹ Eutrophication: In agreement with the Meriam Webster dictionary is the process by which a body of water becomes enriched in dissolved nutrients (such as phosphates) that stimulate the growth of aquatic plant life usually resulting in the depletion of dissolved oxygen.

In the case of anodic reactions like the oxygen evolution reaction (OER) and ammonia oxidation reaction (AOR), metallic oxides can act as reaction precursors or even directly participate in interfacial electrochemical processes. These oxides can offer an alternative reaction pathway that possesses a reduced activation Gibbs energy, thus act as electrocatalysts [6]. Usually, for those reactions, Pt, Ru, Pd, and Ir are used as catalytic electrode, nevertheless, the lack of affordability limits their application on an industrial scale [7–10]. So far, the use of catalyst support as carbon black is commonly contemplated, due to its low cost and high availability, but carbon corrosion is present, among other issues [5,11–13]. On the other hand, carbon nanotubes (CNTs) and carbon nanospheres (CNSs) are stable, have a high surface area, and good electrical conductivity making them a better choice as catalyst support [14–17].

Nickel was used, since the late 60s, in numerous electrochemical systems, such as rechargeable batteries, supercapacitors, fuel cells, electrolyzers, and as an effective and cheap catalyst for the oxidation of small organic compounds including a wide range of alcohols and amines, oxalic acid, ethylene glycol, glycerol, glucose, etc. [18–22]. As an example, the work reported by Fleischmann et al. [23] in 1970, was carried out to analyze the oxidation of some organic compounds, particularly amines and alcohols, at a passivated nickel anode. The oxidation of those organic compounds at a nickel anode in aqueous alkaline solution shows its capacity to efficiently catalyze the conversion of primary alcohols, secondary alcohols and primary amines to carboxylic acids, ketones and nitriles respectively. The kinetics for these anodic oxidations has been studied and a mechanism has been proposed to explain the

behavior observed. Nevertheless, its use in ammonia, even when it oxidized at same potential its limited and present contradictories conclusions.

For instance, in 1966, Despic et al.[24], studied the kinetics of the anodic oxidation of ammonia in alkaline solution at Raney nickel electrode. In their investigation, a nickel electrode failed to give meaningful results. Here, they claimed that electrochemically activated surfaces were spontaneously oxidized at the potentials obtaining in ammonia solution and hence lost practically all catalytic activity for the anodic oxidation of ammonia. Years later, Yao and Cheng [25] make their own investigation of the electrocatalytic activity of nickel using cyclic voltammetry and semiconductor electrochemistry theory. Their results, in agreement with those found by Despic, shown that nickel does not present catalytic activity and offer an explication saying that the layer of oxide formed on the nickel electrode surface disable the adsorption of ammonia and hence its activity. However, in the same article, Yao and Cheng in presence of $(\text{NH}_4)_2\text{SO}_4$ and NH_4Cl , found that nickel could catalyst the ammonia oxidation, suggesting that apparently, the presence of NH_4^+ ions, helps in the ammonia oxidation, but the sequential discharging processes inhibit the nickel activity.

On the other hand, Kapalka et al. [26] using NH_4ClO_4 , claimed that NH_3 rather than NH_4^+ is oxidized on nickel electrodes. Even more, they by means of chronoamperometry found out that Ni is not deactivated during the oxidation process even at high ammonia concentrations. Nevertheless, testing the bulk

electrolysis at pH 11, after 12 hours, they noticed that the solution became grey suggesting corrosion of the electrode. In contrast, Candido et al. [27] using $(\text{NH}_4)_2\text{SO}_4$ claimed that Ni corrosion is present only at pH 7, but not at higher pH, and demonstrated activity for ammonia and ammonium ion. Besides, Shih et al. [28,29] present a direct AOR on nickel using ammonium sulfate and sodium sulfate as supporting electrolyte, where they proposed an electrochemical mechanism of AOR process on nickel, which differs from the mechanism proposed by Kapalka [26].

In this thesis, carbon nanotubes were synthesized looking for an efficient process, which involves the analysis of the catalyst metal, temperature, time, and the flow velocity of the precursor gas inside the CVD chamber. The CNTs were characterized morphologically and structurally using scanning electron microscopy (SEM), Raman spectroscopy, Fourier transform infrared spectroscopy (FTIR) and X-ray diffraction (XRD). For the ammonia oxidation reaction, is reported several electrochemical measurements performed using CNT decorated with nickel as a catalytic electrode. Based on the pH-controlled equilibrium of the $\text{NH}_3/\text{NH}_4^+$ in aqueous solution, three pH values were considered for the tests: pH 7 were the predominant specie is NH_4^+ , pH 9.4 where both species are present in equal percentage and pH 11 were NH_3 represents more than 99% in the solution.

OBJECTIVES

- Formulate a synthesis method for carbon nanostructures that would be used as catalyst supports for the ammonia oxidation reaction, those carbon nanostructures must present high electrical conductivity, high surface area and be inert in the catalytic reaction.
- Define under what conditions nickel can catalyze the ammonium and ammonia electrochemical oxidation reaction, and when is more efficient.

- Evaluate if nickel suffer corrosion when catalyzing the ammonium or ammonia oxidation reaction.
- Asses if nickel lost activity after some time off been used as a catalyst for the ammonium or ammonia oxidation reaction or with high ammonium or ammonia concentration.

MATERIALS AND METHODS

1.1. MATERIALS

For the CVD catalyst preparation, ethanol, tetraethyl orthosilicate (TEOS), nitric acid (HNO_3), iron (III) nitrate nonahydrate ($\text{Fe}(\text{NO}_3)_3 \cdot 9\text{H}_2\text{O}$) and nickel (II) nitrate hexahydrate ($\text{Ni}(\text{NO}_3)_2 \cdot 6\text{H}_2\text{O}$) were used. For the synthesis of the MWCNTs nitrogen gas with 99.99% purity, nitrogen-hydrogen mixture gas (90:10), and acetylene gas were used, all purchased from INFRA, México.

For electrochemical tests, sulphuric acid (H_2SO_4), potassium hydroxide (KOH), ammonium sulfate ($(\text{NH}_4)_2\text{SO}_4$), potassium sulfate (K_2SO_4), and Nafion 117 solution were used. All chemicals were purchased from Sigma Aldrich and used as received unless were said the contrary. All solutions were prepared using deionized water with a resistivity around **18 M Ω cm** (obtained from a Millipore water purification system).

1.2. SYNTHESIS

1.2.1. CVD catalyst

To produce the catalyst support, the Sol-Gel² technique was employed using TEOS as a silicon source. The amounts of iron and nickel nitrates were estimated at a mole ratio of 2 (Fe: Ni), while the $\text{NiFe}_2\text{O}_4 / (\text{NiFe}_2\text{O}_4 + \text{SiO}_2)$ weight ratio was defined to 70 %.

TEOS was first dissolved in ethanol to prepare it for the hydrolysis, then, the solution was slowly added into an aqueous solution of mixed iron nitrate and nickel nitrate. The TEOS/ethanol/ H_2O molar ratio was fixed at 1:1:4 in order to obtain a castable solution. The mixture was stirring for several minutes, initially, it appeared turbid and then turned transparent with an exothermic response, indicating that the hydrolysis of TEOS had taken place. An aqueous solution of HNO_3 was added to promote the hydrolysis process with a linear polymerization.

² See supplementary information (appendix) to learn more about Sol-Gel process

The catalyst liquid solution was put in a rotative cylindrical reactor to dry and milled at 350 °C for 3 hours, followed by calcination of the catalyst powder at 650 °C for 3 hours.

1.2.2. Carbon nanostructures

Carbon nanostructures as carbon nanotubes (CNTs) and carbon nanospheres (CNSs) have been synthesized by different methods, most of them take place in a vacuum chamber or with protective gases as nitrogen or argon. Some of those methods are arc discharge, laser ablation, and chemical vapor deposition (CVD). Of those, CVD is the most promising for the industrial scaling, for its price per unit ratio, and because CVD allows carbon nanostructures synthesis directly on a substrate (Table 1).

The equipment for a standard CVD consists of a reaction chamber (normally a quartz tube) and a heating furnace (Figure 1). In this thesis, a standard CVD synthesis was performed, using FeNi/SiO₂ particles as the catalyst. The catalyst is loaded into the quartz-tube reactor, then, under vacuum, the temperature is raised until 700 °C and nitrogen gas is delivered to the reactor at 1 liter per minute (LPM) for 10 minutes to drag off all the oxygen particles and to create an inert atmosphere. Afterward, the catalyst particles were reduced using a flowing mix of gases (N₂/H₂ at 90:10 %) at 1 LPM for 20 minutes. To initiate the growth of the carbon

nanostructures, acetylene is continuously injected into the reactor while the electric tube furnace provides energy to the pyrolysis reaction. The carbon-containing gas is broken apart first at the surface of the catalytic nanoparticles, then, the obtained carbon fragments are transported to the edges forming the multiwalled carbon nanotubes (CNTs) and/or carbon nanospheres (CNSs). Accordingly with Nyamori and Coville [30], the CNTs and CNSs were synthesized by controlling the carbon decomposition of acetylene over the catalyst using lower flow rate of acetylene for CNTs.

Table 1 Comparison of different synthesis methods of CNTs. (Taking from [31])

| Method | Reaction temperature (°C) | CNT length (µm) | CNT growth rate (µm/s) | CNT yield | CNT quality | CNT purity |
|----------------|---------------------------|-----------------|------------------------|-----------|-------------|------------|
| Arc discharge | 4000 | 1 | Up to 10^7 | Low | High | Low |
| Laser ablation | RT-1000 | 1 | 0.1 | Low | High | Med |
| CVD | 500-1200 | $0.1-10^5$ | 0.1-10 | High | Med | Med-High |

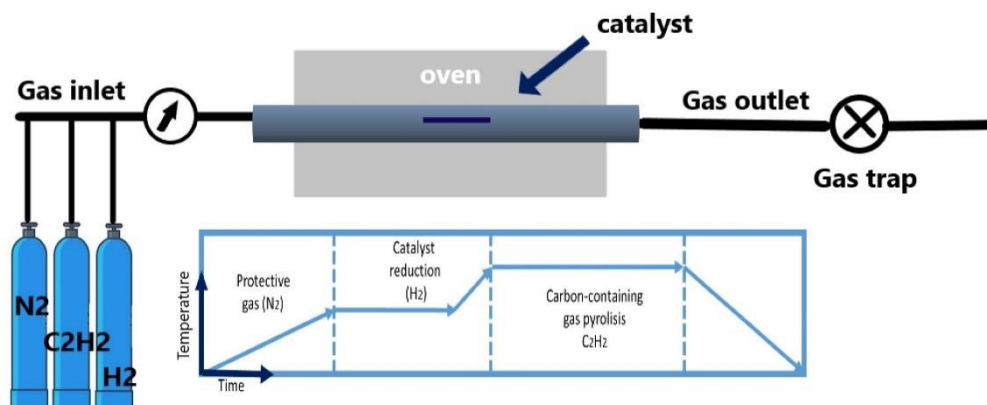


Figure 1: CVD experimental setup. The chamber reactor is heated by an electric furnace and the gases flow inside the chamber during the CVD process.

1.2.3. Ammonia oxidation catalyst

In order to functionalized with Ni the surface of CNTs and CNSs, the chemical reactivity and specificity of both were increased by wet oxidation using concentrated nitric acid and sulfuric acid (1:3 in volume ratio). The mixture was sonicated in a water bath for 2 h at 60 °C and let rest for 24 hours in the acid mixture. Afterward, the mixture was filtered and washed with deionized water until neutral pH. Finally, carbon nanostructures were dried in vacuum at 40 °C overnight.

The oxidized CNTs and CNSs were dispersed into 0.1 M aqueous solution of $\text{Ni}(\text{NO}_3)_2 \cdot 6\text{H}_2\text{O}$ and sonicated in a water bath at room temperature for 10 min, and

then, it was left to settle at room temperature. After impregnation and filtration, the mixture was dried at 40 °C for 10 h.

Finally, for the electrochemical test, two inks were made mixing 100 μL of Nafion with 5 mg of each modified carbon nanostructures and dispersed using an ultrasonic bath for 5 minutes. Then, 30 μl of the ink was dropped on to the graphite electrode and let dry for 20 min in an oven at 60°C.

1.3. CHARACTERIZATION METHODS

1.3.1. Thermogravimetric analysis (TGA)

TGA is an analytical technique used to determine a material's thermal stability and its fraction of volatile components by monitoring the weight change versus time while the sample is heated at a constant rate. TGA represents a useful tool to obtain information regarding thermal and oxidative stability, life expectancy, decomposition profile, moisture and volatiles content [32]. Thermal decomposition was performed using a TGA/DSC 2 STAR[®] system to evaluate thermal stability provided by Mettler Toledo. All the tests were performed using sealed alumina crucibles of 70 μL , heated from room temperature to 900 °C under oxidative atmosphere at temperature rate of 10 K/min.

1.3.2. Surface area and porosity

The surface area and porosity are important physical properties that are closely related to chemical activities of materials as well as product function, efficacy, and stability. Pore size analysis requires physisorption experiments where the manometric method is generally considered for undertaking physisorption measurements with nitrogen at cryogenic temperatures (i.e., 77 K, the boiling temperature of nitrogen). Physisorption is a general phenomenon that occurs whenever an adsorbable gas (the adsorptive) is brought into contact with the surface of a solid (the adsorbent), and its counterpart is desorption, which denotes the converse process, in which the amount adsorbed progressively decreases [33]. Adsorption hysteresis arises when the adsorption and desorption curves do not coincide [33]. The proposed updated classification of physisorption isotherms and hysteresis loops recommended by the IUPAC in 2015 [33] is shown in Figure 2.

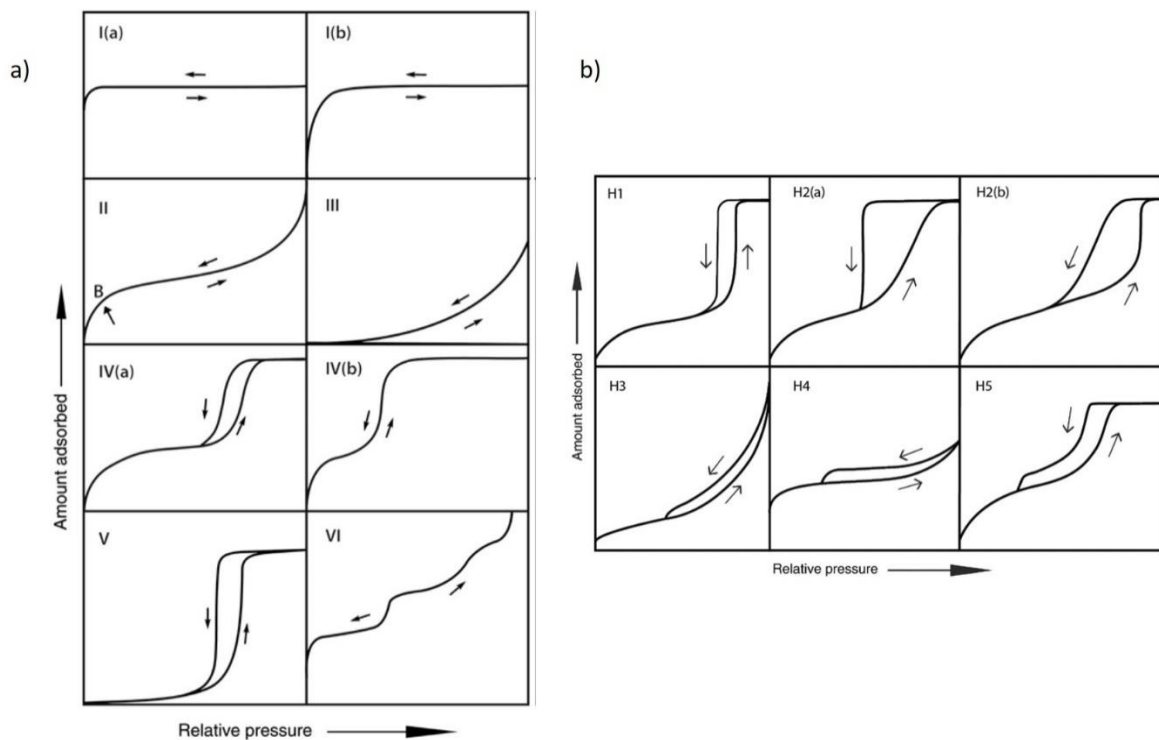


Figure 2 Classification of a) physisorption isotherms, and b) Hysteresis loops [33].

The type I isotherms are given by microporous solids having relatively small external surfaces, type II isotherms are given by the physisorption of most gases on nonporous or microporous adsorbents. In the case of a Type III isotherm the adsorbent-adsorbate interactions are relatively weak, and the adsorbed molecules are clustered around the most favorable sites on the surface of a nonporous or macroporous solid, and type IV isotherms are given by mesoporous adsorbents. Each of the six characteristic types of hysteresis loops is closely related to particular features of the pore structure and underlying adsorption mechanism. The Type H1 loop is found in materials which exhibit a narrow range of uniform mesopores, the type H2 can be attributed either to pore-blocking/percolation in a narrow range of pore necks or to cavitation-induced evaporation, the Type H3 loop are given by non-rigid aggregates of plate-like particles (e.g., certain clays) but also if the pore network

consists of macropores which are not completely filled with pore condensate. The H4 loop is a composite of Types I and II, the more pronounced uptake at low p/p_0 being associated with the filling of micropores. H4 loops are often found with aggregated crystals of zeolites, some mesoporous zeolites, and micro-mesoporous carbons. Although the Type H5 loop is unusual, it has a distinctive form associated with certain pore structures containing both open and partially blocked mesopores.

The Brunauer–Emmett–Teller method (BET) and Barrett, Joyner, and Halenda (BJH) methods are commonly used for evaluating the surface area of porous and finely-divided materials. BET surface area measurement and porosity of the samples were determined from nitrogen adsorption-desorption isotherms using a Quantachrome Autosorb iQ C-XR device. The N_2 adsorption was measured at liquid N_2 temperature and with relative pressure range from .0071 to 0.2. The BJH method was applied to the desorption branch of the N_2 adsorption isotherms to obtain the pore size distribution curves and cumulative volume of pores.

1.3.3. Scanning Electron Microscopy (SEM)

SEM is a powerful instrument that gives a direct view of the solid under study. Is frequently used to study nanomaterials to obtain data about the shape, size, homogeneity, etc. Produces images of a sample by scanning the surface with a focused beam of electrons. The electron beam is scanned in a raster scan pattern, and the position of the beam is combined with the intensity of the detected signal to produce an image. Here was analyzed the morphology of the nanomaterials by SEM using a JEOL JSM -7610F brand equipment. All the samples were dispersed in ethanol and a drop was deposited in a silicon wafer to analyzed.

1.3.4. X-ray powder diffraction (XRD)

XRD becomes a fundamental technique enabling us to evaluate: the nature of crystalline phases, their concentration in the solid and the crystallite size. Is based on constructive interference of monochromatic X-rays and a crystalline sample that satisfy Bragg's law. This law relates the wavelength of electromagnetic radiation to the diffraction angle and the lattice spacing in a crystalline sample. These diffracted X-rays are then detected, processed and counted. By scanning the sample through a range of 2θ angles, all possible diffraction directions of the lattice should be attained due to the random orientation of the powdered material. Conversion of the diffraction peaks to d-spacings allows identification of the mineral because each mineral has a set of unique d-spacings. Typically, this is achieved by comparison of d-spacings with standard reference patterns. The XRD patterns were obtained in a Rigaku Dmax2100 diffractometer using $\text{CuK}_{\alpha 1,2}$ ($\lambda = 1.5406/1.5442 \text{ \AA}$) radiation.

1.3.5. Spectroscopic methods

Spectroscopy can be based on phenomena of emission, absorption, fluorescence or scattering. Different spectroscopic methods are frequently used for the characterization of a wide range of materials.

- **Raman spectroscopy.** was named in the honor of its inventor, C.V. Raman, who, along with K.S. Krishnan, published the first paper on this technique[34]. It is based on the inelastic scattering of incident

radiation through its interaction with vibrating molecules. It probes the molecular vibrations. In Raman spectroscopy, the sample is illuminated with a monochromatic laser beam which interacts with the molecules of sample and originates a scattered light[35]. Raman spectroscopy was performed using a Lab RAM HR Evolution Raman spectrometer from Horiba. For the Raman measurements, a He-Ne excitation laser of 632.8 nm was used, with 2 mW of power through 50X LD lens and 2 μm spot to avoid photo decomposition of the samples.

- **Fourier Transform Infra-Red (FTIR) spectroscopy** is a well-established technique for the identification and structural analysis of chemical compounds. The peaks in the IR spectrum of a sample represent the excitation of vibrational modes of the molecules in the sample and thus are associated with the various chemical bonds and functional groups present in the molecules. Thus, the FTIR spectrum of a compound is one of its most characteristic physical properties and can be regarded as its "fingerprint." Infrared spectroscopy is also a powerful tool for quantitative analysis as the amount of infrared energy absorbed by a compound is proportional to its concentration[36]. (FTIR) was used to evaluate the presence of functional groups and nickel on the carbon nanostructure surface with a Bruker IR Tensor 27 spectrophotometer using a wavenumber range of 400 to 4000 cm^{-1} , 24 swept cycles and 4 cm^{-1} of resolution.

1.3.6. Electrochemistry

Electrochemistry is the study of techniques that use electrical stimulation to analyze the chemical reactivity of a system. The objective of electrochemical systems is the analysis of the electrode/electrolyte interface and the events that occur there when an electric potential is applied and current passes. An electrode is a material in which electrons are the mobile species and therefore can be used to sense (or control) the potential of electrons and an electrolyte is a material in which the mobile species are ions and free movement of electrons is blocked [37].

Electroanalysis comprises ‘static’ and ‘dynamic’ techniques (see Figure 3). The potentiodynamic techniques are all those techniques in which a time-dependent potential is applied to an electrode and the current response is measured. They form the largest and most important group of techniques used for fundamental electrochemical studies.

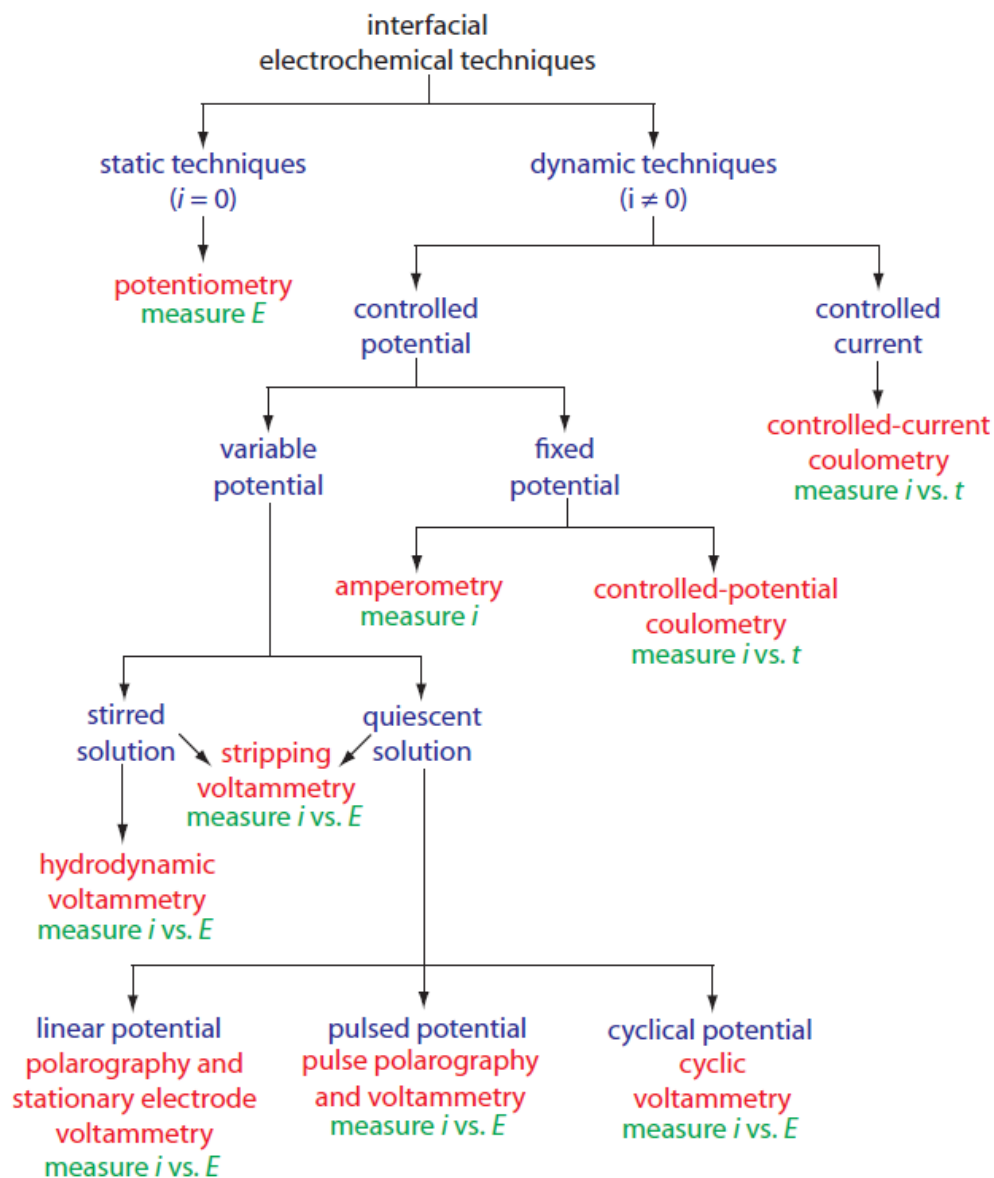


Figure 3 Interfacial electrochemical techniques. The specific techniques are shown in red, the experimental condition in blue, and the analytical signals in green. Taken from Analytical Chemistry 2.0 by David Harvey

[38].

- **Voltammetry** is a measurement of current as a function of controlled electrode potential and time. The resultant current-voltage display is commonly referred to as voltammogram. For a voltammogram, the scan is usually started at a potential where no electrochemical reaction occurs, then, at the potential where the charge transfer begins, a current can be observed which increases with the potential, however, after a maximum value (current peak) it starts to decrease due to the depletion of the reacting species at the interface [39].
- **Cyclic voltammetry** is commonly where the current response of an electrode to a linearly increasing and decreasing potential cycle is performed. Cyclic voltammetry is an excellent technique to survey the reactivity of new materials or compounds and can provide information about the potential at which oxidation or reduction processes occur, the oxidation state of the redox species, the number of electrons involved, the rate of electron transfer, possible chemical processes associated with the electron transfer, and adsorption effects [39].
- **Chronoamperometry** is an electrochemical technique in which the potential of the working electrode is stepped and the resulting current from faradaic processes occurring at the electrode (caused by the potential step) is monitored as a function of time. Chronoamperometry is used to study the kinetics of chemical reactions, diffusion processes, and adsorption. It can be also be used to monitor events [39].

For this thesis, all electrochemical experiments were achieved in a conventional three-electrode cell using a Voltalab PGZ402 potentiostat. As a working electrode, a glassy carbon electrode (5 mm of diameter) was used that was covered with a carbon nanostructure ink. From radiometer analytical, a platinum plate (B35M140) was used as a counter electrode and a saturated calomel electrode (SCE) as the reference electrode (B20B110) which was positioned as close as possible to the working electrode by means of a Luggin capillary. the selection of this electrode is because SCE is highly stable, but all potentials were calculated and reported versus Reversible Hydrogen Electrode (RHE). The RHE is subtype of the standard hydrogen electrodes, nonetheless its measured potential does not change with the pH making it a practical and reproducible electrode "standard", this is an important issue because all the references used different reference electrodes testing solution at different pH.

1.3.7. Chemical analysis

The concentrations of total nitrogen, total ammonia, and nitrate were measured with a Hach Lange spectrophotometer DR 2800, TNT 828 test for total nitrogen (20–100 mg/L), TNT 833 test for ammonia (47–130 mg/L $\text{NH}_3\text{-N}$, 60–167 mg/L NH_3) and TNT 836 for nitrate (5 – 35 mg/L $\text{NO}_3\text{-N}$, 22 – 155 mg/L NO_3). Nitrite was not measured, because in later bibliography ([26,28,29]) its concentration was reported very low (less than 1 mg/L).

RESULTS AND DISCUSSION

2.1. CVD CATALYST

In the chemical vapor deposition (CVD) process, the selection of the catalyst is a key factor in carbon nanostructures growth that define size and form. Even more, the performance of the synthesis is dependent on the rate of dissolution, diffusion, and precipitation of carbon atoms over the catalytic particles. Therefore, the choice of the catalyst and its preparation was thoroughly analyzed.

As was presented in chapter 2, CVD catalyst was synthesized by a sol-gel process to form ultra-fine powders that involve the hydrolysis of a metal alkoxide

(Tetraethyl orthosilicate, TEOS), followed by a cascade of condensation and polycondensation reactions [40]. The best thermal treatment was identified experimentally, based on the thermal decomposition of the liquid catalyst, by means of thermogravimetric analysis (TGA) and is shown in Figure 4.

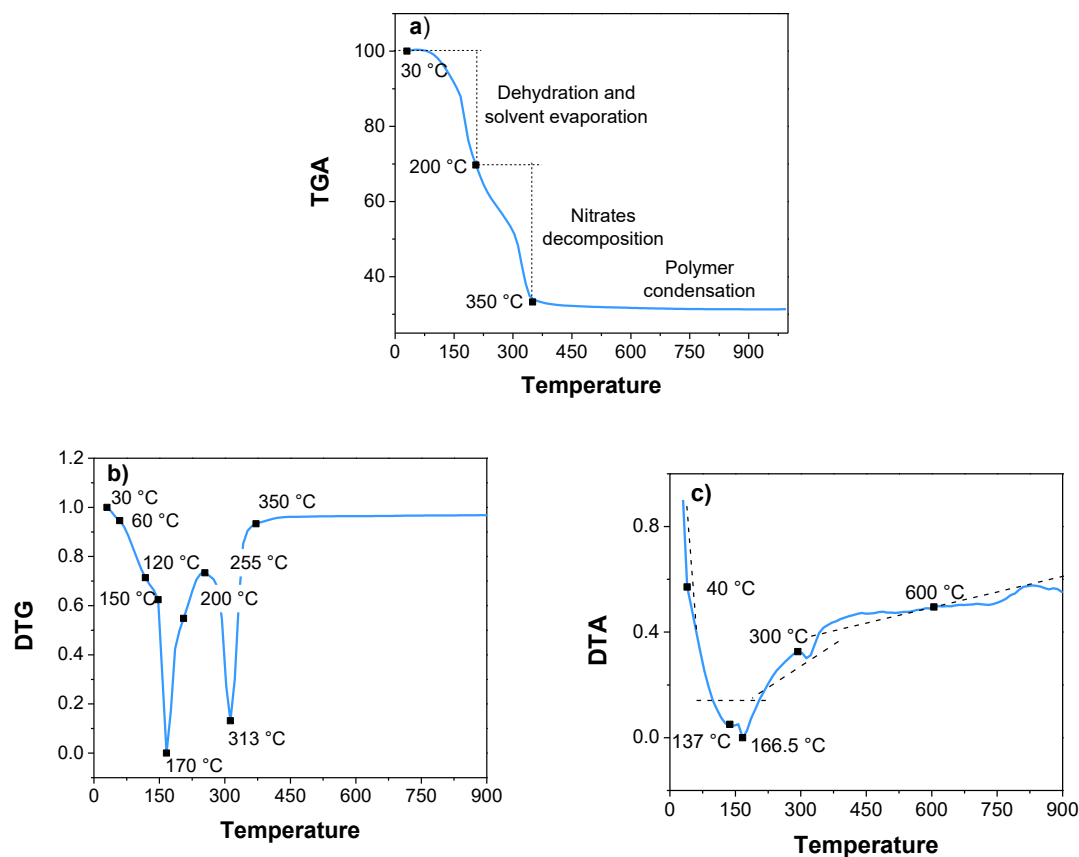


Figure 4 Thermo analysis of the liquid CVD catalyst a) TGA, b) DTG, and c) DTA.

The TGA reveals an accelerated mass loss between 30 °C and 200 °C. From the derivative thermogravimetry (DTG) is possible assigned this degradation process as the combination of individual steps, a partial dehydration and evaporation of the

solution containing the $\text{Fe}(\text{NO}_3)_3 \cdot 9\text{H}_2\text{O}$ and $\text{Ni}(\text{NO}_3)_2 \cdot 6\text{H}_2\text{O}$ salts, then is present the NO_3 degradation into nitrogen oxides and oxygen [41–44]. From 70 °C to 200 °C is the decomposition of HNO_3 , combined with the degradation of the nitrate from the $\text{Ni}(\text{NO}_3)_2$ in the range from 120 °C to 150 °C, and the nitrates from the $\text{Fe}(\text{NO}_3)_3$ around 150 °C to 170 °C [41–44]. The range between 170 °C to 200 °C, is caused by the removal of structural water from sol-gel matrix [41–44].

A second important mass loss in the TGA curve is present between 200 °C and 350 °C. From TDG the range between 200 °C and 255 °C is the oxidation process of iron to form Fe_2O_3 , then between 255 °C and 313 °C, is the formation of NiFe_2O_4 , and from 313 °C to 350 °C the formation of NiO [41–44].

At the same time in the differential thermal analysis (DTA), three endothermic peaks appear at 40 °C, 137 °C, and 166.5 °C. The first one is due to the partial dehydration of nitrates hydrates, the second one is due the decomposition of the nitrate from nickel salt, follow from the endothermic peak of nitrate decomposition from iron salt [41–44]. At 300 °C, there is a little exothermic peak caused by the combustion of the ethanol group of the silica matrix [45]. Finally, a broad exothermic peak is present-centered at 600 °C caused by the condensation polymerization of the sol-gel [45].

Because at 350 °C the solvent should be evaporated and the metals crystallized and oxidized, to obtain a powder of $\text{Fe}/\text{Ni}/\text{SiO}_2$, the sol-gel solution was transferred into rotative reactor set at this temperature for 3 h, at a slow heating rate of 0.5 °C/min and 25 rpm. Use of such a slow heating rate was to facilitate the

establishment of a silica network, as any cracks of the gel due to fast heating at this stage could cause the nitrate salts to leach out and decompose into oxides upon the subsequent heat treatment. Finally, the sample was calcinated at 650 °C for 3 h in order to achieve a completed condensation of silanols into siloxanes groups.

The X-ray diffraction pattern in Figure 5 of the product confirmed the exclusive presence of iron and nickel oxides (Maghemite- Fe_2O_3 , Bunsenite- NiO , and Trevorite- Fe_2NiO_4). Even more, the diffraction pattern presents fluorescence caused by the presence of Fe and Ni. The diffraction peaks were very broad, due to the low crystallinity of the three oxides.

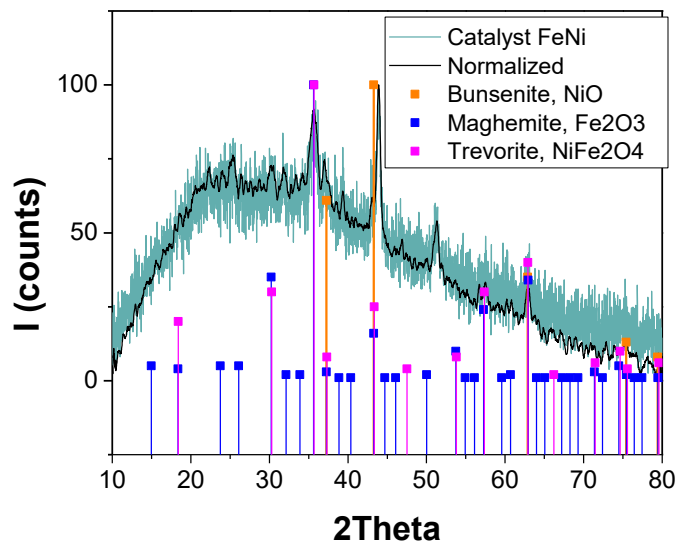


Figure 5 XRD pattern for oxide mixture use as CVD catalyst

Knowledge of morphological parameters such as surface area, pore-volume, area, and pore size distributions, is useful to comprehend the catalytic behavior in

the reaction environment. On one hand, the catalytic process takes place on the surface of the catalyst, then its area strongly affects the catalytic activity [33,46]. On the other hand, to reach the surface, the reagent molecules must run across the porous system, as well as the reaction products must leave the catalyst. Mass transfer process inside the granules depends on pore size (bulk diffusion in macropores, Knudsen diffusion in mesopores and molecular diffusion in micropores) and tortuosity factor. Therefore, the characterization of the catalyst powder was performed using the Brunauer–Emmett–Teller (BET) and Barrett, Joyner, and Halenda (BJH) methods.

In Figure 6 the BET isotherms of the FeNi catalyst is presented. The FeNi catalyst powder exhibits a Type IVa isotherm given by mesoporous adsorbents with two hysteresis loops. The first loop is typical of Type IVa, capillary condensation is accompanied by hysteresis and occurs for nitrogen adsorption at 77 K with pores wider than ~ 4 nm. The second loop is classified as type H5, this type is unusual because it has a distinctive form associated with certain pore structures containing both open and partially blocked mesopores. In the case of the CVD catalyst, this blocked mesopores could be caused by the presence of metal nanoparticles in the silica matrix.

The surface area of the catalyst was calculated as $25.489 \text{ m}^2/\text{g}$ with the data obtained from the BET analysis. BJH was used to analyze the size distribution desorption data, given a surface area of $32.347 \text{ m}^2/\text{g}$ a pore volume of 0.019 cc/g and a pore diameter of 1.184 nm . This values implies that the FeNi nanoparticles should

present high activity because for the size and morphology of the powder their surface area should be higher (with this test we analyzed the SiO₂ support and the metallic nanoparticles are embedded in it). Therefore, the acetylene pyrolysis should be efficiently catalyzed and, at the same time, we should have good carbon deposition on the catalyst to form the carbon nanotubes and spheres.

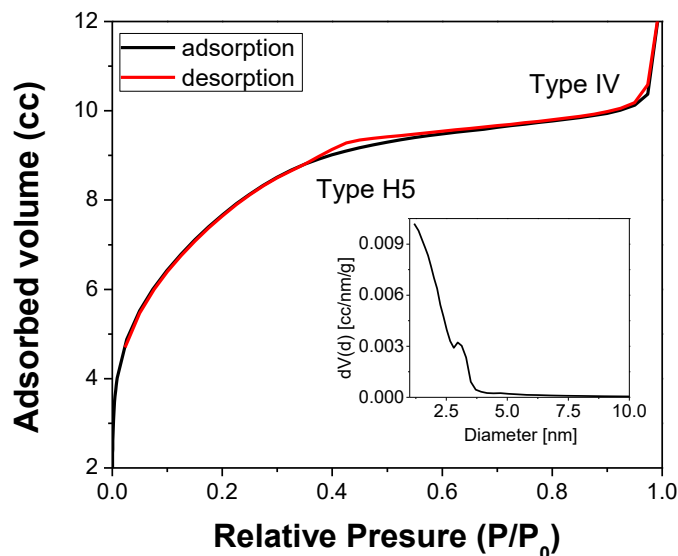


Figure 6 Nitrogen adsorption/desorption plot according to the BET model of the CVD catalyst. The inset is the BJH pore size distribution.

The catalyst mixture powder due to the milled process could present different sizes, then, a first attempted to classified it was based on particle size meshes of 65, 53, 45 and 38 μm openings, but all the material present lower sizes. Therefore, SEM was used to analyze the catalyst morphology, and the micrograph is shown in

Figure 7. The image shows a catalyst particle, the brighter dots are the metallic nanoparticles and the darker the SiO₂ support. All the metallic particle

present good distribution and similar sizes suggesting that the carbon nanostructures will be grown with almost the same diameter all over the particle catalyst forming dense groups.

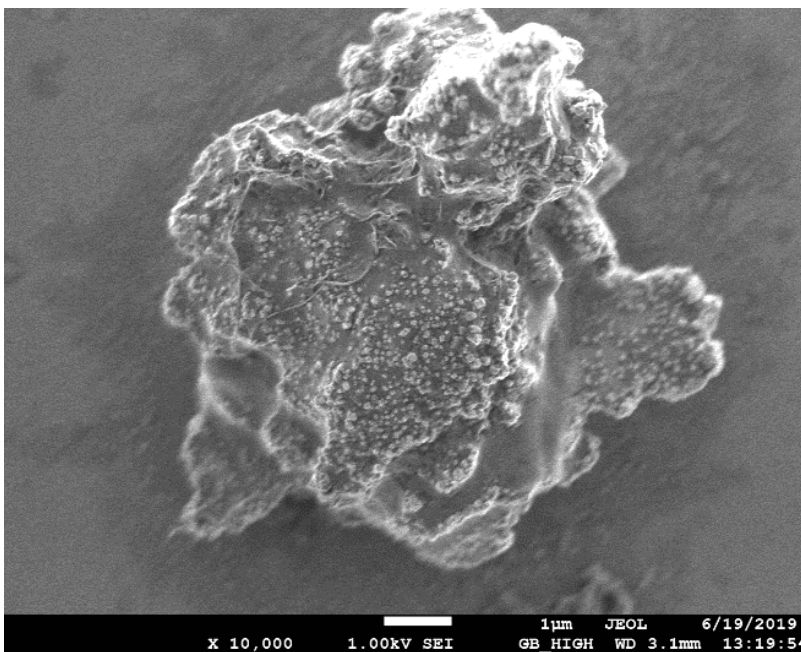


Figure 7. SEM micrograph of a CVD catalyst powder, the bright dots are the metallic nanoparticles and the darker the SiO₂ support.

2.2. CARBON NANOSTRUCTURES

Carbon nanostructures are generally produced from hydrocarbon-catalytic-decomposition over selected metal nanoparticles. By controlled decomposition of carbon-containing reactants over the metal catalyst, the carbon nanostructure-morphology can be controlled too, meaning, under appropriate conditions can be defined the shape, length, diameter, and even more, change their physical and chemical properties. For instance, low metal-carbon relation generates carbon

nanospheres (CNSs), while high metal-carbon relation produces carbon nanotubes (CNTs).

Then, follow the process described in chapter 2, the CNTs and CNSs were synthesized. A micrograph obtained by SEM is presented in Figure 8. As can be seen, CNSs tend to grow forming beads and grow separated from the catalyst, on the other hand, CNTs grow in bundles that wrap up the catalyst. When both samples are analyzed in detail, was found that they contain several kinds of heterogeneities:

- carbonaceous species like fullerenes, amorphous carbon, graphitic and carbon particles, etc;
- impurities such as residual metallic catalyst often protected by graphitized carbon shells or polyhedra;
- defects at the surface or oxygenated grafted functions,
- dispersion in diameter, chirality, and morphology (aspect ratio) and
- aggregation into bundles.

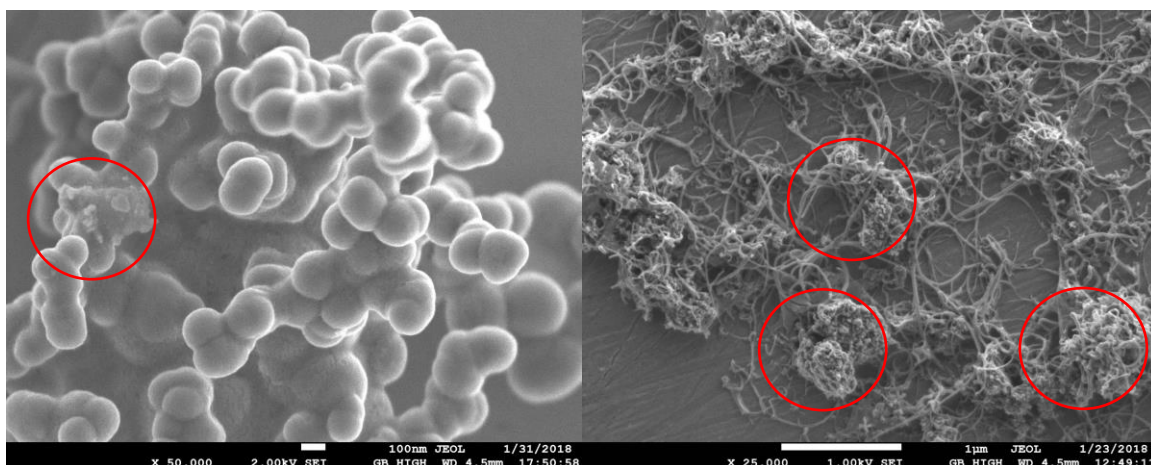


Figure 8 SEM of a) CNSs and b) CNTs. Was circulated some heterogeneities

2.3. CNT AND CNS AS CATALYST SUPPORT

The morphology and size of nanotubes and nanospheres suggest that they could be used as supports for heterogeneous catalysis or as templates for creating small wires or tubular structures by coating them with metals. Nevertheless, their use is limited due to their impurities, besides, the agglomeration (caused by strong inter-tube van der Waals forces) and their high surface energy (due to the strong curvature of the thin nanotubes) [47,48], difficult their solubility in solvents (either aqueous or nonaqueous) even after adding dispersing materials [49]. Then, a purification and a functionalization will be necessary.

The impurities are usually remove using concentrated acids (HNO_3 , HCl , H_2SO_4 or mixtures) or strong oxidants (KMnO_4 , H_2O_2) [50–52] by means of a selective oxidation process that separate the synthesis products as a function of their reactivity, wherein amorphous carbonaceous impurities and metallic-catalyst particles are easily oxidized at a faster rate than CNTs or CNSs [52,53]. Therefore, this process is called purification.

On the other hand, functionalization of CNTs involves the addition of chemical moieties on their surface improving the solubility and processability [47]. The first step to functionalize a carbon nanostructure is the formation of carboxyl surface groups by oxidation. The second one is the grafting of the oxidized surface with various functional groups to obtain more specific surface reaction [54].

Due to both carbon nanostructures will be used as catalyst supports for the ammonia oxidation reaction (AOR) using nickel as active catalyst electrode, we report in chapter 2, a general method in which the nanotube surface can be modified by oxidation to cover them by carboxylic (-COOH), carbonyl (-C=O) and hydroxyl (-COH) groups. The most important advantage is the fact that the presence of these groups should increase the chemical reactivity and specificity of the otherwise relatively inert carbon surface. The carboxylic groups on the surface would be used for ion exchange, replacing the proton with a nickel ion. This should give a very uniform coverage if the carboxylic groups are evenly spread on the nanostructure surface.

FTIR analysis was performed to evaluate the oxidation effect of the acid process onto the CNTs and the successful addition of nickel at the surface. This technique can identify, if they're present, which functional groups are on the surface of the CNTs. The spectrogram in Figure 9 shows the CNT-P spectra, where the peak at 1578 cm^{-1} is attributed to the vibration of the carbon skeleton (C-C stretching) of the carbon nanotube bulk [55,56]. The CNT-O spectra (Figure 9) shows a narrow band at 1382 cm^{-1} and wideband 3650 cm^{-1} attributed to the OH stretch mode in carboxylic acid groups, at 2930 cm^{-1} indicates the symmetric and asymmetric stretching of CH_2 , the band at 1631 cm^{-1} is assigned to characterize the C = O stretching of the carbonyl acid. Then, those results show that the carboxyl acid groups (-COOH) were bound to the CNT surface resulting from the acid treatment used [57–60]. The absorption peaks at 440 cm^{-1} are associated with Ni-O vibration bond but absorption bond at 645 cm^{-1} is assigned to Ni-O-H stretching bond.

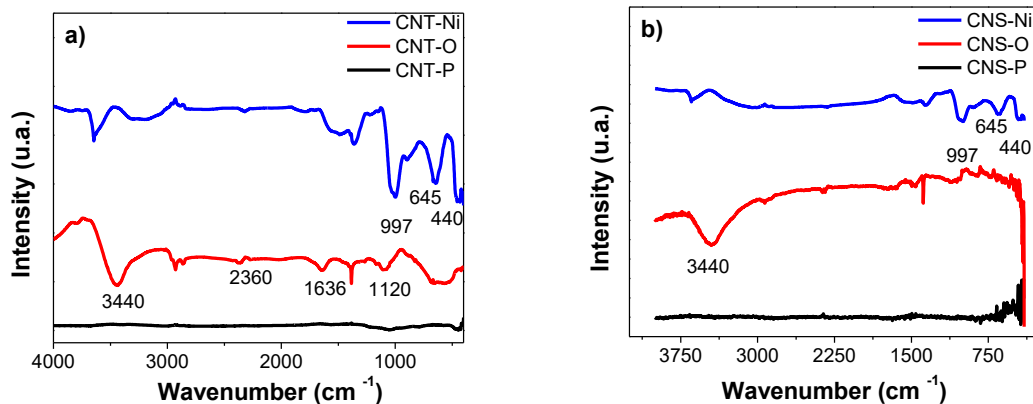


Figure 9 FT-IR spectrums from a) CNTs and b) CNSs. As grown (-P), after the oxidation process (-O) and after nickel decoration (-Ni).

Raman spectroscopy was used in the CNTs and CNSs before and after being modified in order to analyze structural changes caused by the oxidation process and functionalization with nickel. Figure 10 shows three characteristic Raman peaks. The first one is called D band, generally attributed to the presence of disordered carbon in the graphite and is identified around 1330 cm^{-1} . The second peak is named G band, is associated with the sp^2 hybridization vibration in a two-dimensional hexagonal lattice and reflects the structural integrity of the nanotubes, are located around 1590 cm^{-1} . The third peak, known as G' band is characteristic of double resonance induced by disorder and defects (overtone of D band), is found around 2630 cm^{-1} and is also inversely proportional to the number of graphitic layers that formed the carbon nanostructure. Besides, in agreement with bibliography [58,60–62] the relative degree of graphitization in the nanotubes could be evaluated by the intensity ratio of D to G bands (I_D/I_G). This value was calculated for both structures for the CNT-P was 1.62, for CNT-O was 0.83, and for CNT-Ni was 1.055 while for CNSs was 1.47, 0.96 and 1.33 before oxidation, after oxidation, and after the functionalization with nickel

respectively. In Figure 10 the changes in the I_D/I_G ratio caused by the oxidation process was due to the removal of the amorphous carbon for the surfaces. The same when nickel was added the nickel nanoparticles modify the spectra causing not only changes in the I_D/I_G ratio but also a slight fluorescence that causes broadness in the spectra.

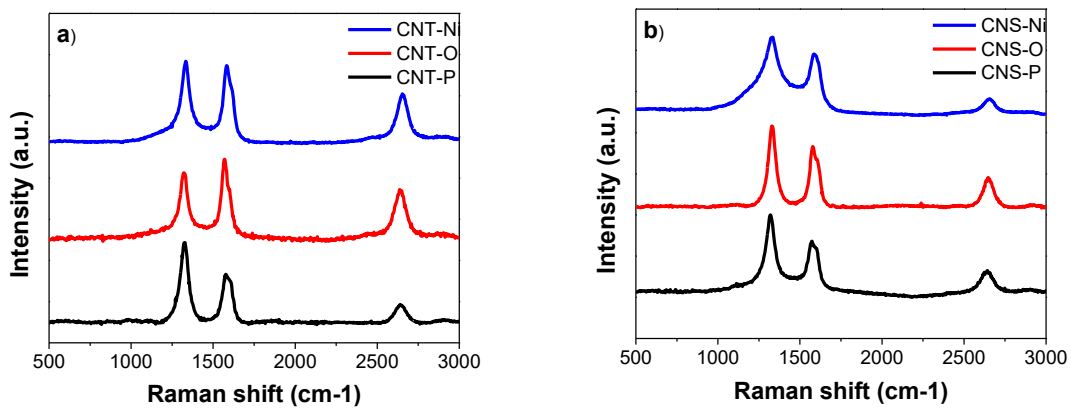


Figure 10 Normalized Raman spectra of a) CNTs and b) CNS. Both nanostructures were analyzed as-grown (-P), after the oxidation process (-O) and after add nickel onto their surface walls (-Ni).

The CNTs and CNSs after the functionalization with nickel are shown in Figure 11, in there a film formed by nickel is surrounding both carbon nanostructures making them wider and more thermally stables.

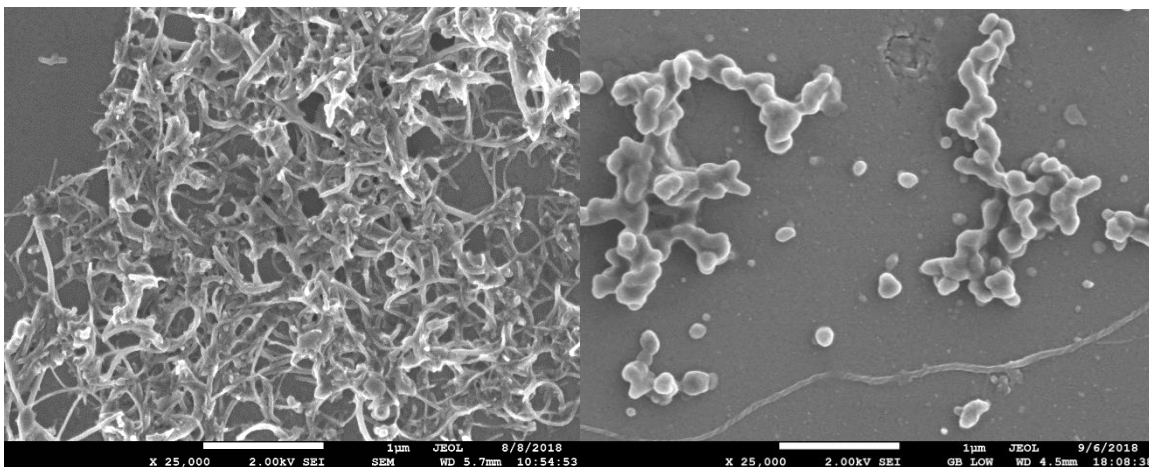


Figure 11 Micrograph obtained of a) CNTs and b) CNSs after been functionalized with nickel.

2.4. NICKEL AS AOR ELECTROCATALYST

The electrode material is clearly an important parameter in electrosynthesis since the mechanism and the products of some electrode reactions are known to depend on the material of the electrode and, indeed, in certain cases on the method of preparation of the electrode surface. Here, the oxidation state of Ni at the electrode surface is very important and determines the electrode's performance, for instance the surface of nickel in alkaline solutions is covered spontaneously and passivated against corrosion with nickel hydroxide. The hydroxide called α -Ni(OH)₂ is formed at the initial stage on the electrode at this potential range ($-0.20 \leq E \leq 0.5$ V vs. RHE) [64,65] but tend to change into β -Ni(OH)₂ irreversibly by increasing the potential or after some time [64–66]. Therefore, after a sequential discharging process the lack of α -Ni(OH)₂ inhibits the catalytic activity when is used at this particular potential. Thus, nickel is prefer to use in alkaline systems at the potential range where β -Ni(OH)₂ is oxidized into nickel oxyhydroxide (β -NiOOH) at 1.45 V vs RHE.

CNT-Ni and CNS-Ni were analyzed through cyclic voltammetry as water electrolyzers by expanding the potential window gradually to observe and determine the relationship between oxidation and reduction reactions taking place on the catalyst surface. As shown in Figure 12, a couple of redox peaks are clearly observed in the CV curve of both catalysts electrodes caused by the reversible cycling between $\text{Ni}^{2+}/\text{Ni}^{3+}$ [64–66]. But while the potential window is increasing two new redox peaks appear corresponding to the onset potential for the OER and the onset potential for the HER. The result indicates that both nanoparticles can be used as a redox catalyst to alkaline water electrolysis process. Nevertheless, as was presented in chapter 2, ammonia requires 95% less energy to be electrolyzed. Therefore, was analyzed this process.

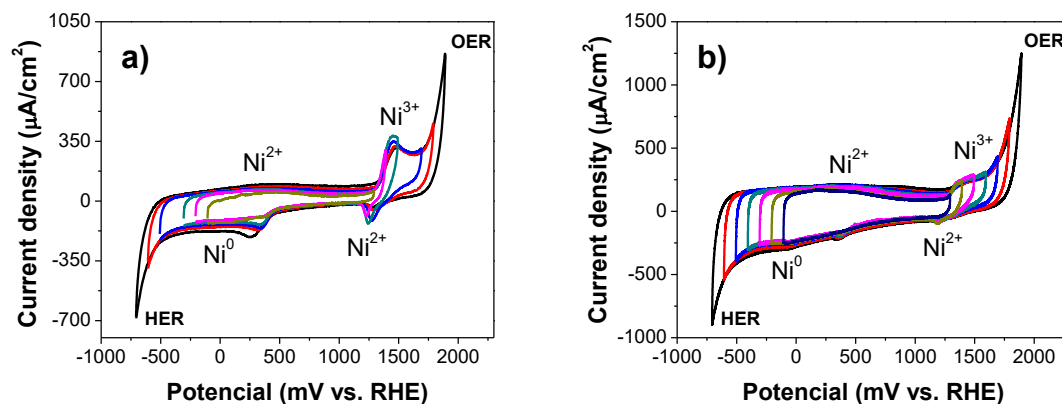


Figure 12 CV recorded in 10 mM solution of K_2SO_4 with pH adjusted with KOH at 11 and 25 mV/s. a) CNT-Ni and b) CNS-Ni

2.5. AMMONIA OXIDATION PROCESS

The dissociation process of ammonia (NH_3) and ammonium ions (NH_4^+) in aqueous solution is pH-dependent and is described by Vitse et al. [67] in Eq. (1) and represented in Figure 13, it shows how as the pH increases, the ionized NH_4^+ is liberated into gaseous NH_3 .

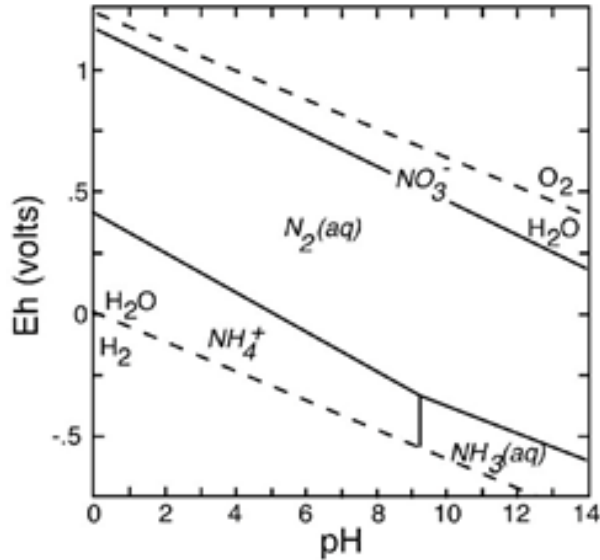
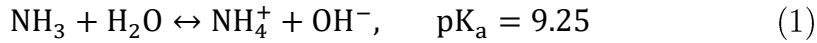
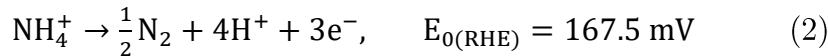
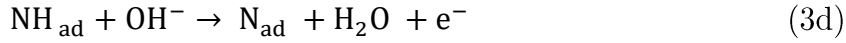
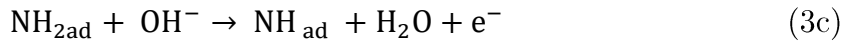
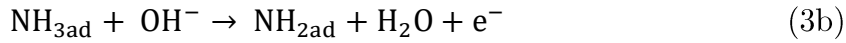
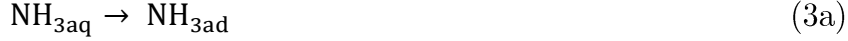


Figure 13 Pourbaix diagram showing the $\text{NH}_4^+ / \text{NH}_3$ equilibrium at pH 9.25 (ammonium's most interactive state) at 25°C . Taken from [68]

According to Eq. (1) at $\text{pH} = 7.25$, predominates NH_4^+ (99%), and the electrochemical process to form nitrogen [27] occurs as shown the Eq. (2)



On the other hand, when predominates NH_3 , at higher OH^- concentration, ammonia will be adsorbed onto the surface of the electrode, and then oxidized to N_2 ($E_{0(\text{RHE})}=1.4$ V at pH 11), as describe the mechanism proposed by Gerisher and Mauerer [69] in Eq.(3).



In order to define if Ni could catalyze the oxidation process of NH_3 or NH_4^+ or both, we take advantage of the pH equilibrium system of ammonia solutions. Figure 14 shows cyclic voltammograms recorded on CNT-Ni and CNS-Ni in the presence of 200 ppm of $(\text{NH}_4)_2\text{SO}_4$ in 100 mM K_2SO_4 at pH 7, 9 and 11. Between both graphs is evident again the better catalyst activity of CNS-Ni with higher anodic density current in the cathodic side, even more they show greater capacitance (the semi rectangular space between anodic scan and cathodic scan) which is effect of the higher electrical conductivity and the spherical shape.

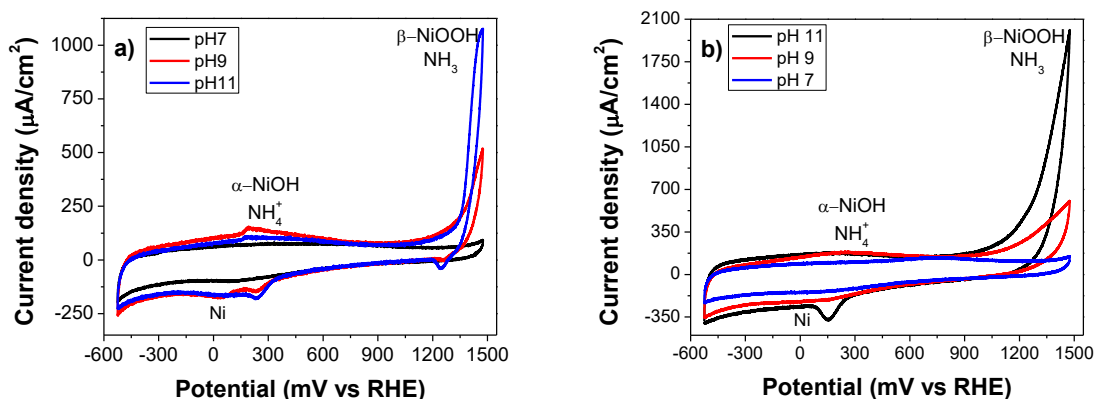


Figure 14 Cyclic voltammograms recorded on a) CNT-Ni and b) CNS-Ni in the presence of ammonia at various pH values; scan rate 100 mV/s; the solution contained 200 ppm of NH_3 and 10 mM of K_2SO_4 + KOH at pH 7, 9, and 11; temperature 25 °C.

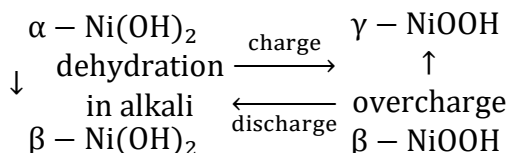
The curves show that the oxidation process is strongly pH-dependent and proceeds mainly at $\text{pH} > 7$. As the pH increases, the oxidation peak of ammonia increases. This result is in agreement with Kapalka et al. [26], demonstrating that Ni could catalyze the AOR, but it contradicts what found by Despic et al. [24], Yao et al. [25] and Candido et al. [27]. The most important difference is that when Ni does not present any catalytic activity [24,25] only was use ammonia without any ion support in the alkaline electrolyte. Only after add sulfate ion, perchlorate ion or chlorate ion ($(\text{NH}_4)_2\text{SO}_4$, NH_4ClO_4 or NH_4Cl) was notice the nickel activity. We could suggest an explanation here, as was proposed by Yu-Jen Shih et al. [28,29], the supporting electrolyte maintains constant conductivity necessary for operating the whole electrode system while minimizing other side effects, such as redox reaction of

background electrolyte species and gas evolution, i.e., O₂ at the anode and H₂ at the cathode.

Second, Candido et al. [27] also use (NH₄)₂SO₄ but they found, unlike us, activity for both NH₃ and NH⁴⁺ as show Figure 15. To explain it is important to understand the nickel behavior in alkaline solution against the potential.

When nickel gets in contact with a base solution, its surface is covered spontaneously with nickel hydroxide. The hydroxide called α -Ni(OH)₂ is formed at the initial stage on the electrode when is polarized in the potential (E) range of $-0.20 \leq E \leq 0.5$ V vs. the reversible hydrogen electrode (RHE) [64–66]. The α -Ni(OH)₂ is formed in anodic step and can be electrochemically reduced to metallic Ni; given a cathodic peak in the range $0.1 \leq E \leq -0.20$ V vs. RHE [64–66].

When the potential increases α -Ni(OH)₂ is transformed into β -Ni(OH)₂ irreversibly. The process is irreversible in the sense that a decrease of potential down into the region of HER does not convert β -Ni(OH)₂ back into α -Ni(OH)₂ nor reduces it to metallic nickel[64–66]. Nickel hydroxide has been reported that could be oxidized to nickel oxyhydroxide, which also presents two polymorphs structures (β and γ), the overall reaction pathway is illustrated in Scheme 1 [70].



Scheme 1: General reaction scheme of nickel in alkaline media initially taken from [70]. α -Ni(OH)₂ dehydrates in the concentrated alkali, forming β -Ni(OH)₂, while by charging process goes to γ -NiOOH, and β -Ni(OH)₂ into β -NiOOH.

From Figure 15a, if the reference electrode is adjusted from SCE to RHE ($E(\text{RHE}) = E(\text{SCE}) + 0.242 + 0.059 \text{ pH}$ at $T = 25 \text{ }^\circ\text{C}$), if we made a new graph this would overlap exactly with Figure 15b, thus, in order to oxidize NH_4^+ is necessary α -Ni(OH)₂ while for NH_3 is require the beta form.

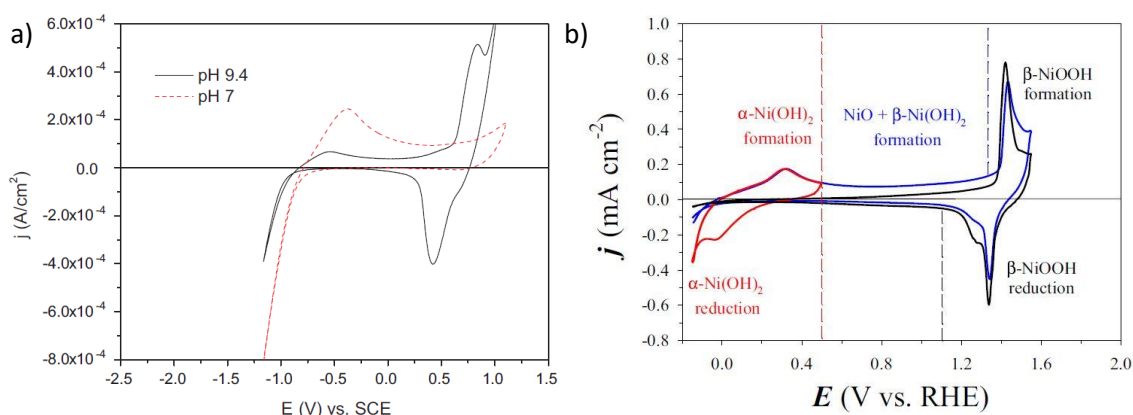


Figure 15 a) Cyclic voltammograms for Ni in 1000 ppm (NH₄)₂SO₄ + 1 M NaOH, pH 7 and pH 9.4. Take it from Candido et al. [27]. b) Three cyclic-voltammetry (CV) profiles for Ni(poly) electrode in 0.5 M aqueous KOH solution. Take it from Mohammad et al.[65].

This also explains why Yao [25] after some sequential discharging processes saw inhibited the activity of nickel because it tends to be rapidly converted to the thermodynamically more stable beta-phase material.

The redox characteristics of the CNT-Ni and CNS-Ni in a solution containing different amounts of ammonia nitrogen were evaluated by voltammetry in the presence of 10mM K₂SO₄, as inert electrolyte (at pH 11). In Figure 16 is shown the i-E response of the carbon nanostructures had a pair of peak potentials, anodic and cathodic, which were attributed to the formation and reduction of nickel oxyhydroxide (β -NiOOH). While NH₃ concentration increase the anodic peak current of β -NiOOH increased too, implying that the faradaic electron transfers of nitrogen species were mediated by the transition of β -Ni(OH)₂ to β -NiOOH. On the other hand, unlike the anodic peak, the reduction peak almost does not increase as the concentration of ammonia increases. This can be explained by the fact that the applied potential is now being split between two oxidation reactions (nickel and NH₃), and only is present the reduction of Ni in the cathodic region.

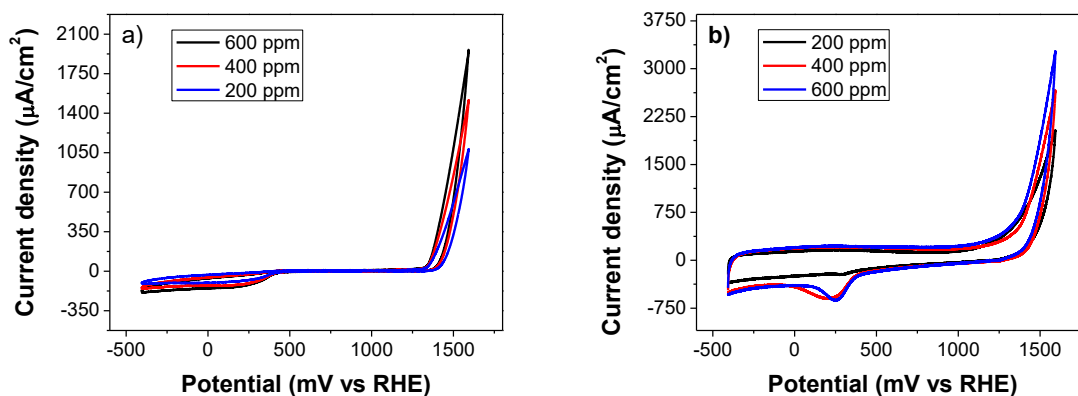


Figure 16 Cyclic voltammograms of CNT-Ni and CNS-Ni with 200 ppm, 400 mM, and 600 ppm of NH₃. Was added 10 mM K₂SO₄ as support electrolyte and KOH to adjust at pH 11 and 25 °C recorded at 100 mV/s.

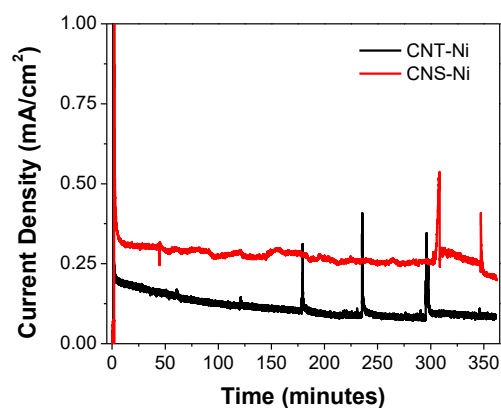


Figure 17 The current response of CNT-Ni and CNS-Ni using a polarization potential of 1.5 V vs RHE. The electrolyte used was 130 ppm of NH_3 at pH 11 and 25 °C. The peak variations were caused by electrolyte movements at the time of taking samples for the chemical analysis.

According to Ni Pourbaix diagram (Figure 18), $\text{Ni}(\text{OH})_2$ is known to passivate nickel and should avoid any further corrosion[71].

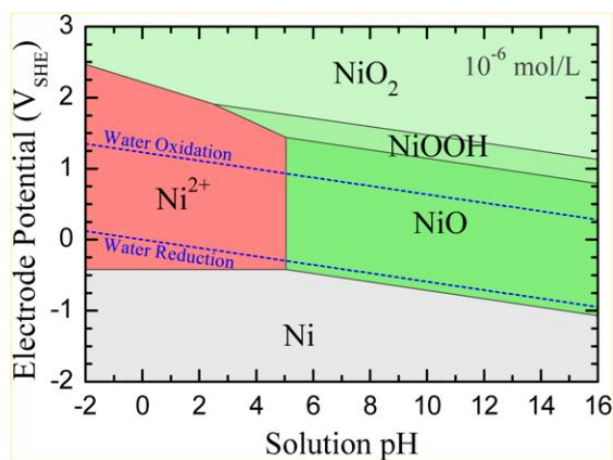


Figure 18 Electrode potential–pH (Pourbaix) diagrams, taken from [72]

Nevertheless, Kapalka et al. [26] notice corrosion of the electrode after performing a bulk electrolysis of 50 mM ammonia on the Ni/Ni(OH)₂ electrode in 1 M NaClO₄ at pH 11 after 12 h of the test, therefore, we tested our electrodes too using a chronoamperometric study. Figure 17 the current response of CNT-Ni and CNS-Ni electrodes after 6 hours, both electrodes were polarized at 1.5 V vs. RHE (approximately at oxidation point between Ni²⁺/Ni³⁺), using (NH₄)₂SO₄ as the electrolyte and the pH was adjusted at 11 using KOH. As can be seen, both electrodes are very stable in time, the current density variation came at the beginning as capacitance effect and then keeps almost constant, evidently CNS-Ni shows less variation than CNT-Ni due to, as was said early, present higher capacitance also this result indicates that the nickel hydroxide on both electrodes is not deactivated during ammonia oxidation. Even more, the electrodes were tested for more than 12 hours (not shown here) but we could not see any variation either in the current density nor at solution color. We suggest that the corrosion in Kapalka et al. [26] experiments are caused by the ClO₄ ions, those are known that can form coordination complexes with nickel, causing de-passivation and pitting corrosion.

The bulk electrolysis was simulated while was running the chronoamperometry using 130 ppm of ammonia on both electrodes at pH 11 and taking samples every hour for the chemical analysis with the Hach spectrophotometer. Figure 19 shows the concentration changes of total nitrogen, total ammonia, and nitrate during the electrolysis, in both graphics, the amount of

total nitrogen and ammonia continuously decreases whereas the amount of nitrate barely increases.

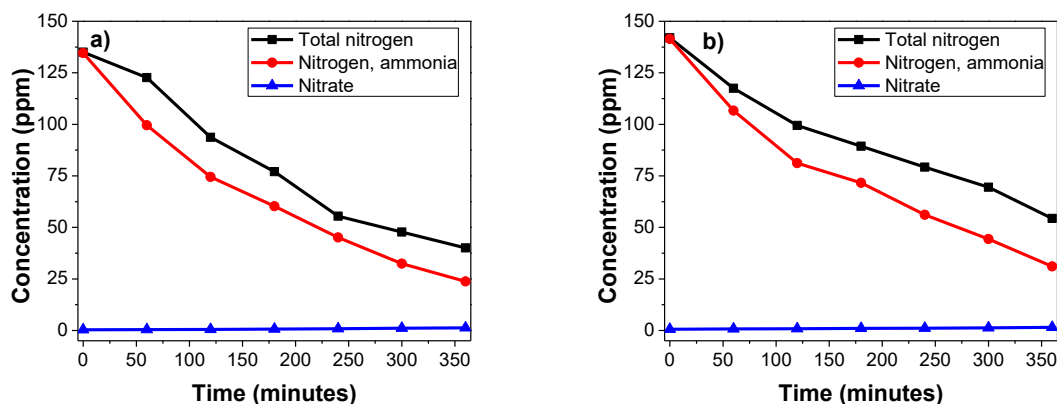


Figure 19 Concentration changes of nitrogen species (Total nitrogen, ammonia, and nitrate) at a constant potential of 1.5 V vs RHE as a function of reaction time. a) CNT-Ni with initial ammonia concentration of 135 ppm, b) CNS-Ni with initial ammonia concentration of 142 ppm. In both tests, pH was adjusted to 11.

At the end of the experiment for the electrolysis using CNT-Ni (after 6 h), 17.6% of the ammonia was degraded resulting in a degradation rate of 2.93 ppm/h. 0.9 % was recovered as nitrate, which leaves 13 % of the production as volatile N-species (N_2). When CNS-Ni was used after the same time, 21.8% of the ammonia was degraded at 3.63 ppm/h generating 1.1% of nitrate and 17.6 % as N_2 .

Comparing the electrolysis results obtained from both electrodes with Kapalka [26] shows higher efficiency because we do not present nickel corrosion and the amount of nitrate generated is lower (1.1 % vs 11 %). Those results are in agreement with Shih [28,29] where a nickel foam-supported $\text{Ni}(\text{OH})_2/\text{NiOOH}$ electrode was used to study the oxidation of ammonia in aqueous solution. The difference is the electrode size, they use a nickel foam (sheet, 2 mm of thickness, area density $\sim 250 \text{ g/m}^2$, holes number = 94 ± 10 pores per linear inch (PPI), Innovation Materials Co., Ltd., Taiwan) was the working electrode, while we use an ink with 0.196 cm^2 of diameter with surface area approximated of 120 g/m^2 to obtained the same results showing that the use of carbon nanostructures increase the catalytic activity.

The catalytic activity of the studied catalysts toward the AOR was performed by linear voltammetry, LV, using the rotating disk electrode (RDE) technique. A general approach to measure the standard rate constant (k_0) of both catalysts for the AOR was performed by a set of voltammograms at different rotation rates (Levich study) and then plot the reciprocal current (sampled at particular locations along the rising portion of each voltammogram) on a Koutecky-Levich plot. The linear sweep voltammograms for different rotation speeds, i.e., 400, 900, 1600 and 2500 rpm, measured at 5 mV/s 200 ppm of $(\text{NH}_4)_2\text{SO}_4 + 10 \text{ mM}$ solution of K_2SO_4 as supported electrolyte saturated with N_2 . Figure 20 shows that the limiting current density is directly proportional to the rotation rate in both cases, indicating a diffusion-controlled process.

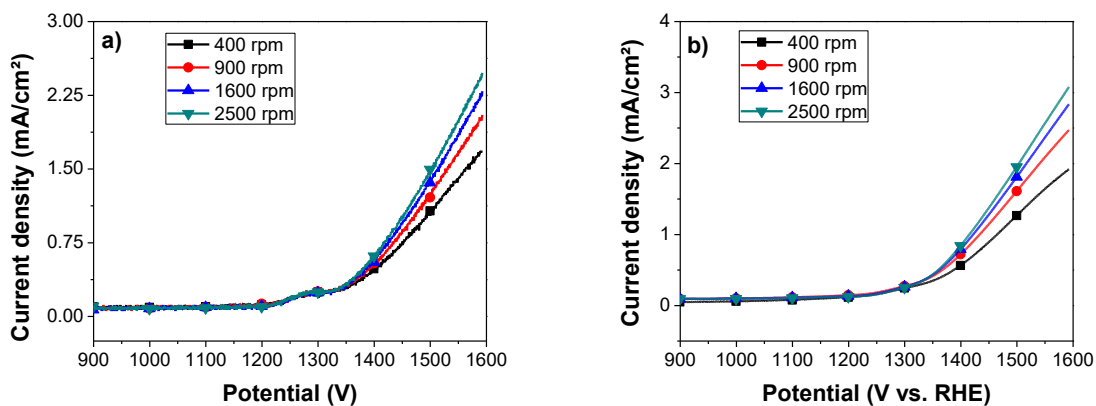


Figure 20 Linear sweep voltammograms of a) CNT-Ni and b) CNS-Ni. The electrolyte has 200 ppm of ammonia from $(\text{NH}_4)_2\text{SO}_4$ with 10 mM of K_2SO_4 as support electrolyte concentration and pH adjusted at 11.

A selection of Koutecky-Levich plots and their linear fits are shown in Figure 21. As is shown for both carbon nanostructures, the half-reaction is limited by sluggish kinetics rather than by mass transport, which is classical in the AOR. Even more, the fitted lines of the Koutecky-Levich plots from both nanocatalysts show good linearity and parallelism. This result indicates that the AOR process follows first-order kinetics respect to the concentration of ammonia and suggest the formation of nitrogen as the principal reaction product.

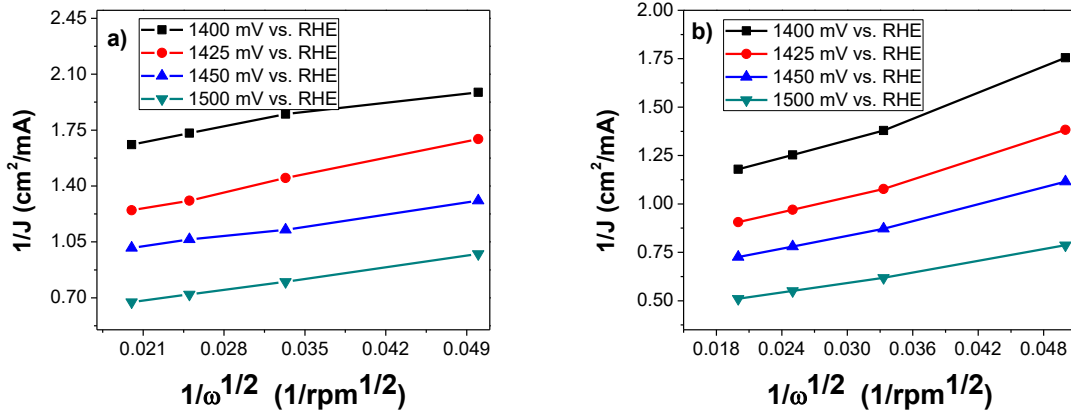


Figure 21 Koutecky-Levich plots for a) CNT-Ni and b) CNS-Ni

In this thesis until now, the CNTs and CNSs were pretreated to transform them into catalyst support by functionalization. The methodology proposed takes around 48 hours and includes a CVD synthesis (to growth the nanostructures), purification, and the metal decoration (functionalization with nickel). Nevertheless, both CNTs and CNSs present the ability to encapsulate other materials, such as metals and polymers, suggesting an improvement in catalytic applications. In literature, different synthesis methods have been modified to filled or doped (in-situ) the carbon nanostructures [7], [8], [11]–[13], [22]–[27]. Within, the approach of this investigation is to reduce the total time for synthesis and doping in CTNs and CNSs in a single-step CVD method that leaves Ni nanoparticles deposited between the walls of the CNTs and CNSs to form the nanocatalyst.

As was said early, carbon nanostructures were synthesized by the CVD process using nickel iron alloy (FeNi) powder prepared by the sol-gel process and using silica as support in a SiO_2 . The FeNi nanoparticles catalyzed the acetylene pyrolysis reaction, besides, acts as nucleation seeds, where the carbon precipitation at the ‘cold-end’ of the catalyst particle creates the CNTs or CNSs. Meanwhile, the catalyst

nanoparticles could be lifted by the growing carbon nanostructures or still adhere to the substrate surface, depending on the interaction between catalyst and substrate. Nevertheless, the catalyst nanoparticles should be present in metallic form, but some of them after the reduction process with the H_2/N_2 mixture remain as oxide, some of those will be lifted and encapsulated by the graphitic walls of the nanotubes or spheres as were reported by Haipeng Li et al. [29].

In order to analyze the possibility of have obtained encapsulated nanoparticles was used thermogravimetric analysis (TGA) that has shown to be a useful technique for the characterization of CNTs and CNSs [63]. Defects in nanotube walls increase the local reactivity, leading to lower temperature oxidation and gasification of the carbon, and manifesting itself in the TGA mass-loss profile. Considering that the oxidation process used to prepare the surface for the functionalization with nickel should eliminate the impurities, no carbonaceous or metallic impurities should be detected through the TGA profile. Nevertheless, the TGA curve in Figure 22a of both samples showed a similar oxidation behavior, with a single step degradation. In the beginning, at a temperature lower than 500 °C, neither CNTs nor CNSs show mass loss that should be occurred mainly due to the presence of amorphous carbon. Also, there is no gain mass. The weight gain occurs in samples where the metal particles are exposed to or are adhered on the surface regions of the sample and therefore were oxidized, this suggests that both carbon nanostructures were purified by the acid treatment. Finally, around 500 °C, a great mass loss is present, this is characteristic of the CNT and CNS decomposition. It was noted that approximately all the carbon should be gone but almost 40 % of the total mass in CNTs and 20 % in CNSs remained behind after performing TGA up to 800 °C.

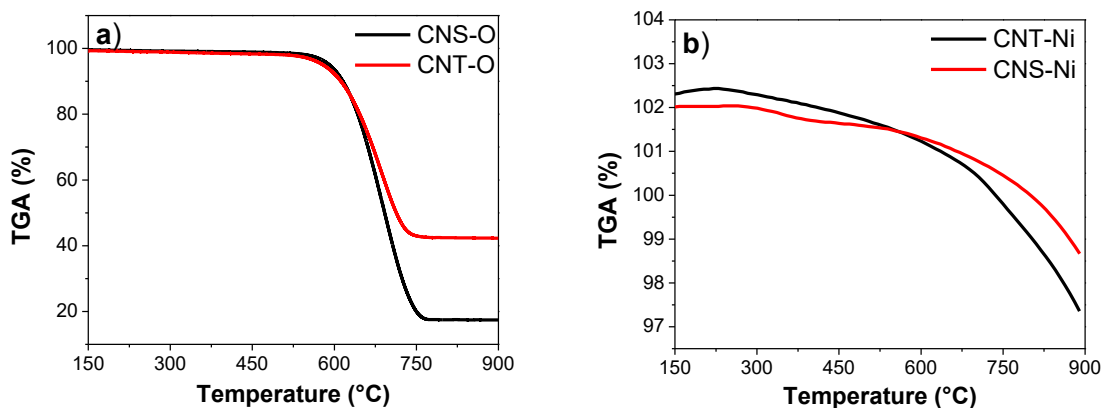


Figure 22 TGA performed over CNS and CNT under oxidant atmosphere. a) Analysis performed over the carbon nanostructures after the oxidation process, b) after the functionalization with nickel.

In Figure 22b is present how, after surface functionalization, both carbon nanostructures showed higher thermal stability, suggesting that either CNTs and CNS are completely covered with nickel.

To complement the analysis and define what is the remaining mass at Figure 22a was used SEM and STEM. In Figure 23 is shown the micrographs obtained from the CNTs and CNS after the oxidation process, here CNTs do not present agglomeration but their surface show some defects caused by the acids. Even more in the STEM image CNTs present some metallic particles encapsulated inside (darker dots). Those particles represent the mass remains in TGA. Since there was no weight gain observed during thermal treatment, the catalyst should be completely encapsulated and is rid of any external or tip catalytic particles, as evident from the STEM results. Looking at CNSs images they also present degradation in the surface and metallic nanoparticles distributed inside the nanostructures. There using a

magneto was confirmed that both nanostructures present magnetic properties offer by the metallic nanoparticles inside of them (Both Ni and Fe present ferromagnetic properties either in their metallic form and as oxide). Similar results were reported by Haipeng Li et al. [63].

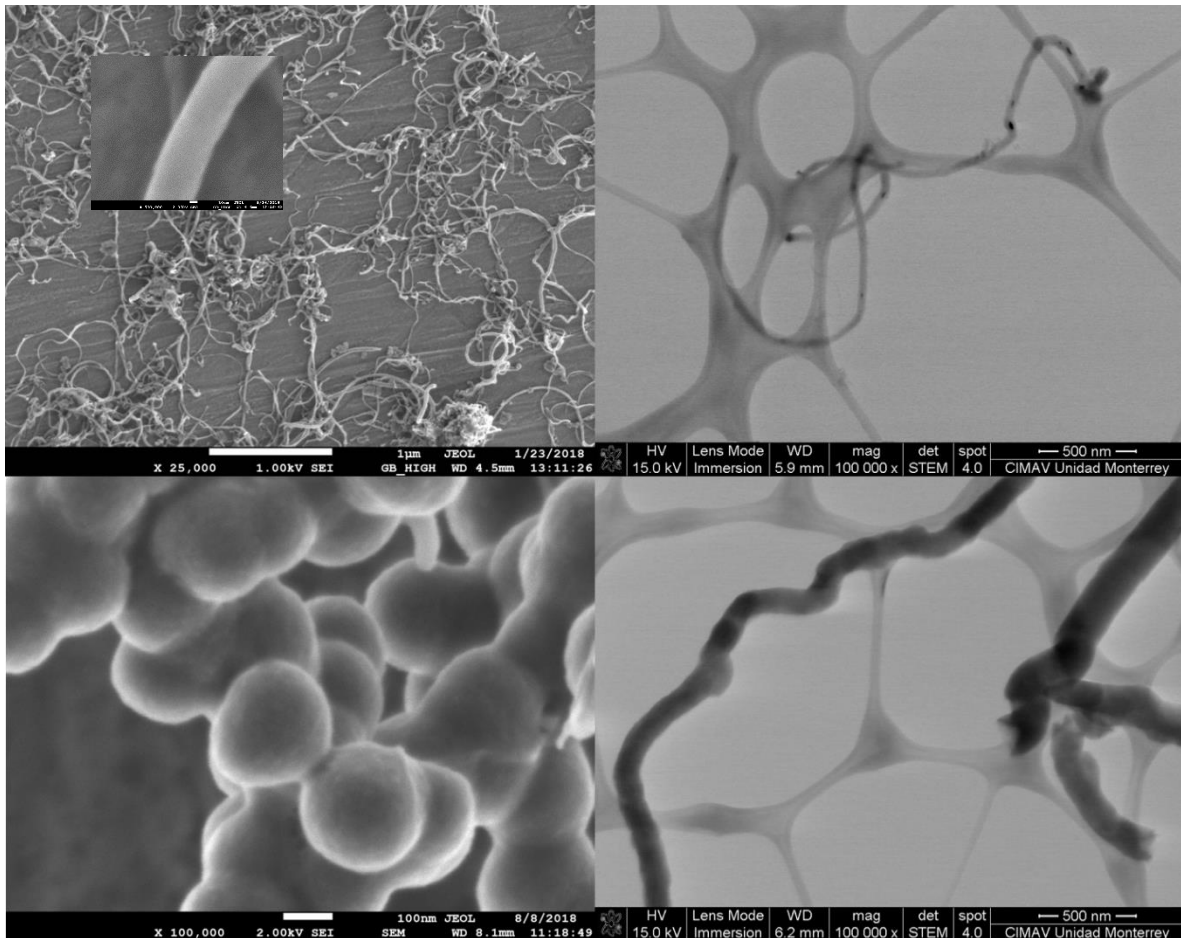


Figure 23 Micrograph obtained of CNTs and CNSs showing defects caused by the acid treatment and metallic particles encapsulated inside

To analyzed if the nanoparticles encapsulated presents catalytic activity for the AOR. An ink was prepared in the same way that was formulated before for the CNT-Ni and CNS-Ni and analyzed by cyclic voltammetry.

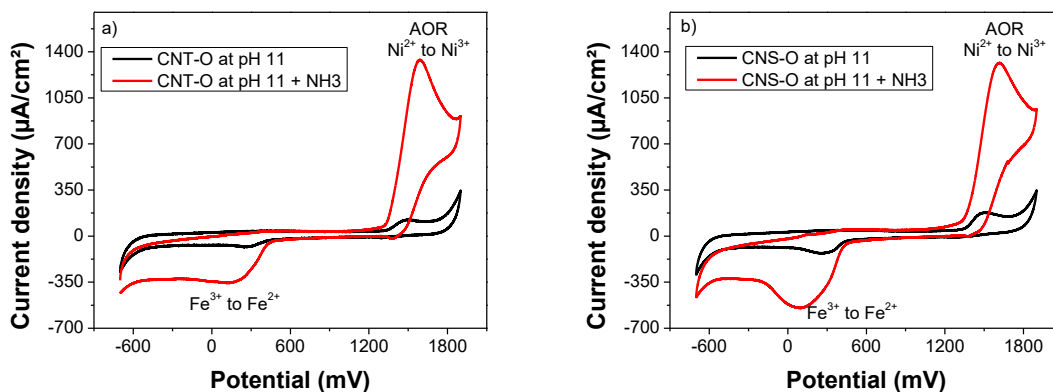


Figure 24 Cyclic voltammetry with and without 200 ppm ammonia using a) CNT-O as the electrode and b) CNS-O as the electrode.

Figure 24 shows in both carbon nanostructures that the CVD catalyst nanoparticles inside present catalytic activity for the AOR and in both cases is almost the same, the difference is that the iron component is most active in CNS-O but for the AOR does not present changes.

An important issue here is that CNT can be grown directly on a substrate as stainless steel that is conductor to use as electrode without the step of functionalization to decorate with the nickel and without preparing the ink and even more can grow aligned to improve their activity, this can be achieved by the CNS that grown separated from the substrate, even when was synthesized on the CNT they do not remain attach as is shown in the micrographs in Figure 25.

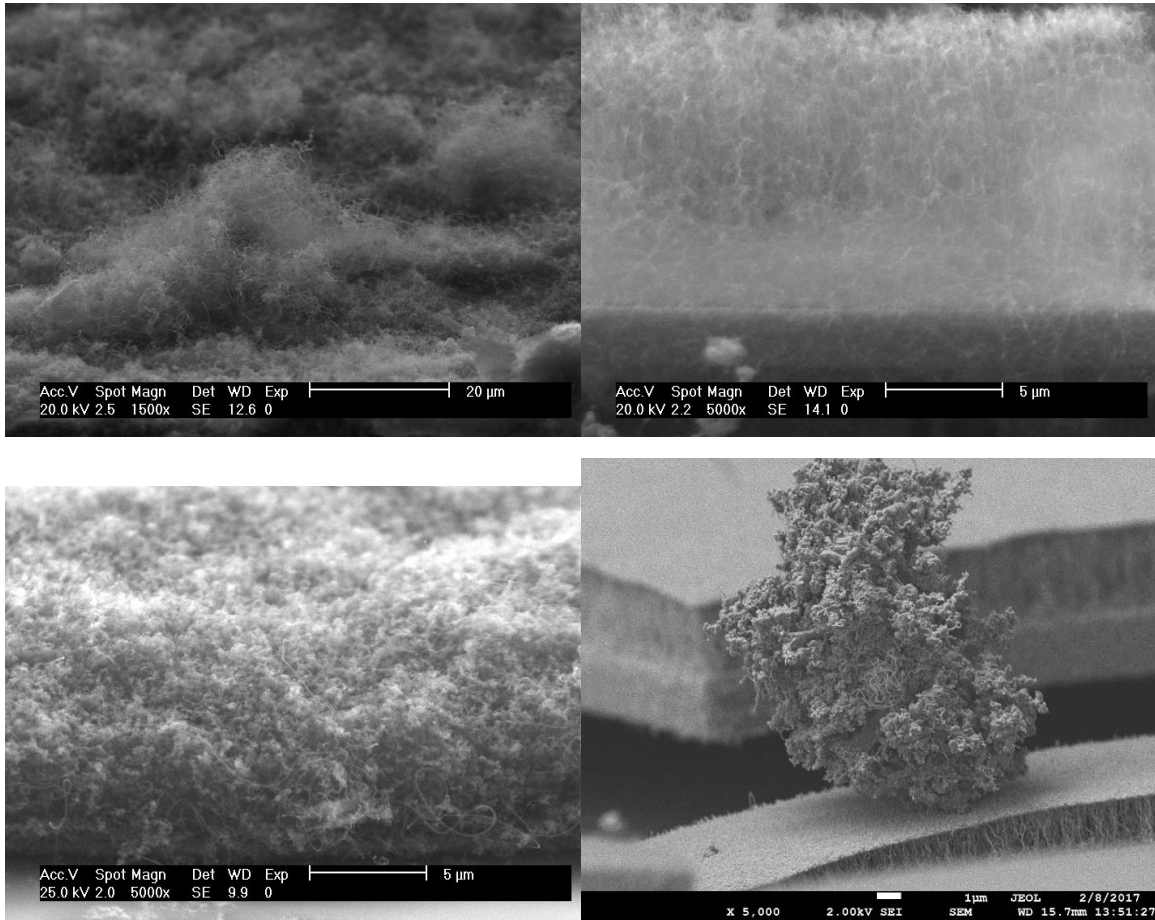


Figure 25 SEM of carbon nanostructures synthesized on stainless steel.
a) CNT entangled, b) CNT aligned (forest), c) CNS and d) CNT and CNS.

CHAPTER 5

CONCLUSIONS

Here, the synthesis methodology for two carbon nanostructures, carbon nanotubes and carbon nanospheres (CNT and CNS respectively) was presented. The synthesis method was defined through the analysis of the CVD catalyst that is a key part that defines sized, graphitic quality, etc. Our method in this study consists of the catalytic decomposition of acetylene over iron-nickel alloy particles supported on silica (SiO_2). Free carbon produced from the decomposition of acetylene aggregates around the metal particles and starts to grow to form CNTs or CNSs.

Both nanostructures show good applicability as nickel catalyst support (CNT-Ni and CNS-Ni) for the ammonia oxidation reaction (AOR). The AOR has been studied due to its promising applications in ammonia electrolysis, wastewater remediation, direct ammonia fuel cells, and sensors. And nickel was chosen because compared to other metals (Au, Pt, Ru, Co, In, Ir, Cu, etc.), Ni with higher natural abundance is economically feasible, suitable for numerous applications in batch, and presents low toxicity.

Results clearly demonstrated the successful decoration of CNTs and CNSs with Ni. The new Ni-electrodes were capable of directly oxidizing NH_3 to N_2 with high selectivity without overoxidation to NO_3 . The presence of NH_3 augmented the anodic current for the oxidation of metallic nickel to nickel oxyhydroxide, which suggested that the redox of Ni(II)/(III) on the surface of Ni mediated the electron transfer of ammonia nitrogen. After comparing both structures, CNS-Ni presents the best results for the AOR.

At the same time was analyzed why the conclusions given by the literature are contradictories, demonstrating that nickel is capable of oxidizing ammonia and ammonium ion depending on the oxidation state of the metal; $\alpha\text{-Ni(OH)}_2$ is required to oxidized NH_4^+ and $\beta\text{-Ni(OH)}_2$ for the NH_3 oxidation. Even more, was demonstrated that is necessary the use of electrolyte support but the use of chloride or perchloride should be avoided because they form complexes with nickel and caused its corrosion.

Even more, the carbon nanostructures were analyzed for the AOR without decorating their surface with nickel taking advantage of the CVD catalyst encapsulated inside showing better results the use of CNTs because they can be synthesized directly on a conductive substrate minimizing the time of production and with it the cost.

REFERENCES

- [1] W. Xu, R. Lan, D. Du, J. Humphreys, M. Walker, Z. Wu, H. Wang, S. Tao, Directly growing hierarchical nickel-copper hydroxide nanowires on carbon fibre cloth for efficient electrooxidation of ammonia, *Appl. Catal. B Environ.* 218 (2017) 470–479. doi:10.1016/j.apcatb.2017.07.005.
- [2] K. Siddharth, Y. Chan, L. Wang, M. Shao, Ammonia electro-oxidation reaction: Recent development in mechanistic understanding and electrocatalyst design, *Curr. Opin. Electrochem.* 9 (2018) 151–157. doi:10.1016/j.coelec.2018.03.011.
- [3] A.C.A. De Vooy, M.T.M. Koper, R.A. Van Santen, J.A.R. Van Veen, The role of adsorbates in the electrochemical oxidation of ammonia on noble and

- transition metal electrodes, *J. Electroanal. Chem.* 506 (2001) 127–137.
doi:10.1016/S0022-0728(01)00491-0.
- [4] H. Zhang, Y. Wang, Z. Wu, D.Y.C. Leung, An ammonia electrolytic cell with NiCu/C as anode catalyst for hydrogen production, *Energy Procedia.* 142 (2017) 1539–1544. doi:10.1016/j.egypro.2017.12.605.
- [5] Z.F. Li, Y. Wang, G.G. Botte, Revisiting the electrochemical oxidation of ammonia on carbon-supported metal nanoparticle catalysts, *Electrochim. Acta.* 228 (2017) 351–360. doi:10.1016/j.electacta.2017.01.020.
- [6] J.A. Herron, P. Ferrin, M. Mavrikakis, Electrocatalytic Oxidation of Ammonia on Transition-Metal Surfaces: A First-Principles Study, *J. Phys. Chem. C.* 119 (2015) 14692–14701. doi:10.1021/jp512981f.
- [7] K. Yao, Y.F. Cheng, Fabrication by electrolytic deposition of Pt-Ni electrocatalyst for oxidation of ammonia in alkaline solution, *Int. J. Hydrogen Energy.* 33 (2008) 6681–6686. doi:10.1016/j.ijhydene.2008.07.023.
- [8] M. Jiang, D. Zhu, X. Zhao, Electrolysis of ammonia for hydrogen production catalyzed by Pt and Pt-Ir deposited on nickel foam, *J. Energy Chem.* 23 (2014) 1–8. doi:10.1016/S2095-4956(14)60110-8.
- [9] A. Allagui, S. Sarfraz, E.A. Baranova, Ni_xPd_{1-x} (x = 0.98, 0.93, and 0.58) nanostructured catalysts for ammonia electrooxidation in alkaline media, *Electrochim. Acta.* 110 (2013) 253–259. doi:10.1016/j.electacta.2013.06.148.
- [10] K.W. Kim, Y.J. Kim, I.T. Kim, G. Il Park, E.H. Lee, The electrolytic decomposition mechanism of ammonia to nitrogen at an iridium oxide anode, *Proc. - Electrochem. Soc. PV 2004-18* (2004) 303–311.

doi:10.1016/j.electacta.2005.01.046.

- [11] S.K. Natarajan, D. Cossement, J. Hamelin, Synthesis and Characterization of Carbon Nanostructures as Catalyst Support for PEMFCs, *J. Electrochem. Soc.* 154 (2007) B310. doi:10.1149/1.2409867.
- [12] S.K. Natarajan, J. Hamelin, Electrochemical Durability of Carbon Nanostructures as Catalyst Support for PEMFCs, *J. Electrochem. Soc.* 156 (2009) B210–B215. doi:10.1149/1.3033517.
- [13] S. Shahgaldi, J. Hamelin, Improved carbon nanostructures as a novel catalyst support in the cathode side of PEMFC: A critical review, *Carbon N. Y.* 94 (2015) 705–728. doi:10.1016/j.carbon.2015.07.055.
- [14] A. Safavi, N. Maleki, M.M. Doroodmand, M.M. Koleini, Carbon nanostructures as catalytic support for chemiluminescence of sulfur compounds in a molecular emission cavity analysis system, *Anal. Chim. Acta.* 644 (2009) 61–67. doi:10.1016/j.aca.2009.04.024.
- [15] S.J. Park, S.Y. Lee, Hydrogen storage behaviors of platinum-supported multi-walled carbon nanotubes, *Int. J. Hydrogen Energy.* 35 (2010) 13048–13054. doi:10.1016/j.ijhydene.2010.04.083.
- [16] A. Abbaspour, E. Mirahmadi, Electrocatalytic activity of iron and nickel phthalocyanines supported on multi-walled carbon nanotubes towards oxygen evolution reaction, *Electrochim. Acta.* 105 (2013) 92–98. doi:10.1016/j.electacta.2013.04.143.
- [17] R.C. Sekol, X. Li, P. Cohen, G. Doubek, M. Carmo, A.D. Taylor, Silver palladium core-shell electrocatalyst supported on MWNTs for ORR in

alkaline media, *Appl. Catal. B-ENVIRONMENTAL*. 138 (2013) 285–293.
doi:10.1016/j.apcatb.2013.02.054.

- [18] M.A. Abdel Rahim, R.M. Abdel Hameed, M.W. Khalil, Nickel as a catalyst for the electro-oxidation of methanol in alkaline medium, *J. Power Sources*. 134 (2004) 160–169. doi:10.1016/J.JPOWSOUR.2004.02.034.
- [19] M. Grdeń, K. Klimek, EQCM studies on oxidation of metallic nickel electrode in basic solutions, *J. Electroanal. Chem.* 581 (2005) 122–131. doi:10.1016/j.jelechem.2005.04.026.
- [20] M. Vidotti, C.D. Cerri, R.F. Carvalhal, J.C. Dias, R.K. Mendes, S.I. Córdoba de Torresi, L.T. Kubota, Nickel hydroxide electrodes as amperometric detectors for carbohydrates in flow injection analysis and liquid chromatography, *J. Electroanal. Chem.* 636 (2009) 18–23. doi:10.1016/j.jelechem.2009.09.006.
- [21] V. Vedharathinam, G.G. Botte, Understanding the electro-catalytic oxidation mechanism of urea on nickel electrodes in alkaline medium, *Electrochim. Acta*. 81 (2012) 292–300. doi:10.1016/j.electacta.2012.07.007.
- [22] A.F.B. Barbosa, V.L. Oliveira, J. Van Drunen, G. Tremiliosi-Filho, Ethanol electro-oxidation reaction using a polycrystalline nickel electrode in alkaline media: Temperature influence and reaction mechanism, *J. Electroanal. Chem.* 746 (2015) 31–38. doi:10.1016/j.jelechem.2015.03.024.
- [23] M. Fleischmann, K. Korinek, D. Pletcher, THE OXIDATION OF ORGANIC COMPOUNDS AT A NICKEL ANODE IN ALKALINE SOLUTION, *J. Electroanal. Chem. Interfacial Electrochem.* 31 (1970) 39–49.

doi:10.1016/S0022-0728(71)80040-2.

- [24] A.R. Despić, D.M. Dražić, P.M. Rakin, Kinetics of electrochemical oxidation of ammonia in alkaline solution, *Electrochim. Acta.* 11 (1966) 997–1005. doi:10.1016/0013-4686(66)80038-5.
- [25] K. Yao, Y.F. Cheng, Investigation of the electrocatalytic activity of nickel for ammonia oxidation, *Mater. Chem. Phys.* 108 (2008) 247–250. doi:10.1016/j.matchemphys.2007.09.030.
- [26] A. Kapalka, A. Cally, S. Neodo, C. Comninellis, M. Wächter, K.M. Udert, Electrochemical behavior of ammonia at Ni/Ni(OH)₂ electrode, *Electrochem. Commun.* 12 (2010) 18–21. doi:10.1016/j.elecom.2009.10.026.
- [27] L. Candido, J.A.C.P. Gomes, Evaluation of anode materials for the electro-oxidation of ammonia and ammonium ions, *Mater. Chem. Phys.* 129 (2011) 1146–1151. doi:10.1016/j.matchemphys.2011.05.080.
- [28] Y.J. Shih, Y.H. Huang, C.P. Huang, Electrocatalytic ammonia oxidation over a nickel foam electrode: Role of Ni(OH)₂(s)-NiOOH(s) nanocatalysts, *Electrochim. Acta.* 263 (2018) 261–271. doi:10.1016/j.electacta.2018.01.045.
- [29] Y.J. Shih, Y.H. Huang, C.P. Huang, In-situ electrochemical formation of nickel oxyhydroxide (NiOOH) on metallic nickel foam electrode for the direct oxidation of ammonia in aqueous solution, *Electrochim. Acta.* 281 (2018) 410–419. doi:10.1016/j.electacta.2018.05.169.
- [30] V.O. Nyamori, N.J. Coville, Effect of ferrocene/carbon ratio on the size and shape of carbon nanotubes and microspheres, *Organometallics.* 26 (2007) 4083–4085. doi:10.1021/om7003628.

- [31] Z. Ren, Y. Lan, Y. Wang, *Aligned Carbon Nanotubes Physics, Concepts, Fabrication and Devices*, Springer Berlin Heidelberg, 2012. doi:10.1007/978-3-642-30490-3.
- [32] K.R. Rajisha, B. Deepa, L.A. Pothan, S. Thomas, Thermomechanical and spectroscopic characterization of natural fibre composites, *Interface Eng. Nat. Fibre Compos. Maximum Perform.* (2011) 241–274. doi:10.1533/9780857092281.2.241.
- [33] M. Thommes, K. Kaneko, A. V. Neimark, J.P. Olivier, F. Rodriguez-Reinoso, J. Rouquerol, K.S.W. Sing, *Physisorption of gases, with special reference to the evaluation of surface area and pore size distribution (IUPAC Technical Report)*, *Pure Appl. Chem.* 87 (2015) 1051–1069. doi:10.1515/pac-2014-1117.
- [34] C. V RAMAN, K.S. KRISHNAN, A New Type of Secondary Radiation, *Nature.* 121 (1928) 501–502. doi:10.1038/121501c0.
- [35] G.S. Bumbrah, R.M. Sharma, Raman spectroscopy – Basic principle, instrumentation and selected applications for the characterization of drugs of abuse, *Egypt. J. Forensic Sci.* 6 (2016) 209–215. doi:https://doi.org/10.1016/j.ejfs.2015.06.001.
- [36] A.A. Ismail, F.R. van de Voort, J. Sedman, Chapter 4 Fourier transform infrared spectroscopy: Principles and applications, *Tech. Instrum. Anal. Chem.* 18 (1997) 93–139. doi:10.1016/S0167-9244(97)80013-3.
- [37] A.J. Bard, L.R. Faulkner, *ELECTROCHEMICAL METHODS Fundamentals and Applications*, 201AD.
- [38] D. Harvey, *Analytical Chemistry 2.0—an open-access digital textbook*, *Anal.*

- Bioanal. Chem. 399 (2011) 149–152. doi:10.1007/s00216-010-4316-1.
- [39] A.J. Bard, G. Inzelt, F. Scholz, *Electrochemical dictionary*, Springer-Verlag Berlin Heidelberg, 2008. doi:10.1007/978-3-340-74598-3.
- [40] A.M.B. and M. Greenblatt, *The sol-gel Preparation of Silica Gels*, n.d.
- [41] A.Ó. Ma, R. Gajerski, S. Labus, B. Prochoswka-Klisch, K.T. Wojciechowski, MECHANISM OF THERMAL DECOMPOSITION OF d -METALS NITRATES HYDRATES, *J. Therm. Anal. Calometry*. 60 (2000) 17–23.
- [42] O.A. Cortez, F.J. Moura, E. de Albuquerque Brocchi, R.N.C. de Siqueira, R.F.M. de Souza, Fe-Ni Alloy Synthesis Based on Nitrates Thermal Decomposition Followed by H₂ Reduction, *Metall. Mater. Trans. B Process Metall. Mater. Process. Sci.* 45 (2014) 2033–2039. doi:10.1007/s11663-014-0221-x.
- [43] M.A.A. Elmasry, A. Gaber, K.M. H., THERMAL DECOMPOSITION OF Ni(II) AND Fe(III) NITRATES AND THEIR MIXTURE, *J. Therm. Anal.* 52 (1998) 489–495.
<http://weekly.cnbnews.com/news/article.html?no=124000>.
- [44] K. Wieczorek-Ciurowa, A.J. Kozak, The thermal decomposition of Fe(NO₃)₃×9H₂O, *J. Therm. Anal. Calorim.* 58 (1999) 647–651.
doi:10.1063/1.3253104.
- [45] S. Wang, L. Song, P. Chen, Y. Zhou, W. Nie, Weak acid-base interaction induced assembly for the formation of rambutan-like poly(styrene-alt-maleic anhydride)/silica composite microspheres, *Colloid Polym. Sci.* 292 (2014) 2465–2473. doi:10.1007/s00396-014-3278-9.

- [46] G. Leofanti, M. Padovan, G. Tozzola, B. Venturelli, Surface area and pore texture of catalysts, *Catal. Today*. 41 (1998) 207–219. doi:10.1016/S0920-5861(98)00050-9.
- [47] C.H. Lau, R. Cervini, S.R. Clarke, M.G. Markovic, J.G. Matisons, S.C. Hawkins, C.P. Huynh, G.P. Simon, The effect of functionalization on structure and electrical conductivity of multi-walled carbon nanotubes, *J. Nanoparticle Res.* 10 (2008) 77–88. doi:10.1007/s11051-008-9376-1.
- [48] M. Zhang, L. Su, L. Mao, Surfactant functionalization of carbon nanotubes (CNTs) for layer-by-layer assembling of CNT multi-layer films and fabrication of gold nanoparticle/CNT nanohybrid, *Carbon N. Y.* 44 (2006) 276–283. doi:10.1016/J.CARBON.2005.07.021.
- [49] C. Lifei, X. Huaqing, L. Yang, Y. Wei, Surface Chemical Modification of Multiwalled Carbon Nanotubes by a Wet-Mechanochemical Reaction, *J. Nanomater.* 2008 (2008). doi:10.1155/2008/783981.
- [50] R.A. Moraes, C.F. Matos, E.G. Castro, W.H. Schreiner, M.M. Oliveira, A.J.G. Zarbin, The effect of different chemical treatments on the structure and stability of aqueous dispersion of iron- and iron oxide-filled multi-walled carbon nanotubes, *J. Braz. Chem. Soc.* 22 (2011) 2191–2201.
- [51] A. Hirsch, O. Vostrowsky, Functionalization of carbon nanotubes, *Top. Curr. Chem.* 245 (2005) 193–237. doi:10.1007/b98169.
- [52] a. F. Ismail, P.S. Goh, J.C. Tee, S.M. Sanip, M. Aziz, a Review of Purification Techniques for Carbon Nanotubes, *Nano.* 03 (2008) 127–143. doi:10.1142/S1793292008000927.

- [53] P.-X. Hou, C. Liu, H.-M. Cheng, Purification of carbon nanotubes, *Carbon* N. Y. 46 (2008) 2003–2025. doi:10.1016/j.carbon.2008.09.009.
- [54] I.N. Burmistrov, D.S. Muratov, I.A. Ilinykh, E.A. Kolesnikov, A.Y. Godymchuk, D. V Kuznetsov, The effects of liquid-phase oxidation of multiwall carbon nanotubes on their surface characteristics, {IOP} Conf. Ser. Mater. Sci. Eng. 112 (2016) 12004. doi:10.1088/1757-899x/112/1/012004.
- [55] W. Zhao, M. Li, Z. Zhang, H.X. Peng, EMI shielding effectiveness of silver nanoparticle-decorated multi-walled carbon nanotube sheets, *Int. J. Smart Nano Mater.* 1 (2010) 249–260. doi:10.1080/19475411.2010.511477.
- [56] C. Jiang, H. Chen, C. Yu, S. Zhang, B. Liu, J. Kong, *Electrochimica Acta* Preparation of the Pt nanoparticles decorated poly (N -acetylaniline)/ MWNTs nanocomposite and its electrocatalytic oxidation toward formaldehyde, 54 (2009) 1134–1140. doi:10.1016/j.electacta.2008.08.071.
- [57] A. Mangone, R. Comparelli, M. Garzia Trulli, L.C. Giannossa, P. Favia, E. Sardella, S. Musso, G. Palazzo, F. Palumbo, Towards highly stable aqueous dispersions of multi-walled carbon nanotubes: the effect of oxygen plasma functionalization, *J. Colloid Interface Sci.* 491 (2016) 255–264. doi:10.1016/j.jcis.2016.12.039.
- [58] C.G. Silva, A.P.M. Tavares, G. Dražič, A.M.T. Silva, J.M. Loureiro, J.L. Faria, Controlling the surface chemistry of multiwalled carbon nanotubes for the production of highly efficient and stable laccase-based biocatalysts, *Chempluschem.* 79 (2014) 1116–1122. doi:10.1002/cplu.201402054.
- [59] Y. Jia, K. Yu, K. Qian, Facile approach to prepare multi-walled carbon

- nanotubes/graphene nanoplatelets hybrid materials, *Nanoscale Res. Lett.* 8 (2013) 1–6. doi:10.1186/1556-276X-8-243.
- [60] S. Osswald, M. Havel, Y. Gogotsi, Monitoring oxidation of multiwalled carbon nanotubes by Raman spectroscopy, *J. Raman Spectrosc.* 38 (2006) 728–736. doi:DOI: 10.1002/jrs.1686.
- [61] J. Li, Z. Zhao, X. Fan, Z. Yang, Y. Hu, Multiple functionalization of multiwalled carbon nanotubes with carboxyl and amino groups, *Appl. Surf. Sci.* 276 (2013) 476–481. doi:10.1016/j.apsusc.2013.03.119.
- [62] J. Yin, G. Zhu, B. Deng, Multi-walled carbon nanotubes (MWNTs)/polysulfone (PSU) mixed matrix hollow fiber membranes for enhanced water treatment, *J. Memb. Sci.* 437 (2013) 237–248. doi:10.1016/j.memsci.2013.03.021.
- [63] H. Li, N. Zhao, C. He, C. Shi, X. Du, J. Li, Thermogravimetric analysis and TEM characterization of the oxidation and defect sites of carbon nanotubes synthesized by CVD of methane, *Mater. Sci. Eng. A.* 473 (2008) 355–359. doi:10.1016/j.msea.2007.04.003.
- [64] M. Alsabet, M. Grden, G. Jerkiewicz, Electrochemical Growth of Surface Oxides on Nickel. Part 2: Formation of β -Ni(OH)₂ and NiO in Relation to the Polarization Potential, Polarization Time, and Temperature, *Electrocatalysis.* 5 (2014) 136–147. doi:10.1007/s12678-013-0172-z.
- [65] M. Alsabet, M. Grdeń, G. Jerkiewicz, Electrochemical Growth of Surface Oxides on Nickel. Part 3: Formation of β -NiOOH in Relation to the Polarization Potential, Polarization Time, and Temperature, *Electrocatalysis.*

6 (2014) 60–71. doi:10.1007/s12678-014-0214-1.

- [66] M. Alsabet, M. Grdeń, G. Jerkiewicz, Electrochemical Growth of Surface Oxides on Nickel. Part 1: Formation of α -Ni(OH)₂ in Relation to the Polarization Potential, Polarization Time, and Temperature, *Electrocatalysis*. (2011) 317–330. doi:10.1007/s12678-011-0067-9 *Electrochemical*.
- [67] F. Vitse, M. Cooper, G.G. Botte, On the use of ammonia electrolysis for hydrogen production, *J. Power Sources*. 142 (2005) 18–26. doi:10.1016/j.jpowsour.2004.09.043.
- [68] M.J. Russell, A.J. Hall, The hydrothermal source of energy and materials at the origin of life, *ACS Symp. Ser.* 1025 (2009) 45–62. doi:10.1021/bk-2009-1025.ch003.
- [69] H.G. A. MAUERER, UNTERSUCHUNGEN ZURANODISCHEN OXIDATION VONAMMONIAK AN PLATIN-ELEKTRODEN, *J. Electroanal. Chem. Interfacial Electrochem.* 25 (1969) 421–433.
- [70] H.M. French, M.J. Henderson, A.R. Hillman, E. Vieil, Ion and solvent transfer discrimination at a nickel hydroxide film exposed to LiOH by combined electrochemical quartz crystal microbalance (EQCM) and probe beam deflection (PBD) techniques, *J. Electroanal. Chem.* 500 (2001) 192–207. doi:10.1016/S0022-0728(00)00373-9.
- [71] M. Pourbaix, *Lectures on Electrochemical Corrosion*, Plenum Press, United States of America, 1973.
- [72] L.F. Huang, M.J. Hutchison, R.J. Santucci, J.R. Scully, J.M. Rondinelli, *Improved Electrochemical Phase Diagrams from Theory and Experiment:*

The Ni-Water System and Its Complex Compounds, *J. Phys. Chem. C*. 121
(2017) 9782–9789. doi:10.1021/acs.jpcc.7b02771.

APPENDIX

SOL-GEL PROCESS

The Sol-Gel process is the name applied when a solution, usually of a metal alkoxide, form polymers which crosslink together to form a **gel** (Figure A 1). At the transition, the solution or **sol** becomes a rigid porous mass through destabilization, precipitation, or supersaturation.

For a silica gel, with tetraethylorthosilicate (TEOS), is a one-phase solution that goes through an irreversible sol-gel transition to a rigid two-phase system of solid silica and solvent-filled pores. In this mechanism, the gel is formed as a combination of a continuous solid and fluid network of silanes, silanols, silicon alkoxide, water, and ethanol.

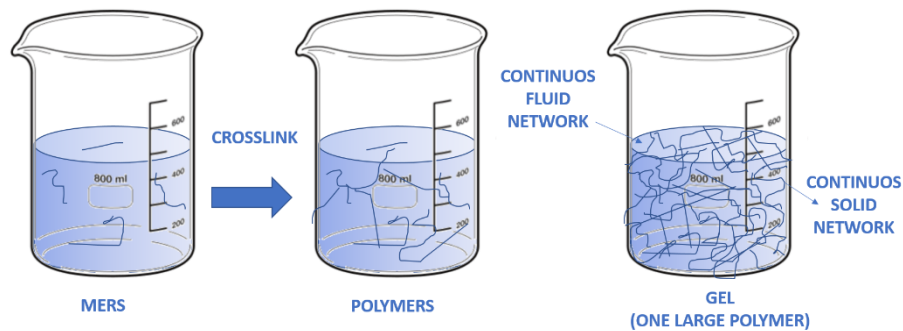


Figure A 1. Sol-Gel process

This process initiates spontaneously in the presence of water which hydrolyzes successive ethoxy groups on TEOS to create silanols and ethanol (Figure A 2). Since water and alkoxides are immiscible, it is necessary to use a common solvent to mix them into solution, commonly chosen to have the same carbon chain as the ligands of the alkoxide, in this case ethanol.

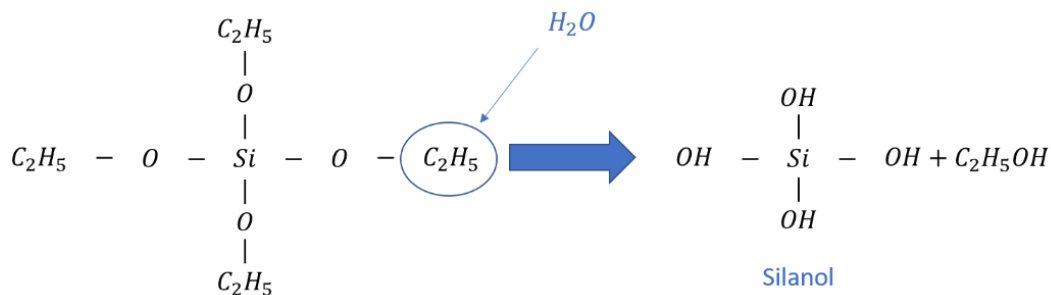


Figure A 2. Hydrolysis process of TEOS

Complete hydrolysis of TEOS would give silicic acid; however, this does not happen. Instead, a polymerization occurs (Figure A 3). As soon as a silanol group is formed it can react with an ethoxy group of TEOS or with another silanol to create siloxane bonds with a catalyst-controlled mechanism. In the presence of an acid

catalyst an electrophilic substitution occurs which difficult the subsequent hydrolysis while under base conditions subsequent hydrolysis becomes easier and carry out through nucleophilic substitution. As a result, linear polymers grow in an acid-catalyzed solution, and branched clusters grow in a base-catalyzed solution.

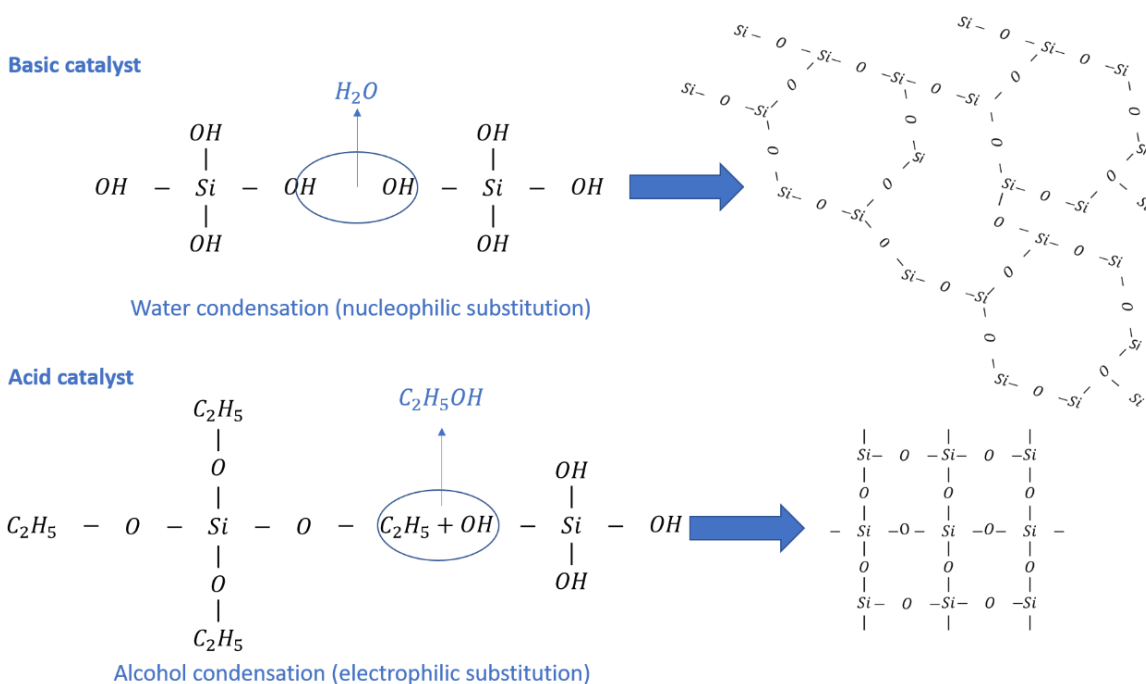


Figure A 3. Polymerization mechanism: Polymerization regenerates the water used in hydrolysis, perpetuating the reaction.

Once we succeed in going from step one, forming a solution, through step two, gelation, the third step is drying. In this process, the solvent phase is removed with ordinary evaporation to create xerogels, or with hypercritical evacuation to form aerogels (Figure A 4).

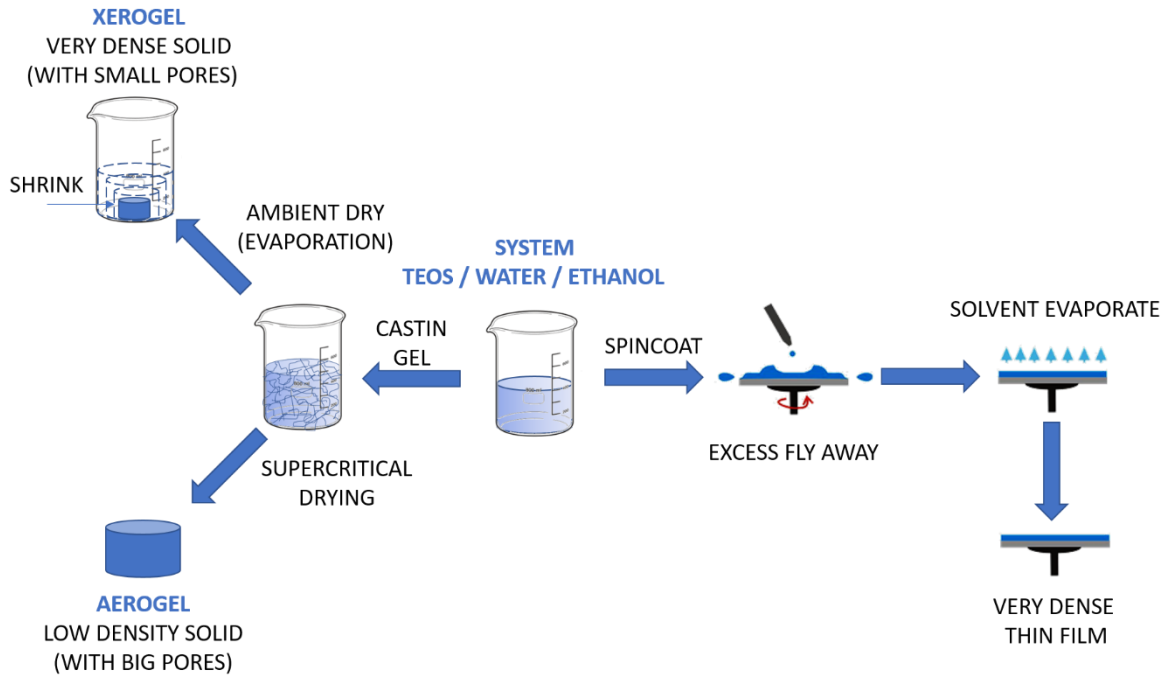


Figure A 4. Different cases of drying a gel

ANNEX

PUBLISHED PAPERS

- Determination of optical properties of a corn starch biofilm
- Synthesis and functionalization of carbon nanotubes and nanospheres as a support for the immobilization of an enzyme extract from the mushroom *Trametes Versicolor*

Determination of optical properties of a corn starch biofilm

J. Alejandro Menchaca-Rivera,¹ M. A. Gonzalez-Reyna ¹, Luz Ma. Avilés-Arellano,¹
 Rodrigo Fernández-Loyola,¹ Eduardo Morales-Sánchez,² J. Francisco Pérez Robles ¹

¹Centro de Investigación y de Estudios Avanzados del IPN, Unidad Querétaro, Libramiento Norponiente No. 2000, Fraccionamiento Real de Juriquilla, C.P. 76230, Querétaro, Querétaro, México

²Centro de Investigación en Ciencia Aplicada y Tecnología Avanzada-IPN, Unidad Querétaro, Cerro Blanco No. 141, 76090, Col. Colinas del Cimatario, C.P. 76090, Querétaro, Querétaro, México

Correspondence to: J. F. Pérez Robles (E-mail: jfperez@cinvestav.mx)

ABSTRACT: In this work, the optical properties of a corn starch-based film were correlated with its structural properties. Scanning electron microscopy was performed to determine if incorporation of starch into the matrix gives a homogenous and smooth surface. X-ray diffraction was performed to identify the relative degree of crystallinity. The optical properties of the film in the range 300 to 2500 nm were studied, showing diffuse total transmissivity and total absorption coefficients comparable with that of low-density polyethylene films. The process used in this research is carried out in an aqueous solvent, without using any toxic raw material, and prepared by casting. The process allows for the use of different additives. This processing of the starch film represents a great advantage also because it takes a maximum of 10 h, four times less than other processes, and no special equipment is needed. © 2018 Wiley Periodicals, Inc. *J. Appl. Polym. Sci.* **2018**, *135*, 47111.

KEYWORDS: biopolymers and renewable polymers; films; optical properties; synthesis and processing techniques; thermoplastics

Received 4 April 2018; accepted 7 August 2018

DOI: 10.1002/app.47111

INTRODUCTION

Plastics have been widely used throughout the world for a long time. Normally they are designed and manufactured to resist environmental degradation; besides, they are low in cost in terms of processing and energy.¹ Plastic materials have a wide range of applications due to their desirable properties, such as flexibility, light weight, optical transparency, low cost, ease of manufacture, and diverse mechanical properties.²

However, over time, plastics have come to represent a serious pollution problem. Therefore, environmental concerns have promoted research and development on new materials from renewable sources that are biodegradable or compostable at the end of their lifecycle.^{1,3–7} In recent years, the importance and applications of biobased plastics have grown. In 2014, the global production capacity of biobased plastics was 1.7 million of tons, where 10% was based on biodegradable starch blends.⁸ Bioplastics are used in an increasing number of applications, from packaging to electronics, from automotive to agriculture, and a number of other segments.⁸

In agriculture and food industries, plastic is successful because it is light in weight, is a barrier against microorganisms, and provides protection against the environment, which keeps plants and food fresh and free of contamination.^{5,6,9,10} In protected horticulture, plastic materials are used as radiation filters in order to modify crop

temperature and the growth of plants. Therefore, the optical properties, such as reflectivity (ρ), transmissivity (τ), and absorption (α) of solar radiation, are important factors that have to be taken into account when designing plastics for that application.^{3,11–13} In the present work, research was conducted on synthesizing a transparent plastic based on starch without using special equipment. It is necessary to remark that the total processing time was 10 h, shorter than that for other processes used to produce plastics with the same purpose, which are carried out over more than 48 h and need both some additives and a vacuum to process them.^{14–17}

Maran *et al.*¹⁴ obtained a homogenous and clear film of starch by the casting method, using degassing with a vacuum and drying for 48 h. Alves *et al.*¹⁵ prepared a translucent starch film by casting, employing a filmogenic solution, and drying in a ventilated oven for about 20 h. Thermoplastic starch was processed by Seligra *et al.*¹⁶ at 50 °C for 24 h. Guimaraes *et al.*¹⁷ obtained a film from a solution of starch with 3% starch and drying for 10 days.

Starch-based film can be processed by different techniques (casting, injection, or blowing), and different processes can provide different properties.¹⁸ The properties are dependent on the presence of flaws and the degree of crystallinity, and crystalline structures found in thermoplastic starch polymers are influenced by the composition and processing.^{19,20} For instance, high-amylose materials

generally result in products with higher strength and stiffness than high-amylopectin materials, due to the linear amylose chains entangling effectively and forming strong physical crosslinks, resulting in strong and coherent materials.²¹ On the other hand, if the starch is incompletely gelatinized, remnants of the granules can lead to fracture zones in the samples. In addition, ghosts of the initial starch granules can survive processing, and these too produce inhomogeneities in the structure that can limit the ductility and optical properties.²⁰ In terms of optical properties, a rough surface reflects and transmits light in random directions, and the refractive index of an amorphous phase is less than that of a crystalline phase. The combination of the two previous effects makes the polymeric material less transparent and therefore more or less opaque.¹⁹

For the above reasons, in the present work, we performed a morphological and structural characterization of the obtained materials using scanning electron microscopy (SEM) and X-ray diffraction (XRD). In addition, the optical properties that are the main focus of this publication were determined, within which the spectral coefficients and parameters related to the transmission of photosynthetically active radiation were calculated using a spectrophotometer equipped with an integrating sphere and compared with the values of low-density polyethylene, which is the most-used synthetic plastic.

EXPERIMENTAL

Materials

Normal corn starch (Sigma-Aldrich, St. Louis, MO) and glycerol (Meyer, Mexico City, Mexico) were used as received, containing 73% amylopectin and 27% amylose according to the provider, so we can assume that the film will present a low crystallinity, in deionized water ($>18 \mu\Omega \text{ cm}$). Commercial transparent low-density polyethylene (LDPE) from the petrochemical company PEMEX (Mexican Oil Industry) was used for comparison.

Preparation of Cornstarch-Based Films

Native starch granules consist essentially of two types of polymers of α -D-glucose: an essentially linear molecule, amylose, and a highly branched molecule, amylopectin. The amylose/amylopectin ratio varies for each starch source. To generate thermoplastic starch polymers, the complex semicrystalline structure needs to be destroyed to produce an amorphous material. This

process, called gelatinization, is achieved by heating the starch in the presence of water and glycerol as plasticizer, which have two important roles: aiding in gelation and decreasing the processing temperatures to avoid starch degradation.^{15,20–22}

Native starch was dissolved in deionized water, using a starch/water ratio of 1:10 at $90 \pm 5 \text{ }^\circ\text{C}$ on a hot plate and stirring the mixture at 560 rpm until all starch clusters were dissolved. Then glycerol (30% w/w relative to starch) was added slowly to form a homogenous solution. The corn starch-based (CSB) film solution was cooled slightly and was used to prepare the films by casting on an acrylic plate as substrate and dried at $70 \text{ }^\circ\text{C}$ in a conventional oven for 8 h.

Characterization of the Films

The X-ray diffraction study was performed using a Rigaku DMAX 2100 diffractometer (Tokyo, Japan). SEM analysis was performed using a Philips XL30 ESEM (Amsterdam, Netherlands). An ultraviolet–visible–near infrared (UV–vis–NIR) CARY 5000 spectrophotometer (Agilent, Santa Clara, CA), with an integrating sphere accessory (DRA 2500), was used to determine the spectral coefficients (ρ , τ , and α). The sphere has a diameter of 110 mm, with an internal coating of polytetrafluoroethylene (PTFE) of 4 mm thickness, and a measuring range of 200 to 2500 nm; the sample ports have a measurement area of 3.14 cm^2 . Supplementary infrared spectroscopy was used to analyze the functional groups in both samples using a Fourier transform infrared (FTIR) spectrophotometer (Spectrum GX, PerkinElmer, Waltham, MA). The spectra were obtained in the range 4000 to 650 cm^{-1} using the technique of attenuated total reflectance (ATR), from which the chemical groups of both films were determined.

RESULTS AND DISCUSSION

All analyses were performed using two films: a corn starch-based film with thickness of $74 \mu\text{m}$ and an LDPE with $53 \mu\text{m}$. As we presented, many mechanical and optical properties are dependent on the presence of flaws in the materials. Figure 1 shows the SEM analysis of both films. Here both polymers present a low, rough homogenous surface, which promotes a good optical dispersion of light. Even more, the CSB film [Figure 1(a)] shows no cracks or internal voids or granule remnants. This means the starch was completely gelatinized and destroyed, promoting the

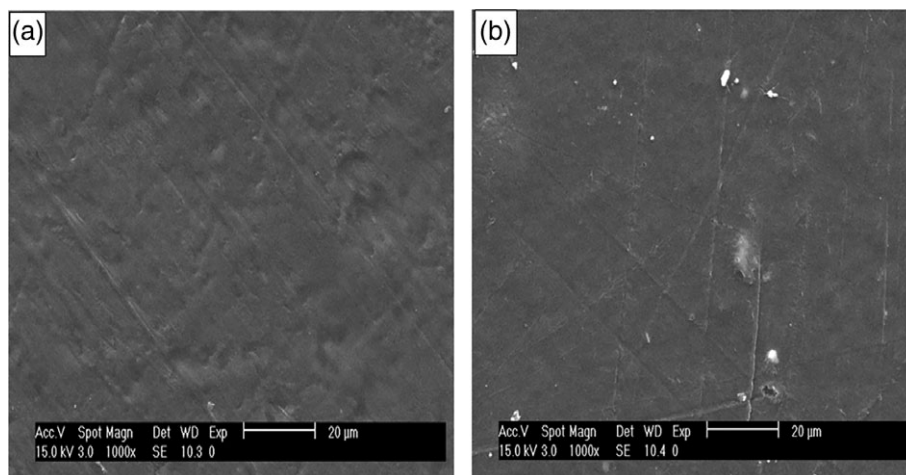


Figure 1. Surface of (a) CSB and (b) LDPE. Micrographs were obtained by coating the sample with a thin layer of gold to improve conductivity.

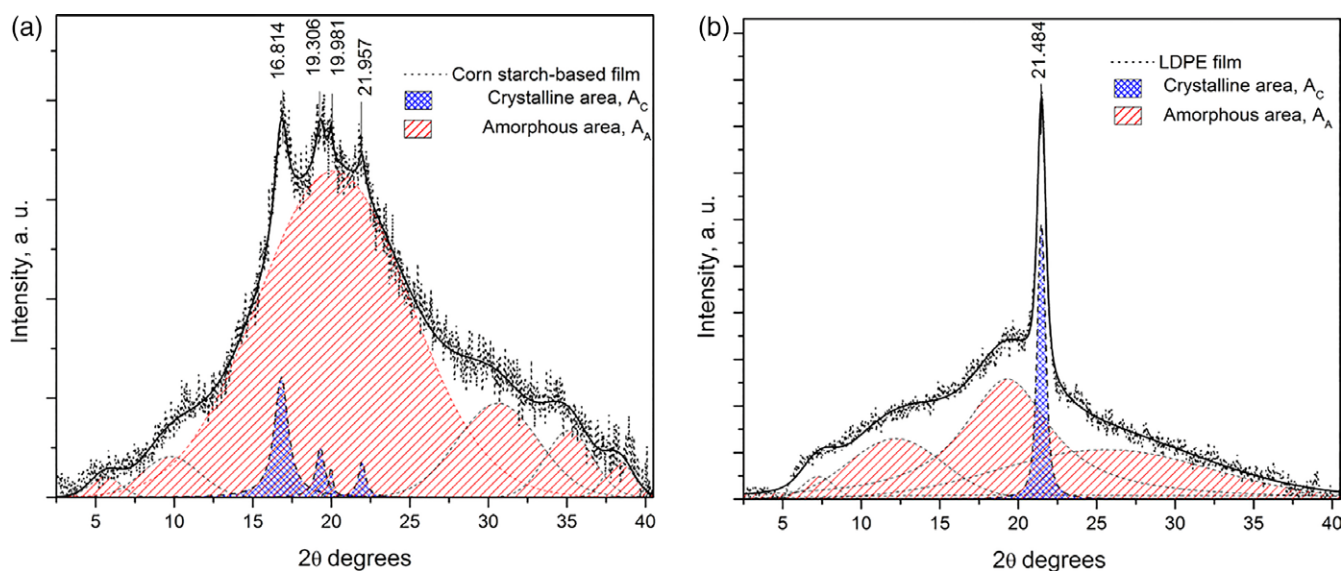


Figure 2. Original and deconvoluted X-ray diffractograms of (a) CSB film and (b) LDPE film. [Color figure can be viewed at wileyonlinelibrary.com]

formation of a homogenized and transparent film and suggesting a cohesive matrix, as has been reported by Fakhouri *et al.*¹⁸

X-Ray Diffraction

The X-ray diffraction results are presented in Figure 2, where the dotted curve is the original diffractogram and the solid line is the fitted curve obtained from a deconvolution. Figure 2(a) shows the X-ray spectra of the CSB film. The planes indexed at 16.814°, 19.306°, 19.981°, and 21.957° are characteristic of type “A” of native corn starch.^{23,24} The plane at 19.306° may be associated with a recrystallization of the CSB film due to the thermal processing and the presence of glycerol. Figure 2(b) shows the diffractogram of LDPE film, which, in contrast to starch biofilm, has only one diffraction plane at 21.484°.^{25–29}

Values of relative degree of crystallinity, C , calculated with eq. (1), and interplanar distance, d , calculated with Bragg’s law, are shown in Table I, where A_C is the total area of the diffracted planes (crystalline region), and A_A is the area of amorphous material in the diffractogram.^{26,28,30,31} CSB showed a lower crystallinity than LDPE, and therefore a lower refractive index; consequently, CSB should be more transparent, even taking account the difference in thickness. On the other hand, the modulus and strength are directly proportional to the degree of crystallinity. To solve this problem, different additives could be used to

improve the material properties, or a different type of starch with bigger amylose/amylopectin ratio could be used.²¹

$$C (\%) = \frac{A_C}{A_C + A_A} \times 100 \quad (1)$$

Spectrophotometry

In the range of solar (300 to 2500 nm), near-infrared (700 to 2500 nm), and photosynthetically active radiation (PAR, 400 to 700 nm), the spectral coefficients (ρ , τ , and α) were calculated using the UV–vis–NIR spectrophotometer. Figure 3 shows the UV–vis–NIR spectrum. Both films present very similar values from 200 to 800 nm, but in the range 800 to 2500 nm, notable changes are due to the cyclic structure of the starch in comparison to the linear structure of the LDPE and its contributions by CH groups.^{32–35} In the range 1400 to 1600 nm, the contributions of CH₃ and OH groups are apparent, while in 1650 to 1850 nm the contributions of CH and CH₃ are observed. The signals at about 1950 nm are attributed to the O–H vibration of water. At 2100 nm, the contribution of the O–H from the alcohol on C6 of the ring of pyranose is observed. Finally, in the range 2300 to 2500 nm, the vibrations of CH₃ and CH₂ are observed.^{32–35}

Diffuse transmittance spectra are shown in Figure 4, and they were calculated by subtracting the normal transmission spectra from the total transmission spectra for both films in the range 200 to 2500 nm. Measurements of transmission spectra at normal incidence were obtained using the UV–vis–NIR spectrophotometer, and total transmission spectra were obtained using the integrating sphere accessory. In this figure, it is shown that the diffuse transmittance of the CSB film is greater than that of LDPE film.

Irradiation values $E_\lambda(\lambda)$ were taken from ASTM G173-03³⁶; the spectral coefficients can be calculated using the obtained spectra. The average material coefficient R_s evaluated in the range of solar radiation of interest can be calculated as shown in eq. (2)^{3,11–13}:

Table I. Relative Crystallinity of CSB and LDPE Films

| Material | 2θ | d (Å) | C (%) |
|----------|--------|---------|---------|
| CSB | 16.814 | 5.269 | 5.56 |
| | 19.306 | 4.594 | |
| | 19.981 | 4.44 | |
| | 21.957 | 4.045 | |
| LDPE | 21.484 | 4.133 | 8.21 |

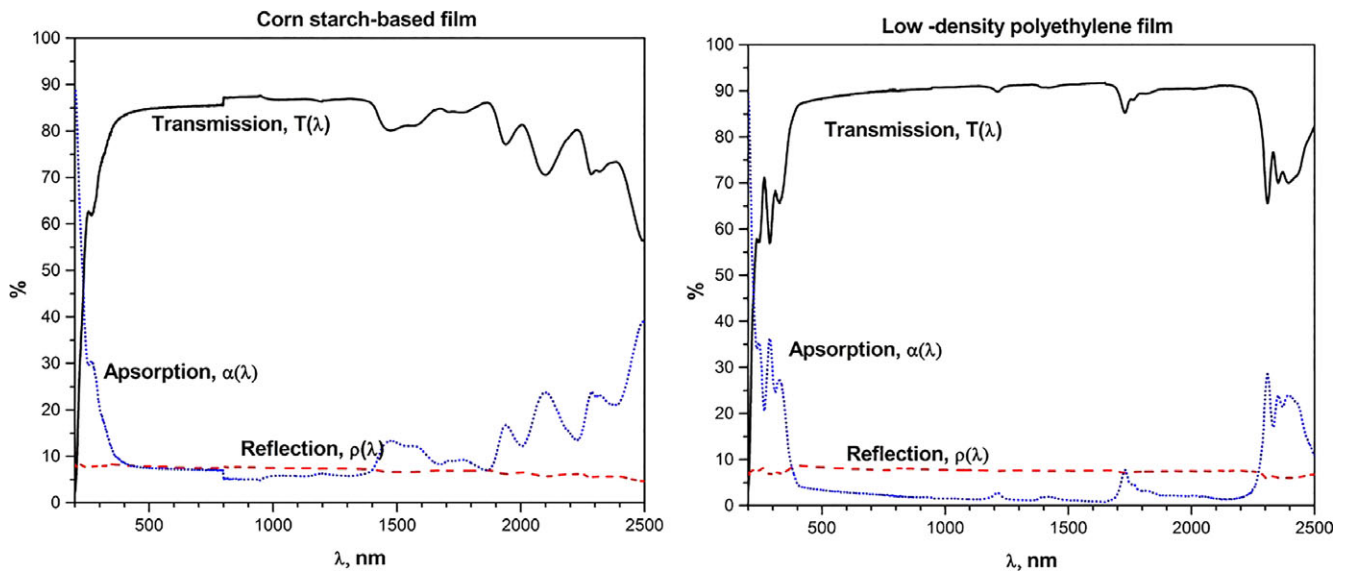


Figure 3. Total transmission, total reflection, and total absorption spectra of (a) CSB film and (b) LDPE films measured with an integrating sphere. [Color figure can be viewed at wileyonlinelibrary.com]

$$R_S = \frac{\int_{\lambda_1}^{\lambda_2} R(\lambda) E_\lambda(\lambda) d\lambda}{\int_{\lambda_1}^{\lambda_2} E_\lambda(\lambda) d\lambda} \quad (2)$$

where R_s represents the transmissivity (τ), reflectivity (ρ), and absorption (α) coefficients, and $R(\lambda)$ represents the measured spectral values (see Figures 3 and 4) evaluated over the range of wavelengths considered.

Once the coefficients τ and ρ are calculated, the average solar absorption can be calculated using the Kirchhoff ratio^{3,11–13}:

$$\tau + \rho + \alpha = 1 \quad (3)$$

Based on the above studies, the spectral coefficients are presented in Table II. The coefficients were evaluated in the solar, PAR, and NIR ranges. Additionally, the spectral coefficients for diffuse transmission are presented in the same table.

From Table II, the total absorption and diffuse transmissivity coefficients in CSB are greater than in LDPE, showing an increase of 162.2% and 357% in the solar range, 136.5% and 312.6% in PAR, and 256.9% and 453.4% in NIR, respectively. This means a greater amount of scattered radiation, decreasing the risk of burn injuries on crops, as well as reducing the shade of solid materials in their path. Certain basic information about the spectral response of photosynthesis is required for a rational discussion of the relative merits of the various definitions of photosynthetically

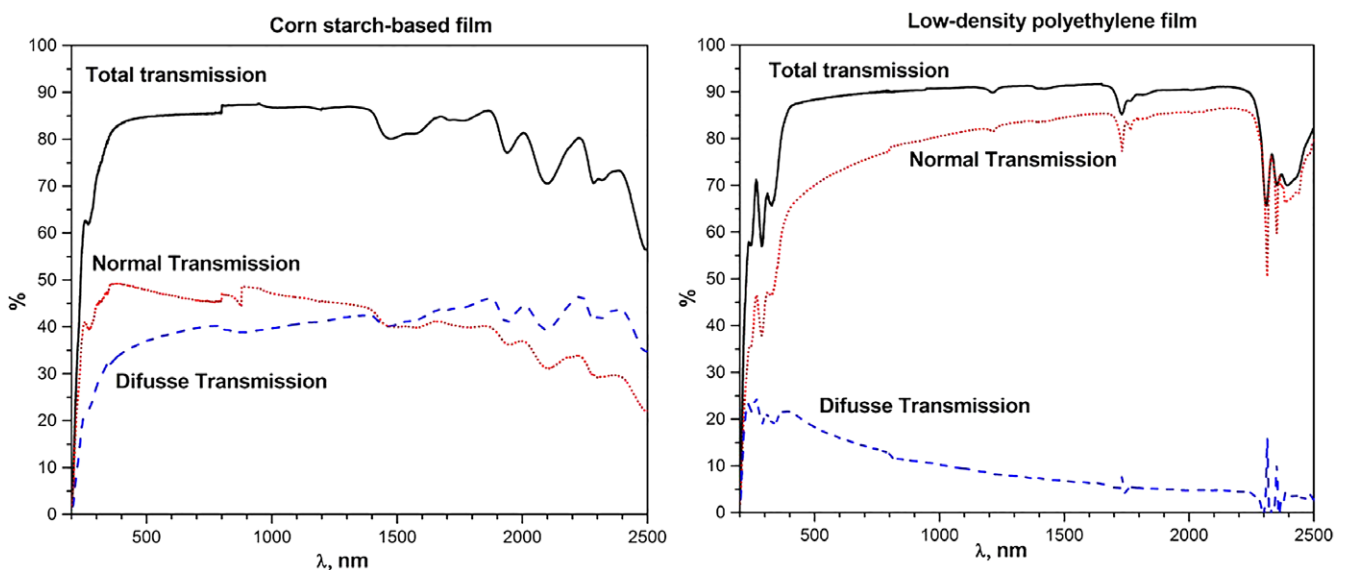


Figure 4. Spectrum of normal transmission and diffuse and total transmission of (a) CSB film and (b) LDPE film. [Color figure can be viewed at wileyonlinelibrary.com]

Table II. Spectral Coefficients of Transmissivity, Reflectivity, and Absorption

| Range: | Solar | | PAR | | NIR | |
|-----------------------------|-------|-------|-------|-------|-------|-------|
| Film: | CSB | LDPE | CSB | LDPE | CSB | LDPE |
| τ_{total} (%) | 89.7 | 90.13 | 88.98 | 89.23 | 90.73 | 91.32 |
| τ_{diffuse} (%) | 50.84 | 14.24 | 51.39 | 16.44 | 50.15 | 11.06 |
| ρ_{total} (%) | 7.51 | 8.15 | 7.58 | 8.25 | 7.42 | 7.96 |
| α_{total} (%) | 2.79 | 1.72 | 3.44 | 2.52 | 1.85 | 0.72 |

active radiation. This could be in the form of an action spectrum, that is, the rate at which carbon dioxide is taken up (or oxygen evolved), divided by the rate at which energy is received by the leaf, and is denoted by A_{λ} .³⁷

The effective photosynthetic action transmission η represents the effective proportion of outside radiant energy transmitted by the film and active for photosynthesis. It is obtained by eq. (4)^{11,12} with the action spectrum parameter, A_{λ} , characteristic of the photosynthetic response of an average plant to PAR energy, reported by McCree,³⁷ where $\tau(\lambda)$ is taken from Figure 4:

$$\eta = \frac{\int_{400}^{700} E_{\lambda}(\lambda)\tau(\lambda)A_{\lambda}(\lambda)d\lambda}{\int_{400}^{700} E_{\lambda}(\lambda)A_{\lambda}(\lambda)d\lambda} \quad (4)$$

The effective quantum transmission, E [eq. (5)], with quantum yield response Y_{λ} ,³⁷ represents the relative quantity of photon flux that can be absorbed by the leaf of the plant after transmission through the film^{11,12}:

$$E = \frac{\int_{400}^{700} E_{\lambda}(\lambda)\tau(\lambda)Y_{\lambda}(\lambda)d\lambda}{\int_{400}^{700} E_{\lambda}(\lambda)Y_{\lambda}(\lambda)d\lambda} \quad (5)$$

The light parameter ζ can be determined by eq. (6) and is a ratio of photon fluence rates of a 10 nm band centered on 660 nm and 730 nm; this is related to the morphogenetic response of the plant^{11,12}:

$$\zeta = \frac{E_{\lambda}(660)\tau(660)}{E_{\lambda}(730)\tau(730)} \quad (6)$$

Parameters related to the PAR range and the ratio ζ are summarized in Table III, where small differences were found between the films. Furthermore, values of η and E are very close to the values analyzed in transmission in the PAR wavelengths, meaning CSB is a good optical prospect as cover material due its transparency, as it will let the crop receive the PAR radiation it needs to grow.

FTIR-ATR

The spectra obtained for the CSB and LDPE films are shown in Figure 5. Due to the complexity of the molecular structure of the CSB film, the spectrum presents a variety of bands within the range 3450 to 3217 cm^{-1} [Figure 5(a)]. Those bands are

attributed to the stretching vibrational modes associated with OH group bonds that make up the structure of starch and glycerol.^{4,27} The bands at 2935 to 2889 cm^{-1} are characteristic of stretching CH bonds. It has been reported²⁷ that a decrease in the intensity of these vibrational bands can be attributed to the breakdown that is due to the thermal processing of biodegradable starch materials, natural fibers, and glycerol. The band at 1643 to 1630 cm^{-1} is associated with bands of OH bonds of water located in starch, and specifically the band at 1640 cm^{-1} is due to bound water, probably in the carbonyl group of starch.^{24,27,38}

In the range 1500 to 1300 cm^{-1} , it is not possible to determine the vibrational modes since these are attributed to the deformation of Z-C-H bonds, where Z may be O or C, although some contribution of COH and OH stretching vibrational modes is detected. In the absorption band at 1461 cm^{-1} , contributions of bonds of O-C-H and C-H appear, in the absorption band at 1419 cm^{-1} vibrations of bonds of O-C-H appear, while at 1340 cm^{-1} deformation of bonds of C-H₂ and O-H appears, and in the absorption band at 1292 cm^{-1} appear vibrational modes of O-C-H and C-C-H.^{27,39-41}

On the other hand, in the range 1300 to 900 cm^{-1} , contributions arise due to the stretching modes of C-O and C-C bonds. According to Vasko *et al.*,^{39,40} the absorption bands at 1153 cm^{-1} , 1076 cm^{-1} , and 1049 cm^{-1} are due to C-O bonds, followed by contributions of C-C and C-O-H bonds. The bands at 1019 cm^{-1} and 990 cm^{-1} are due to C-C bonds with a contribution of about 50%, followed by the contributions of O-C-H, C-C-H, and C-C-O bonds. The bands at 862 cm^{-1} and 846 cm^{-1} are contributions of the C-C, C-C-H, and C-O bonds.^{27,39,40}

Figure 5(b) shows the FTIR spectrum of LDPE film. The bands at 2916 and 2848 cm^{-1} belong to the stretching modes of CH₂ bonds. The band at 1471 cm^{-1} belongs to bending vibrations

Table III. Comparative Values of the Plant Related to the Parameters Yield Efficiency, Effective Quantum Transmission, and Ratio of Red to Far Red Irradiance

| Film | η | E | ζ |
|-------------|--------|-------|---------|
| CSB | 89.41 | 89.04 | 1.21 |
| LDPE | 90.14 | 89.32 | 1.21 |

Values in %.

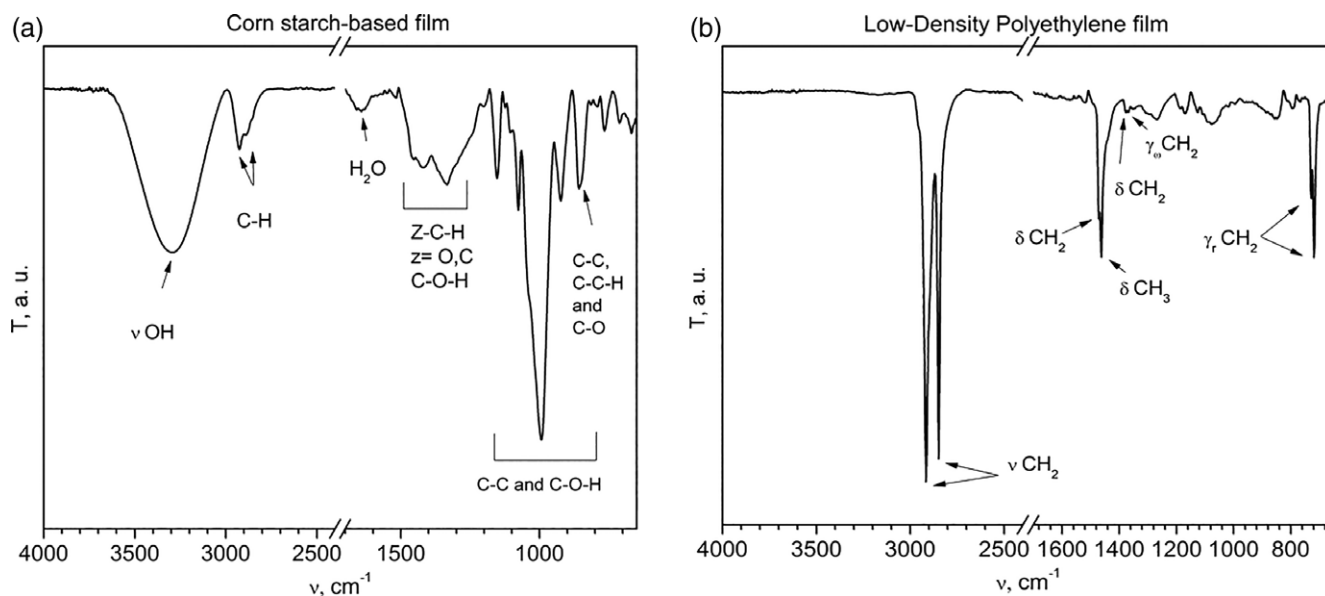


Figure 5. FTIR spectra obtained by the ATR technique: (a) CSB film and (b) LDPE film (ν = stretching deformation, δ = scissoring deformation, γ_w = wagging deformation, γ_r = rocking deformation).

of CH_2 bonds, while the bands present at 1462 and 1376 cm^{-1} are due to bending vibrations of CH_3 bonds. The band at 1369 cm^{-1} belongs to wagging vibrations of CH_2 bonds, while the bands at 729 and 719 cm^{-1} belong to rocking vibrations of CH_2 bonds.^{4,9,42}

CONCLUSIONS

In this work, a simple optical characterization methodology is presented that allows estimation of optical behavior and spectral coefficients of a corn-based starch film. By means of SEM analysis, it was ensured that granules of native starch were destroyed, promoting in this way the formation of a film with a homogenized solution, which is helpful in its optical properties. XRD shows that CSB has a low relative crystallinity of 5.56%, explaining its high transparency. The results confirm that a corn starch-based film represents a low-cost, ecological, and sustainable alternative to low-density polyethylene as covers for agriculture due to its high transparency and scattering in the visible range. It can greatly reduce the risk of plants being burned by direct exposure to radiation owing to its high values of diffused transmission coefficients (50.84% for the solar range, 51.39% for the PAR range, and 50.15% for the NIR range). Even more, the photosynthesis process can be enhanced because the filtered light can reach more parts of the plant.

Additionally, the corn starch process is appropriate for developing ecofriendly and low-cost films due to the capacity to form cohesive films, and their use in agriculture represents a low-cost alternative. The obtained results give the opportunity to use hybrid composites to obtain a synergy between both materials for applications in agriculture, with better properties of biodegradability, less deformation, and more scattering of light, and it is an approach toward an ecologically sound idea of partially substituting for polymers from nonrenewable sources.

ACKNOWLEDGMENTS

The authors gratefully acknowledge CONACYT-Mexico for the scholarship provided for doctoral studies. We would also like to show our gratitude to Dr. Gerardo Torres Delgado and Q. A. Cynthia Zúñiga Romero, who provided technical assistance, and to PEMEX Petrochemistry for facilitating the low-density polyethylene.


REFERENCES

1. Ali, R. R.; Rahman, W. A. W. A.; Kasmani, R. M.; Ibrahim, N. *Int. J. Chem. Mol. Nucl. Mater. Metal. Eng.* **2012**, *6*, 531.
2. Nguyen Vu, H. P.; Lumdubwong, N. *Carbohydr. Polym.* **2016**, *154*, 112.
3. Vox, G.; Schettini, E. *Polym. Test.* **2007**, *26*, 639.
4. Pushpadass, H. A. A.; Bhandari, P.; Hanna, M. A. A. *Carbohydr. Polym.* **2010**, *82*, 1082.
5. Ferreira, A. R. V.; Alves, V. D.; Coelho, I. M. *Membranes (Basel)* **2016**, *6*, 1.
6. Romani, V. P.; Prentice-Hernández, C.; Martins, V. G. *Ind. Crops Prod.* **2017**, *97*, 268.
7. Kaisangsri, N.; Kerdchoechuen, O.; Laohakunjit, N. *Ind. Crops Prod.* **2012**, *37*, 542.
8. European Bioplastics; Institute for Bioplastics and Biocomposites **2017**, 1. Available at http://docs.european-bioplastics.org/publications/EUBP_Facts_and_figures.pdf (accessed December 29, 2017).
9. Raj, B.; Sankar, U. K.; Siddaramaiah *Adv. Polym. Technol.* **2004**, *23*, 32.
10. de Moraes Crizel, T.; Haas Costa, T. M.; de Oliveira Rios, A.; Hickmann Flôres, S. *Ind. Crops Prod.* **2016**, *87*, 218.

11. Papadakis, G.; Briassoulis, D.; Scarascia Mugnozza, G.; Vox, G.; Feuilloley, P.; Stoffers, J. A. *J. Agric. Eng. Res.* **2000**, *77*, 7.
12. Kittas, C.; Baille, A. *J. Agric. Eng. Res.* **1998**, *71*, 193.
13. Picuno, P.; Sica, C.; Laviano, R.; Dimitrijević, A.; Scarascia-Mugnozza, G. *Polym. Degrad. Stab.* **2012**, *97*, 1654.
14. Maran, J. P.; Sivakumar, V.; Sridhar, R.; Thirugnanasambandham, K. *Carbohydr. Polym.* **2013**, *92*, 1335.
15. Alves, V. D.; Mali, S.; Beléia, A.; Grossmann, M. V. E. *J. Food Eng.* **2007**, *78*, 941.
16. Seligra, P. G.; Medina Jaramillo, C.; Famá, L.; Goyanes, S. *Carbohydr. Polym.* **2016**, *138*, 66.
17. Guimarães, M.; Botaro, V. R.; Novack, K. M.; Teixeira, F. G.; Tonoli, G. H. D. *Ind. Crops Prod.* **2015**, *70*, 72.
18. Fakhouri, F. M.; Costa, D.; Yamashita, F.; Martelli, S. M.; Jesus, R. C.; Alganer, K.; Collares-Queiroz, F. P.; Innocentini-Mei, L. H. *Carbohydr. Polym.* **2013**, *95*, 681.
19. Roos, A. *Appl. Opt.* **1994**, *33*, 7908.
20. Chaléat, C.; Halley, P. J.; Truss, R. W. In *Starch Polymers: From Genetic Engineering to Green Applications*; Halley, P. J., Averous, L. R., Eds.; Elsevier: Amsterdam, Netherlands, **2014**; Chapter 7, p 187.
21. Jenkins, P. J.; Donald, A. M. *Int. J. Biol. Macromol.* **1995**, *17*, 315.
22. Kim, H. Y.; Jane, J.; Lamsal, B. *Ind. Crops Prod.* **2017**, *95*, 175.
23. Colussi, R.; Pinto, V. Z.; El Halal, S. L. M.; Vanier, N. L.; Villanova, F. A.; Marques E Silva, R.; Da Rosa Zavareze, E.; Dias, A. R. G. *Carbohydr. Polym.* **2014**, *103*, 405.
24. Pushpadass, H. A.; Marx, D. B.; Wehling, R. L.; Hanna, M. A. *Cereal Chem.* **2009**, *86*, 44.
25. BeMiller, J. N. *Starch: Chemistry and Technology*, 3rd ed.; BeMiller, J., Whistler, R., Eds.; Elsevier: Cambridge, **2009**.
26. Frost, K.; Kaminski, D.; Kirwan, G.; Lascaris, E.; Shanks, R. *Carbohydr. Polym.* **2009**, *78*, 543.
27. Galicia-García, T.; Martínez-Bustos, F.; Jiménez-Arevalo, O.; Martínez, A. B.; Ibarra-Gómez, R.; Gaytán-Martínez, M.; Mendoza-Duarte, M. *Carbohydr. Polym.* **2011**, *83*, 354.
28. Shujun, W.; Hongyan, L.; Wenyuan, G.; Haixia, C.; Jiugao, Y.; Peigen, X. *Food Chem.* **2006**, *99*, 30.
29. Tang, M. C.; Copeland, L. *Carbohydr. Polym.* **2007**, *67*, 80.
30. Buléon, A.; Colonna, P.; Planchot, V.; Ball, S. *Int. J. Biol. Macromol.* **1998**, *23*, 85.
31. Ramírez-Wong, D. G.; Ramírez-Cardona, M.; Sánchez-Leija, R. J.; Rugerio, A.; Mauricio-Sánchez, R. A.; Hernández-Landaverde, M. A.; Carranza, A.; Pojman, J. A.; Garay-Tapia, A. M.; Prokhorov, E.; Mota-Morales, J. D.; Luna-Bárceñas, G. *Green Chem.* **2016**, *18*, 4303.
32. Bernard, L. In *Infrared and Raman Spectroscopy of Biological Molecules*; Theophanides, T. M., Ed.; Springer Netherlands: Dordrecht, **1979**.
33. Gulmine, J. V.; Janissek, P. R.; Heise, H. M.; Akcelrud, L. *Polym. Test.* **2002**, *21*, 557.
34. Mizushima, M.; Kawamura, T.; Takahashi, K.; Nitta, K. *Polym. J.* **2012**, *44*, 162.
35. Socrates, G. *Infrared and Raman Characteristic Group Frequencies*, 3rd ed.; Wiley: New York, **2004**.
36. ASTM G173-03; ASTM: West Conshohocken, PA, **2013**.
37. McCree, K. *J. Agric. Meteorol.* **1971**, *9*, 191.
38. Zullo, R.; Iannace, S. *Carbohydr. Polym.* **2009**, *77*, 376.
39. Vasko, P. D.; Blackwell, J.; Koenig, J. L. *Carbohydr. Res.* **1971**, *19*, 297.
40. Vasko, P. D.; Blackwell, J.; Koenig, J. L. *Carbohydr. Res.* **1972**, *23*, 407.
41. Basri, S. N.; Zainuddin, N.; Hashim, K.; Yusof, N. A. *Carbohydr. Polym.* **2016**, *138*, 34.
42. Krimm, S.; Liang, C. Y.; Sutherland, G. B. B. M. *J. Chem. Phys.* **1956**, *25*, 549.



Synthesis and functionalization of carbon nanotubes and nanospheres as a support for the immobilization of an enzyme extract from the mushroom *Trametes versicolor*

Mariana Romero-Arcos¹, Juan Francisco Pérez-Robles^{2,*} , Ma. Guadalupe Garnica-Romo³, Maria Selene Luna-Martinez⁴, and M. A. Gonzalez-Reyna⁴

¹ Cinvestav Libramiento Norponiente, #2000, Fracc. Real de Juriquilla, C.P. 76230 Santiago de Querétaro, Qro, Mexico

² Laboratorio de Materiales Nanoestructurados y Caracterización Electroquímica, Cinvestav Libramiento Norponiente, #2000, Fracc. Real de Juriquilla, C.P. 76230 Santiago de Querétaro, Qro, Mexico

³ Facultad de Ingeniería Civil, Universidad Michoacana de San Nicolás de Hidalgo, Santiago Tapia 403, col. Centro, C.P. 5800 Morelia, Mexico

⁴ Programa de Doctorado en Nanociencias y Nanotecnología, Cinvestav Zacatenco, Mexico, Mexico

Received: 1 January 2019

Accepted: 27 May 2019

© Springer Science+Business Media, LLC, part of Springer Nature 2019

ABSTRACT

In this work, an enzyme extract immobilization over carbon nanomaterials is presented; that is, carbon nanospheres (CNSs), and multi-walled carbon nanotubes (CNTs), using covalent bonds with glutaraldehyde as a crosslinking compound. Carbon nanostructures were obtained by chemical vapor deposition using an iron–cobalt powder alloy prepared by the sol–gel process and using silica powder as support. Acetylene gas was used as carbon carrier to prepare both the CNTs and CNSs. Both nanostructures were oxidized with an acid treatment in order to add functional groups to the surface and subsequently immobilize the enzymes. Carbon nanostructures were characterized using scanning electron microscopy, infrared spectroscopy and Raman spectroscopy to confirm oxidation, immobilization and structural properties. Electrochemical impedance spectroscopy revealed that carbon nanostructures improve the electron transfer of the electrode. Finally, the cyclic voltammetry provided information about the redox process before and after immobilization. Even more, the catalytic activity of the enzymes extract was evaluated showing that CNSs are the best support.

Address correspondence to E-mail: jfperez@cinvestav.mx

<https://doi.org/10.1007/s10853-019-03722-2>

Published online: 03 June 2019

Introduction

In recent years, it has been recognized the potential applications of carbon nanomaterials, such as carbon nanotubes (CNTs) and carbon nanospheres (CNSs) and their oxidized derivatives due to their possibility to develop materials for a wide variety of applications such as capacitors, fuel cells, biosensors and biocatalysts [1, 2]. Among the properties that can be considered for the application of those materials are the high surface area, high adsorption capacity of some chemical species and high conductivity that facilitate the transfer of electrons between the electroactivated species and the electrode surface [3–6]. As it is well known, the CNTs are composed of concentric and closed graphene sheets, rolled each one around the other giving structures of different diameters, typically 2 to 30 nm. The CNTs increase the electrocatalytic activity of some chemical compounds, due to the above-mentioned properties and to the presence of active sites, like the edge plane located at both ends and defects along the surface of them, where the chemical species can be attached. In addition to that, they provide a high surface-to-volume ratio and faster electron transfer kinetics owing to their curvature [7, 8]. On the other hand, CNSs consider the advantages of carbon materials with spherical colloids, which give them several unique characteristics such as regular geometry, tunable porosity and controllable particle size distribution. Those innovative materials present a high value for catalysis, adsorption, purification of water and air, storage and energy conversion [9, 10].

The immobilization of biomolecules (proteins such as enzymes, nucleic acid, etc.) in different types of surfaces and materials has been widely documented, because once they are immobilized on a substrate, they often show better physical stability and a greater capacity to be reused [11]. Therefore, the immobilized biomolecules have important advantages over the biomolecules in suspension, since it is not necessary to continuously restore the biocatalyst, which has economic benefits and it is relatively easy to recover the enzymatic components at the end of any reaction. In many cases, it is also possible to obtain higher catalyst concentrations in the reaction mixture; and additionally, the immobilized biomolecule could be physically more stable than the one in suspension [12, 13]. Various types of biomolecules have been successfully immobilized by simple physical

adsorption or adsorption on functionalized nanostructures such as polymers, biomolecules or surfactants by means of covalent bonds [14–16].

The immobilization of enzymes on different types of nanostructures is a research area that still presents great challenges for practical implementation [12, 17], where novel materials such as carbon nanostructures that present biocompatibility, high stability, surface area, and conductivity help enzymes to retain their catalytic properties [18]. For that reason, with the aim of developing a robust biocatalyst, an enzyme extract was immobilized on the surface of two different nanostructures, CNTs and CNSs. To analyze the materials as catalytic supports, different characterizations are made, using Raman and Fourier-transform infrared (FTIR) spectroscopies, scanning electron microscopy (SEM), energy-dispersive X-ray spectroscopy (EDS), electrochemical impedance spectroscopy (EIS) and cyclic voltammetry (CV) method. In agreement with the structural and electrochemical characterization, the CNSs present better qualities as enzyme immobilization support, due to their higher electrical conductivity, and lower crystallinity enhancing surface oxidation that results in more anchor points to the enzymatic support.

Materials and methods

Carbon nanostructures were synthesized by chemical vapor deposition (CVD) in the Nanostructured Materials Synthesis and Electrochemical Characterization Laboratory of the Center for Research and Advanced Studies of the National Polytechnical Institute (CINVESTAV) in Mexico. Raw enzyme extract, obtained using fungal inoculum generation, from fungal strains identified by phylogenetic analysis as *Trametes versicolor* (CMUTA01) was donated by Dr. Gerardo Vazquez Marrufo from the Michoacán University in Mexico. In agreement with the study made by Vazquez, CMUTA01 produces three ligninolytic enzymes: laccase, manganese peroxidase and lignin peroxidase [19]. Glutaraldehyde at 50% from Sigma-Aldrich was used as a surface modifier to immobilize the extracted enzymes onto the carbon nanostructures surface. As working electrodes, there were used cylindrical Graphite ST-21 bars of 3 mm of diameter supplied by Bay Carbon, Inc. The electrolyte was 0.1 M phosphate buffer solution (PBS) prepared with Na_2HPO_4 and KH_2PO_4 at pH value of

6.5. The EIS and CV characterization were carried out in a solution 5 mM of $K_3[Fe(CN)_6]/K_4[Fe(CN)_6]$ in 0.1 M KCl as electrolyte.

For the FTIR analysis, a Bruker IR Tensor 27 spectrophotometer was used with a wavenumber range of 400 to 4000 cm^{-1} , using 24 swept cycles and 4 cm^{-1} of resolution. Raman spectroscopy was performed using a Lab RAM HR Evolution Raman spectrometer from Horiba. For the Raman measurements, a He-Ne excitation laser of 632.8 nm was used, with 2 mW of power through 50X LD lens and 2 μm spot to avoid photodecomposition of the samples. Morphology and surface composition were characterized by JEOL Scanning Electron Microscope JSM-7600F. For the electrochemical measurements, EIS and CV were performed with a Potentiostat/Galvanostat/ZRA, Gamry Instruments, Inc. All experiments were carried out with a conventional three-electrode system in a glass electrochemical cell, working with a graphite electrode, coated with different composites. The counter electrode was a platinum wire. A saturated calomel electrode (SCE) was used as reference electrode. All experiments were performed at room temperature.

Catalyst support preparation

Carbon nanostructures were synthesized by the CVD process using an iron-cobalt (Fe-Co) powder alloy prepared by the sol-gel process and using silica as support. The ratio silica/catalyst was 50/50 (w/w). Acetylene was used as gas precursor. At a temperature of 700 °C and by controlling the decomposition of carbon over the metal catalyst; the carbon nanostructure-morphology can be modified [20, 21]. A flow rate of 1.0 sccm of the gas precursor produces CNTs, while 0.5 sccm of the precursor gas produces CNSs. The prepared CNTs had an average diameter of about 30 nm and the CNSs 100 nm.

Functionalization of CNTs and CNSs

It was necessary to functionalize the carbon nanostructures for attaching the enzymes. For that reason, an adaptation of the procedure described by Raghava et al. [20] was implemented. The CNTs and CNSs as prepared were dispersed on a mixture of concentrated acids of H_2SO_4/HNO_3 (3:1 v/v) and sonicated at room temperature continually for 2 h. After that, deionized water was added to the mixture of acids

and carbon nanostructures. The suspension was left to rest overnight, and the next day the samples were filtrated and rinsed with deionized water until neutral pH was obtained. Finally, the samples were dried during the night at 80 °C. Figure 1 shows a scheme of the whole process of functionalization.

Covalent immobilization of enzymatic extract onto CNTs and CNSs through glutaraldehyde

The enzymes of the extract were immobilized on the carbon nanostructures surfaces modifying the process of Abraham et al. [22] and Verma et al. [23], according to the next procedure: 5 mg/mL of acid-modified CNTs and CNSs were suspended in deionized water and sonicated for 30 min; then, a solution 1% (w/w) of glutaraldehyde (GA) was added. GA is generally a dependable material that invariably gives high yields of immobilized protein on the support. GA acts to cross-link the enzymes with the superficial functional groups on the carbon nanostructures. The mixture was sonicated again for 1 h, and the modified carbon nanostructures were removed by centrifugation and rinsed with deionized water. Later, the covalent binding of the enzymes to the carbon nanostructures was achieved by incubating the activated supports with extract, suspending the carbon nanostructures in the enzyme extract solution at 25 °C for 1 h using a shaker at 250 rpm. After that, all the enzymes that were not covalently

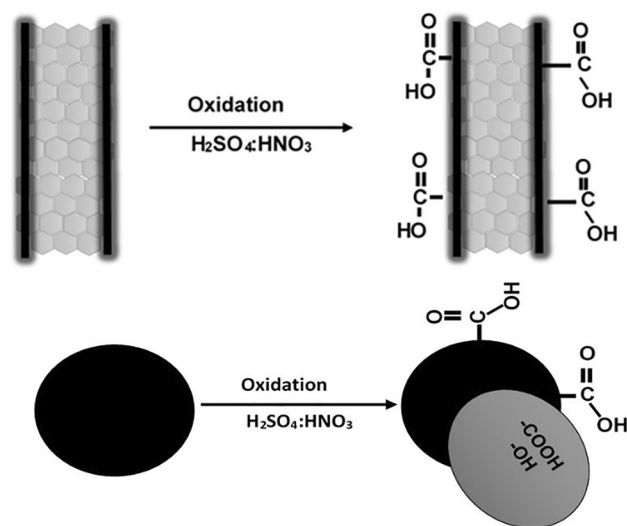


Figure 1 Graphic representation of the carbon nanostructures before and after being oxidized by acid treatment.

bonded to the carboxylic groups were removed by repeated washings with deionized water and the PBS. The immobilization method described is illustrated in Fig. 2.

Results and discussion

An analysis of the carbon nanostructures was performed using Raman spectroscopy to characterize the structural, electronic and vibrational properties of CNSs and CNTs. According to the literature, graphitic carbon materials can be characterized by three bands in the Raman spectrum. The first is the D-band, known as “disorder induced.” That band is attributed to the defects that the nanotube can contain in the network and to the presence of impurities. That band is located at $\sim 1330\text{ cm}^{-1}$ and corresponds to the mode of A_{1G} vibration. The second one is called G-band, due to in-plane vibrations of sp^2 carbons or

stretching mode of C–C bonds and is located at 1580 to 1600 cm^{-1} . That band corresponds to the fundamental vibration (first order) of tangential elongation and is assigned to the vibration mode E_{2G} . The third band is called G'-band and is located at $\sim 2660\text{ cm}^{-1}$. The G'-band corresponds to an overtone of the D mode and usually decrease inversely proportional with the number of graphene layers [24, 25]. Additionally, from the relative intensity between the D- and G-bands, the degree of graphitization of the nanotube walls is determined, as well as the presence of defects in the network thereof. The intensity ratio between the I_D/I_G bands is greater than one which indicates the presence of defects [26–28], where it is possible to attach the enzymes.

Figure 3 shows the comparative Raman spectra of the carbon nanostructures, in their pristine form, CNS-P and CNT-P, after the oxidation process, CNS-O and CNT-O and after the functionalization with the enzymes CNS-E and CNT-E. As it can be seen, for the

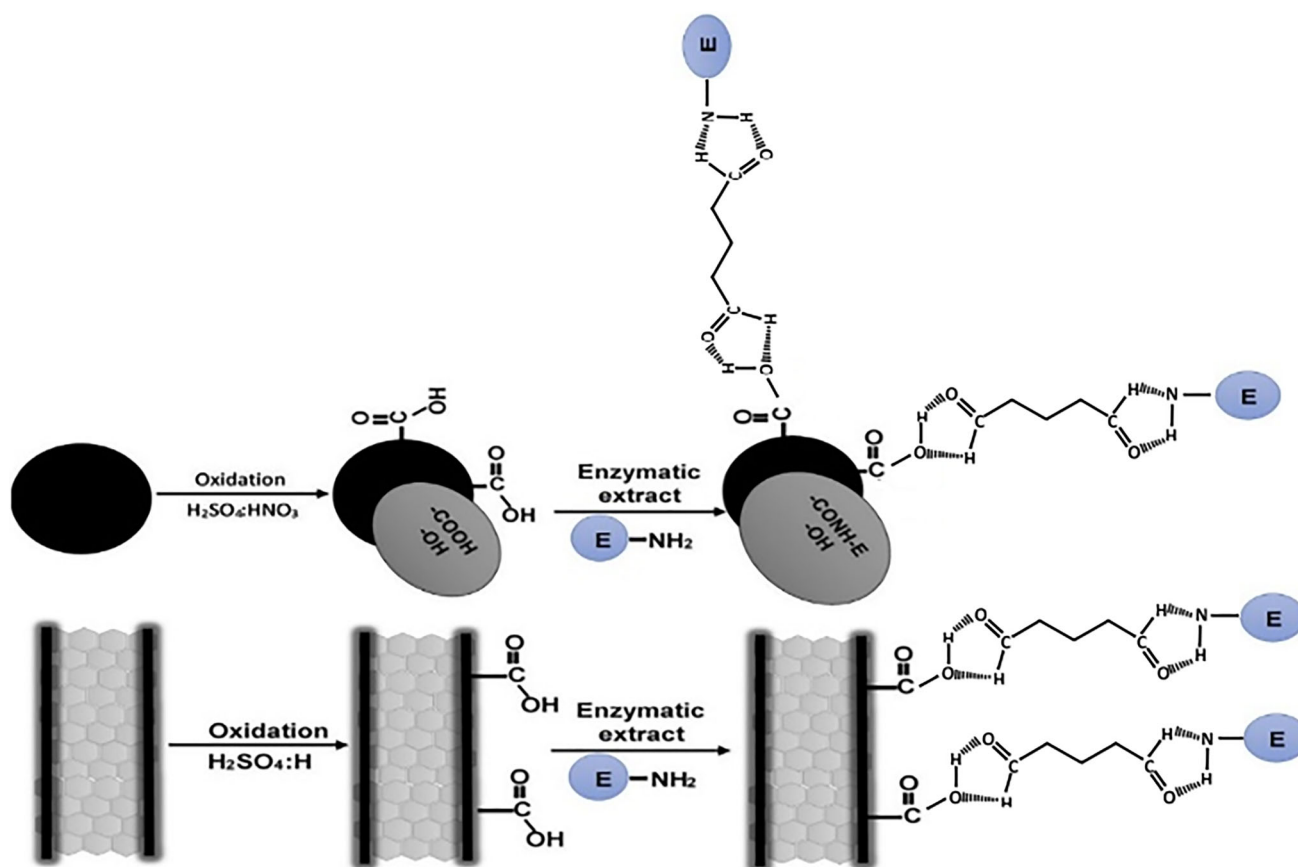


Figure 2 Schematic representation of the covalent immobilization of enzymes on carbon nanostructures. After the oxidation process, the functional groups are modified by the glutaraldehyde allowing

a covalent bond between carbon nanostructures and the enzymes. The circle with E represents enzymes.

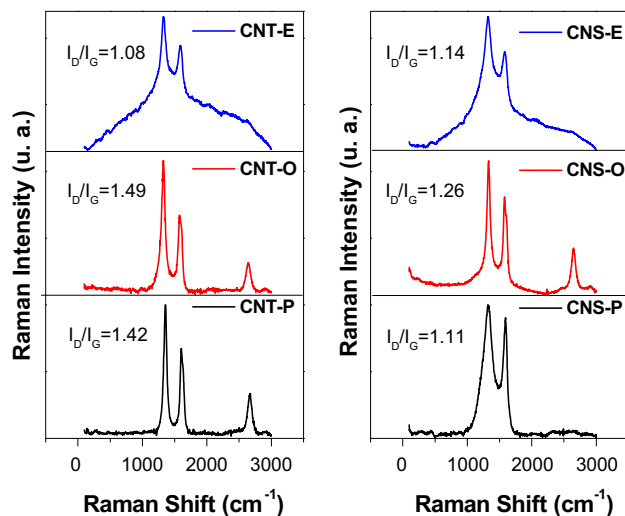


Figure 3 Raman spectra of CNTs and CNSs after normalization of curves. P, O and E refer to the pristine, oxidized and enzymes covered nanostructures, respectively.

two nanostructures there are important changes in the position, width and relative intensity of every band, which depend on the acid treatment or the attachment of glutaraldehyde and/or the enzymes. As shown in Fig. 3, in their pristine form CNSs present a broader D-band compared to CNTs which is eliminated by the oxidation process. That broadness is related to a greater superficial amorphism, and accordingly, CNTs are more crystalline than CNSs. Additionally, after the acid treatment, the number of defects was increased, as can be seen from the changes in the I_D/I_G ratio, which is good for increasing the number of superficial sites where the enzymes were attached. From the same figure, the acid treatment generates superficial groups on both nanostructures and reduces the number of walls, causing a rise of G'-band on CNTs and the presence of that band on CNSs. On the other hand, after functionalization, important variations appear in the D-band and G-band. Those bands are still present but a big luminescent spectral involves them; this is attributed to the presence of the enzyme extract over both carbon nanostructures, CNTs and CNSs.

The FTIR spectra of CNT-P, CNT-O, CNS-P and CNS-O are compared in Fig. 4. For CNT-P (4a), the spectra did not show any band in comparison with that of CNS-P (4c), which shows an intense band, centered around 3428 cm^{-1} . That band is associated with stretching modes of the OH groups attributed to the adsorbed water and carboxyl groups on the

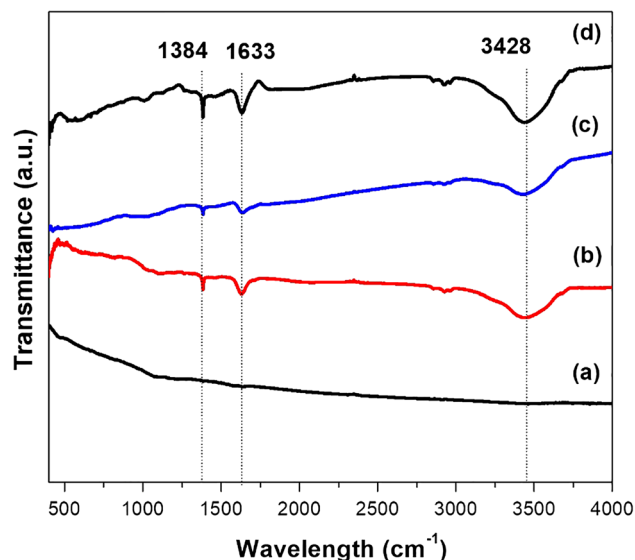


Figure 4 FTIR spectra of CNTs and CNSs before and after the oxidation process. **a** CNT-P, **b** CNT-O, **c** CNS-P and **d** CNS-O.

surface. That band appears from the beginning on the surface of the CNSs which gives an idea of the great number of defects of those structures when they are synthesized. For the CNTs, that band appears after the acid treatment. The band around 1633 cm^{-1} is due to the stretching of the carboxylic groups, $\text{C}=\text{O}$, in both functionalized structures, CNT-O (4b) and CNS-O (4d), which increased after the chemical treatment. That fact is consistent with that reported by Mao et al. [9], Schierz et al. [29] and Sun et al. [30]. On the other hand, the band at 1383 cm^{-1} is associated with the stretching vibrations of the $\text{C}-\text{O}$ group, which is part of the carboxyl group [31, 32]. The signals found for CNS-O are stronger when compared to that of the CNTs spectra, where it is possible to conclude that the surface of the CNSs is more susceptible to the formation of carboxylic groups.

SEM characterization was used to observe the morphology and to confirm the success of enzyme immobilization on the carbon nanostructure surfaces. A sample of CNTs and CNSs after the oxidation process and after the enzyme immobilization was dispersed in ethanol. A drop was deposited on a small piece of silicon wafer and coated with a thin layer of gold for improving the conductivity and to prevent degradation of the enzymes of the extract by means of the electron beam during the observation. Figure 5a shows the SEM image of the CNT-O; where no amorphous residues are present and the entangled nanotubes are clearly distinguished. On the

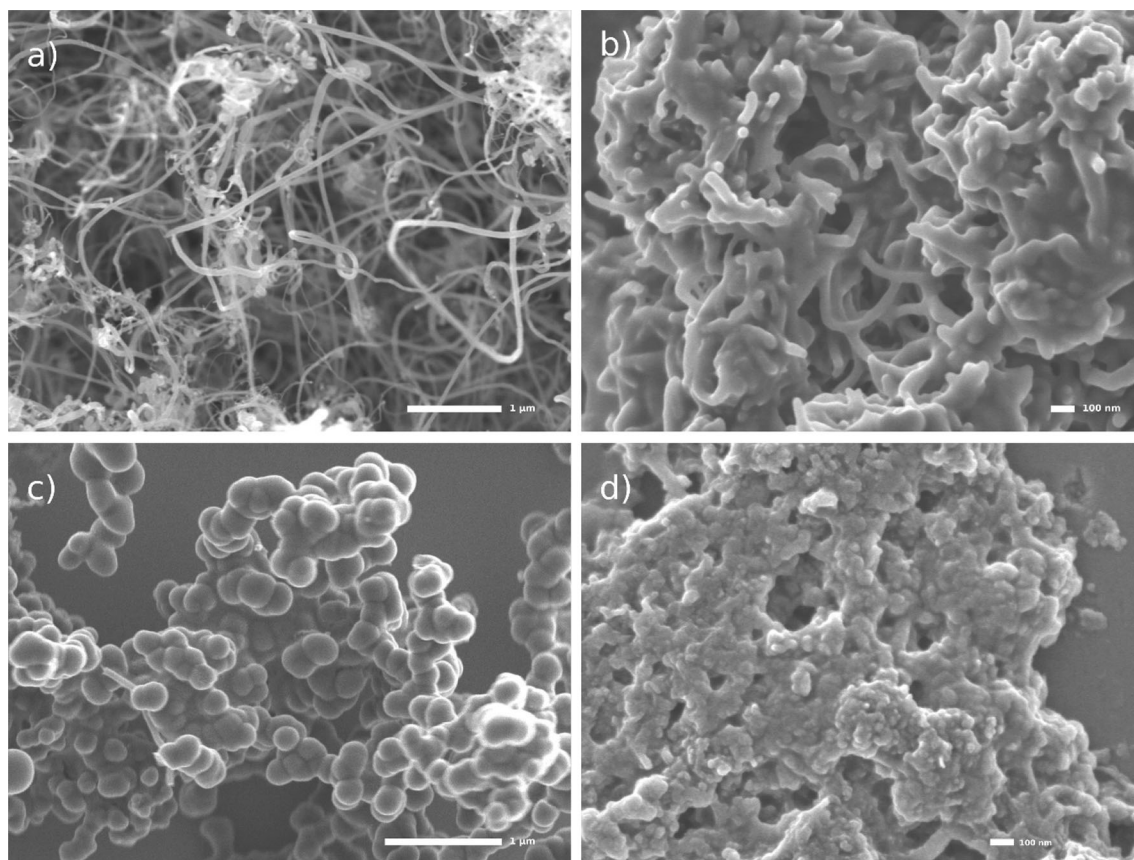


Figure 5 SEM analysis of: **a** CNT-O, **b** CNT-E, **c** CNS-O and **d** CNS-E.

other hand, Fig. 5b shows the image of the CNT-E when the glutaraldehyde and the enzymes are added; in that image, it is possible to see how the nanotubes are completely covered by glutaraldehyde and enzymes. The micrograph 5c shows clean spheres which present some superficial irregularities due to the oxidation process, CNS-O, while in Fig. 5d similarly for the CNTs is observed the presence of glutaraldehyde and enzymes on the surface of the carbon nanospheres, CNS-E.

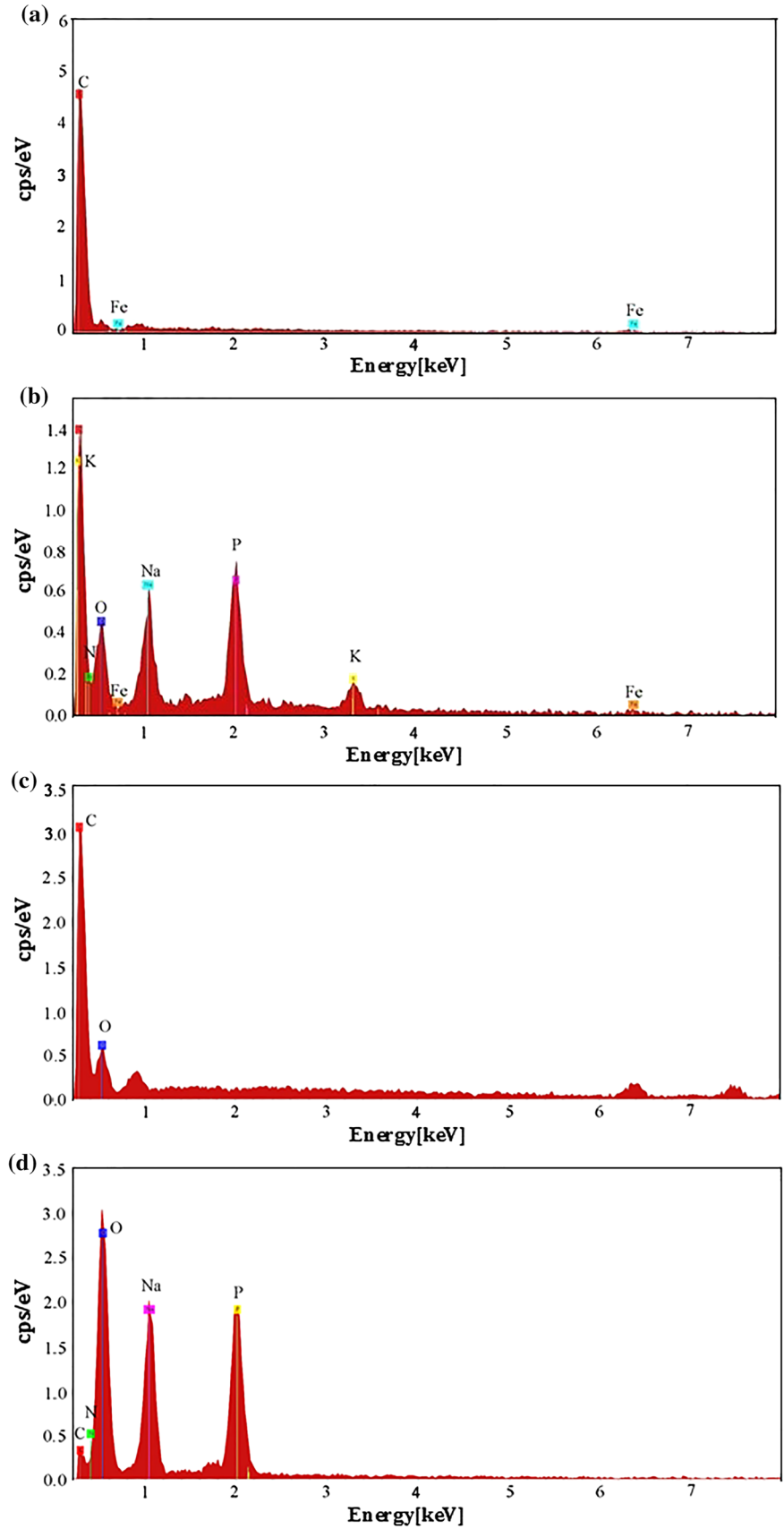
Figure 6 shows EDS analysis of CNTs and CNSs. In Fig. 6a, the EDS analysis reveals the characteristic carbon and oxygen signals, those belong to carbon structure and the oxidation products (carboxyl groups), CNT-O. The spectrum of Fig. 6b shows the characteristic signals of sodium and phosphorus which are related to the presence of the PBS on the surface. Additionally, the changes on the carbon and oxygen bands indicate the presence of the enzyme extract over the carbon nanostructures, CNT-E. Figure 6c shows the EDS analysis for the oxidized carbon nanospheres, CNS-O where the oxygen signal is

greater than that for CNT-O. That implies that more functional groups were generated on the surface of carbon nanospheres, consequently giving more anchor points and therefore a greater quantity of enzymes of the extract. That was confirmed by more intense signals than that for CNTs in the EDS analysis of Fig. 6d for sodium and phosphorus, CNS-E.

Enzymes are proteins that present highly selective catalytic properties toward specific substrates. Therefore, to analyze electrochemically the immobilization of the enzyme extract over the carbon nanostructures, the reaction redox $K_4Fe(CN)_6/K_3Fe(CN)_6$ was used as a mediator. The kinetic process of that reaction is fast and reversible and presents a well-characterized electrochemical behavior.

The EIS was used to evaluate the changes in the electrodes surfaces [33]. It is well known for EIS that a semi-circular curve at high frequencies in the Nyquist diagram is related to the electronic transfer, in other words, gives kinetic information of the redox process on the electrode surface. The Randles circuit (inserted in Fig. 6) is chosen to fit the obtained impedance data

Figure 6 EDS analysis of:
a CNT-O, **b** CNT-E, **c** CNS-O
 and **d** CNS-E.



containing the electron transfer process (modeled as a load transfer resistance, R_{ct}) and the diffusion process (modeling as the Warburg-type impedance, W). The diameter of the semi-circle corresponds to the interfacial electron transfer resistance (R_{ct}). On the other hand, the linear curve at low frequencies is associated with the diffusion process [34]. Electrochemical impedance spectroscopy (EIS) results for the materials of this research are presented in Fig. 7. The EIS characterization shows the curves for the graphite electrode covered by CNT-E, CNS-E and the electrode with a mixture of the enzymes extract and glutaraldehyde. The graphite electrode presents a linear tendency caused by one step systems with no resistance to the charge transfer process. After adding the composite CNT-E in the transducer surface, a short semi-circle appeared at high frequencies caused by the increase in resistance interface (48.15Ω). In the same way, when CNS-E were added to the electrode, EIS spectra show a resistance variation at high frequencies (27.40Ω), this is lower than that for CNT-E and could be attributed to the spherical symmetry. Besides, the composite extract/glutaraldehyde shows a semi-circle explained by the non-conductive properties of the enzymatic extract. This produced an increase in resistance to the transfer of 135Ω [6, 34–36].

Cyclic voltammetry (CV) is a versatile electroanalytical technique which monitors redox behavior of

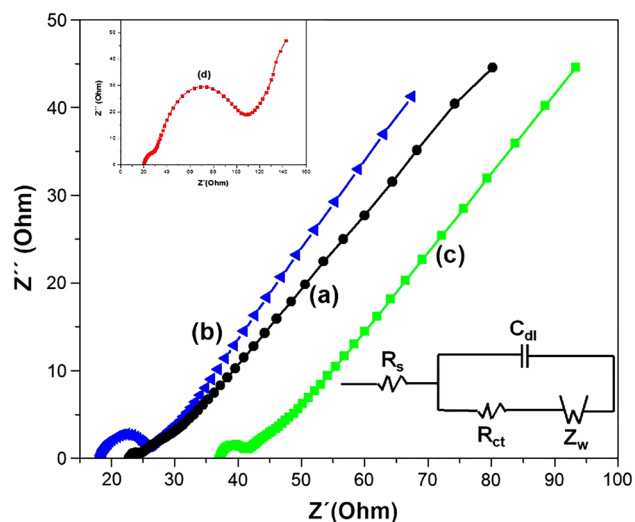


Figure 7 EIS of **a** graphite bar electrode, **b** CNS-E, **c** CNT-E, **d** Enzyme extract mixed with glutaraldehyde. A solution 0.1 M KCl and 5 mM of $K_3[Fe(CN)_6]/K_4[Fe(CN)_6]$ was used as electrolyte.

chemical species within a wide potential range. In the presence of an electroactive molecule a voltammogram shows a characteristic signal due to the reduction and/or oxidation of the electroactive molecule. Therefore, the redox reaction $K_4Fe(CN)_6/K_3Fe(CN)_6$ was used as mediator and KCl as supporting electrolyte, the scan rate was 100 mVs^{-1} and the potential ranged was -0.6 to 0.80 V .

Cyclic voltammograms obtained using 5 mM of $K_3[Fe(CN)_6]/K_4[Fe(CN)_6]$ and 0.1 M KCl as electrolyte and with a scan rate of 100 mVs^{-1} . (a) Graphite bar electrode, (b) CNS-E, (c) CNT-E (d) Mixture of enzymes extract with glutaraldehyde.

Cyclic voltammeteries for the different prepared materials are shown in Fig. 8: over (a) the graphite electrode, (b) the electrode with CNTs and extract, CNT-E, electrode with CNSs and extract (c) CNS-E and (d) a mixture of glutaraldehyde and the enzymes extract. In the curves, it is appreciated only the well-defined characteristic signals of the redox pair of $K_4Fe(CN)_6/K_3Fe(CN)_6$ and its classic reversible behavior. Curve 8a shows the electrochemical response over only the graphite electrode showing similarities with those reported by Perenlei et al. [37]. After adding the extract, the current density increases due to the high electrical conductivity of carbon supports, but in CNS-E is higher than that of CNT-E. That fact is attributed to the excess of carboxylic groups present on the surface of that carbon nanostructure which helped to increase the quantity of

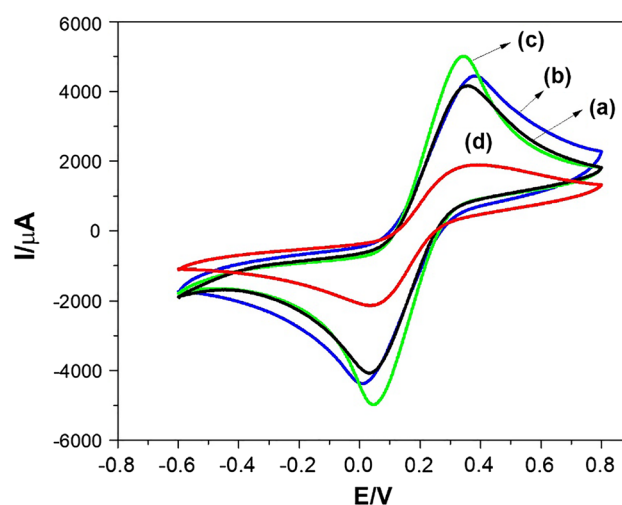


Figure 8 Cyclic voltammograms obtained using 5 mM of $K_3[Fe(CN)_6]/K_4[Fe(CN)_6]$ and 0.1 M KCl as electrolyte at a scan rate of 100 mVs^{-1} . **a** Graphite bar electrode, **b** CNT-E, **c** CNS-E, **d** mixture of enzymes extract with glutaraldehyde.

immobilized enzymes over the surface. The mixture of glutaraldehyde and the enzymes extract over the graphite electrode obtained the lowest current density due to the poor electrical conductivity which will inhibit the catalytic response of this material.

Conclusions

The results demonstrate the use of two different carbon nanostructures, CNTs and CNSs, as support to immobilize the enzyme extract, for example, for efficient development of biocatalysts. The enzymatic electrode obtained showed high electroanalytical efficiency for practical purposes. The correct immobilization was due to the presence of carboxyl groups occurred in the oxidation process, which was corroborated by Raman, FTIR, SEM and EDS. On the other hand, the results obtained by the electrochemical characterization with the enzymes provided the adequate immobilization of enzymes on CNSs and CNTs for its potential applications as biocatalysts for a delignification process, nano-biosensor or any other application. Even more, in the comparison of both carbon nanostructures, CNSs present better qualities as support, due to their higher electrical conductivity, lower crystallinity that helps to enhance surface oxidation and more anchor points to the enzymatic support. Furthermore, CNSs present the highest current densities in the redox $K_4Fe(CN)_6/K_3Fe(CN)_6$ system in comparison with those obtained for the other electrodes. In summary, CNSs improve the transfer of electrons in the redox process, accelerating the transfer of electrons between the electroactive sites embedded in the enzymes and the electrode. The results are excellent, considering that the process for obtaining CNSs is easy to scale up and the obtained quantity of CNSs is greater when compared with the production of CNTs.

Acknowledgements

Authors show their gratitude to the Michoacan University which provided the biological and electrochemical characterization, especially to Dr. Gerardo Vazquez Marrufo who gave the enzyme extract. We acknowledge the carbon nanomaterials and their structural characterization to CINVESTAV. Mariana Romero Arcos wants to thank the fund CONACYT-

SENER for the scholarship support. The M. A. Gonzalez-Reyna and Maria Selene Luna-Martínez's scholarships were supported by CONACYT under grant 424698.

Compliance with ethical standards

Conflict of interests We declare that there is no conflict of interests among the authors or with our institution. In fact, our institution is so interested in publishing the results of our different researches.

References

- [1] Park JH, Xue H, Jung JS, Ryu K (2012) Immobilization of laccase on carbon nanomaterials. *Korean J Chem Eng* 29:1409–1412. <https://doi.org/10.1007/s11814-012-0024-1>
- [2] Endo M, Hayashi T, Kim Y-A (2006) Large-scale production of carbon nanotubes and their applications. *Pure Appl Chem* 78:1703–1713. <https://doi.org/10.1351/pac200678091703>
- [3] Vargas-García JR, Calderón-Domínguez G, Ortiz-López J, Manzo-Robledo A, Guadarrama-Fernández L, Chanona-Pérez J, Martínez-Rivas A (2014) Characterization of functionalized multiwalled carbon nanotubes for use in an enzymatic sensor. *Microsc Microanal* 20:1479–1485. <https://doi.org/10.1017/s143192761401304x>
- [4] Liu M, Zhang F, Li J, Feng Y, Kuang D (2010) Voltammetric determination of bisphenol A in food package by a glassy carbon electrode modified with carboxylated multi-walled carbon nanotubes. *Microchim Acta* 172:379–386. <https://doi.org/10.1007/s00604-010-0512-0>
- [5] Silva CG, Tavares APM, Dražić G, Silva AMT, Loureiro JM, Faria JL (2014) Controlling the surface chemistry of multi-walled carbon nanotubes for the production of highly efficient and stable laccase-based biocatalysts. *Chempluschem* 79:1116–1122. <https://doi.org/10.1002/cplu.201402054>
- [6] Oliveira TMBF, Fátima Barroso M, Morais S, De Lima-Neto P, Correia AN, Oliveira MBPP, Delerue-Matos C (2013) Biosensor based on multi-walled carbon nanotubes paste electrode modified with laccase for pirimicarb pesticide quantification. *Talanta*. 106:137–143. <https://doi.org/10.1016/j.talanta.2012.12.017>
- [7] Kaushik A, Tiwari A, Malhotra BD, Ansari AA, Solanki PR (2009) Multi-walled carbon nanotubes/sol-gel-derived silica/chitosan nanobiocomposite for total cholesterol sensor. *Sens Actuators B Chem* 137:727–735. <https://doi.org/10.1016/j.snb.2008.12.044>
- [8] Banks CE, Compton RG (2004) *i - S E C T I O N E D U C A T I O N* Ultrasound: promoting electroanalysis in difficult real world media. *Analyst* 129:678–683

- [9] Mao H, Chen X, Huang R, Chen M, Yang R, Lan P, Zhou M, Zhang F, Yang Y, Zhou X (2018) Fast preparation of carbon spheres from enzymatic hydrolysis lignin: effects of hydrothermal carbonization conditions. *Sci Rep* 8:2–11. <https://doi.org/10.1038/s41598-018-27777-4>
- [10] Chen C, Yu D, Zhao G, Du B, Tang W, Sun L, Sun Y, Besenbacher F, Yu M (2016) Three-dimensional scaffolding framework of porous carbon nanosheets derived from plant wastes for high-performance supercapacitors. *Nano Energy* 27:377–389. <https://doi.org/10.1016/j.nanoen.2016.07.020>
- [11] Mahmoud D (2007) Immobilization of invertase by a new economical method using wood sawdust waste. *Aust J Appl Sci* 1:364–372
- [12] Cang-Rong JT, Pastorin G (2009) The influence of carbon nanotubes on enzyme activity and structure: investigation of different immobilization procedures through enzyme kinetics and circular dichroism studies. *Nanotechnology*. <https://doi.org/10.1088/0957-4484/20/25/255102>
- [13] Liang JF, Li YT, Yang VC (2000) Biomedical application of immobilized enzymes. *J Pharm Sci* 89:979–990. [https://doi.org/10.1002/1520-6017\(200008\)89:8%3c979:AID-JPS2%3e3.0.CO;2-H](https://doi.org/10.1002/1520-6017(200008)89:8%3c979:AID-JPS2%3e3.0.CO;2-H)
- [14] Karim F, Fakhrudin ANM (2012) Recent advances in the development of biosensor for phenol: a review. *Rev Environ Sci Biotechnol* 11:261–274. <https://doi.org/10.1007/s11157-012-9268-9>
- [15] Kausaite-Minkstimiene A, Mazeiko V, Ramanaviciene A, Ramanavicius A (2011) Evaluation of amperometric glucose biosensors based on glucose oxidase encapsulated within enzymatically synthesized polyaniline and polypyrrole. *Sens Actuators B Chem* 158:278–285. <https://doi.org/10.1016/j.snb.2011.06.019>
- [16] Feng L, Zhao Y, Luo X, Tu X, Li J, Luo S (2011) Metal chelate affinity to immobilize horseradish peroxidase on functionalized agarose/CNTs composites for the detection of catechol. *Sci China Chem* 54:1319–1326. <https://doi.org/10.1007/s11426-011-4298-7>
- [17] Andreescu S, Njagi J, Ispas C (2008) Chapter 7 - Nanos-structured materials for enzyme immobilization and biosensors, in: V. Erokhin, M.K. Ram, O.B.T.-T.N.F. of O. and C.N. Yavuz (Eds.), Elsevier, Amsterdam, pp 355–394. doi:<https://doi.org/10.1016/B978-008045052-0.50009-9>
- [18] Saifuddin N, Raziah AZ, Junizah AR (2013) Carbon nanotubes: a review on structure and their interaction with proteins. *J Chem*. <https://doi.org/10.1155/2013/676815>
- [19] Mari R (2017) Characterization of ligninolytic enzyme production in white-rot wild fungal strains suitable for kraft pulp bleaching. <https://doi.org/10.1007/s13205-017-0968-2>
- [20] Pradhan D, Sharon M (2002) Carbon nanotubes, nanofilaments and nanobeads by thermal chemical vapor deposition process. *Mater Sci Eng B Solid-State Mater Adv Technol* 96:24–28. [https://doi.org/10.1016/s0921-5107\(02\)00309-4](https://doi.org/10.1016/s0921-5107(02)00309-4)
- [21] Coville NJ, Mhlanga SD, Nxumalo EN, Shaikjee A (2011) A review of shaped carbon nanomaterials. *S Afr J Sci* 107:1–15. <https://doi.org/10.4102/sajs.v107i3/4.418>
- [22] Abraham RE, Verma ML, Barrow CJ, Puri M (2014) Suitability of magnetic nanoparticle immobilised cellulases in enhancing enzymatic saccharification of pretreated hemp biomass. *Biotechnol Biofuels* 7:1–12. <https://doi.org/10.1186/1754-6834-7-90>
- [23] Verma ML, Chaudhary R, Tsuzuki T, Barrow CJ, Puri M (2013) Immobilization of β -glucosidase on a magnetic nanoparticle improves thermostability: application in cellobiose hydrolysis. *Bioresour Technol* 135:2–6. <https://doi.org/10.1016/j.biortech.2013.01.047>
- [24] Pacley S, Theodore M (2011) Characterization of catalyst effect on carbon nanopearls. *NSTI-Nanotech* 1:307–310
- [25] Domingo C, Santoro G (2007) Espectroscopía Raman de nanotubos de carbono Raman spectroscopy of carbon nanotubes ABSTRACT: *Opt Pura Apl* 1136:175–186
- [26] Malard LM, Pimenta MA, Dresselhaus G, Dresselhaus MS (2009) Raman spectroscopy in graphene. *Phys Rep* 473:51–87. <https://doi.org/10.1016/j.physrep.2009.02.003>
- [27] Messina G, Donato MG, Santangelo S, Pistone A, Milone C, Galvagno S (2006) Optimisation of gas mixture composition for the preparation of high quality MWCNT by catalytically assisted CVD. *Diam Relat Mater* 16:1095–1100. <https://doi.org/10.1016/j.diamond.2006.12.018>
- [28] Donato MG, Messina G, Milone C, Pistone A, Santangelo S (2008) Experiments on C nanotubes synthesis by Fe-assisted ethane decomposition. *Diam Relat Mater* 17:318–324. <https://doi.org/10.1016/j.diamond.2007.12.043>
- [29] Schierz A, Zänker H (2009) Aqueous suspensions of carbon nanotubes: surface oxidation, colloidal stability and uranium sorption. *Environ Pollut* 157:1088–1094. <https://doi.org/10.1016/j.envpol.2008.09.045>
- [30] Sun X, Li Y (2004) Colloidal Carbon Spheres and Their Core/Shell Structures with Noble-Metal Nanoparticles. *Angew Chemie Int Ed* 43:597–601. <https://doi.org/10.1002/anie.200352386>
- [31] Ahmed DS, Haider AJ, Mohammad MR (2013) Comparison of functionalization of multi-walled carbon nanotubes treated by oil olive and nitric acid and their characterization. *Energy Proc* 36:1111–1118. <https://doi.org/10.1016/j.egypro.2013.07.126>
- [32] Chen J, Xia N, Zhou T, Tan S, Jiang F, Yuan D (2009) Mesoporous carbon spheres: synthesis, characterization and supercapacitance. *Int J Electrochem Sci* 4:1063–1073
- [33] Chauhan N, Pundir CS (2011) An amperometric biosensor based on acetylcholinesterase immobilized onto iron oxide

- nanoparticles/multi-walled carbon nanotubes modified gold electrode for measurement of organophosphorus insecticides. *Anal Chim Acta* 701:66–74. <https://doi.org/10.1016/j.aca.2011.06.014>
- [34] Chawla S, Rawal R, Kumar D, Pundir CS (2012) Amperometric determination of total phenolic content in wine by laccase immobilized onto silver nanoparticles/zinc oxide nanoparticles modified gold electrode. *Anal Biochem* 430:16–23. <https://doi.org/10.1016/j.ab.2012.07.025>
- [35] Mayorga-Martinez CC, Cadevall M, Guix M, Ros J, Merkoçi A (2013) Bismuth nanoparticles for phenolic compounds biosensing application. *Biosens Bioelectron* 40:57–62. <https://doi.org/10.1016/j.bios.2012.06.010>
- [36] C Jiang, H Chen, C Yu, S Zhang, B Liu, J Kong (2009) *Electrochimica Acta* Preparation of the Pt nanoparticles decorated poly (N -acetylaniline)/MWNTs nanocomposite and its electrocatalytic oxidation toward formaldehyde, 54: 1134–1140. Doi: 10.1016/j.electacta.2008.08.071
- [37] Perenlei G, Tee TW, Yusof NA, Kheng GJ (2011) Voltammetric detection of potassium ferricyanide mediated by multi-walled carbon nanotube/titanium dioxide composite modified glassy carbon electrode. *Int J Electrochem Sci* 6:520–531

Publisher's Note Springer Nature remains neutral with regard to jurisdictional claims in published maps and institutional affiliations.